THE UNIVERSITY *of* EDINBURGH

Modulation, Tracking and Adaptive System Design for Robust Optical Wireless Communications

Jianhui Chen

A thesis submitted for the degree of Doctor of Philosophy.
The University of Edinburgh.
July 31, 2025

Dedication

This thesis is dedicated to the memory of Yufeng Lai and Qingming Lei.

Abstract

Optical wireless communication (OWC) has emerged as a promising technology for high-speed wireless connectivity, offering vast unregulated bandwidth in the optical spectrum and inherent security advantages. However, the hostile nature of optical wireless channels, particularly in turbid, turbulent underwater and foggy free-space optical (FSO) environments, presents significant challenges for reliable data transmission. This thesis investigates the development of multiple complementary approaches to achieve link robustness in OWC systems, addressing challenges ranging from turbulence-induced fading and beam misalignment to time varying channel conditions through comprehensive theoretical analysis and experimental validation.

Through experimental evaluation in a controlled channel emulator, an empirical investigation of frequency-based modulation schemes combined with polarisation division multiplexing (PDM) in underwater optical wireless communication (UOWC) channels is presented. The results demonstrate that frequency-shift keying with subcarrier intensity modulation (FSK-SIM) and frequency-shift chirp modulation (FSCM) provide inherent resilience to turbulence-induced received optical intensity fluctuations. In addition, the incorporation of PDM successfully approximately doubles the system throughput while maintaining the robustness of two frequency-based techniques.

Building upon the need for link reliability, a fine tracking system for maintaining optical alignment in dynamic OWC links is developed. The system applies a photodiode array architecture with algorithm by differential intensity measurements to detect beam displacement in real-time. Experimental validation in free-space optical (FSO) channels demonstrates successful link maintenance at misalignment speeds up to 17.4 mm/s with 1.1% outage probability. Real-time image transmission experiments further validate the system's practical impact, reducing bit error rate (BER) from 0.305 without tracking to 2.29×10^{-3} with tracking enabled.

To simultaneously maximise data throughput and maintain link robustness under varying channel conditions, the investigation is expanded through the development of camera-based adaptive transmission strategies for both underwater and atmospheric channels. A k-nearest neighbour machine learning algorithm successfully classifies turbulence levels from captured images of backscattered light patterns with 99% accuracy, distinguishing between temperature-induced and bubble-induced turbulence. The system maintains reliable communication by dynamically adjusting modulation schemes based on the channel estimation, and achieves an average 3.51 Gbps throughout varying channel conditions.

The adaptive OWC is further developed and demonstrated through a channel state information (CSI) estimation architecture based on corner-cube retroreflector. The system exploits deterministic polarisation changes induced by retroreflectors to enable transmitter side channel monitoring. The bidirectional propagation path effectively doubles the channel's impact on the retroreflected signal, enhancing sensing sensitivity. Experimental validation demonstrates 9% throughput improvement in turbulent underwater channels and 15% improvement in foggy FSO channels compared to the best performing fixed modulation schemes.

Lay Summary

Optical wireless communication (OWC) uses beams of light instead of radio waves to transmit data wirelessly at high speeds. Similar to how a TV remote uses infrared light, OWC systems can send information through the air or underwater. This technology offers significant advantages over traditional methods, particularly underwater where it can achieve much faster data transmission than sound-based communication systems.

Despite these advantages, sending data through light beams faces significant challenges. When light travels through water or air, fog, bubbles, or temperature changes can disrupt the signal, much like how fog reduces visibility for the human eye. Another critical issue is maintaining alignment between the transmitter and receiver, as even small movements can cause the connection to fail.

This thesis addresses these challenges through four main contributions. First, it investigates advanced methods to encode information onto light beams, making them more resistant to disruptions. Second, it develops a tracking system that automatically maintains alignment between the transmitter and receiver during movement. Third, it presents a camera-based system that monitors channel conditions and automatically adjusts communication settings to maintain optimal performance. Fourth, it introduces an alternative approach using retroreflector that monitors channel conditions.

Laboratory experiments validate the effectiveness of these solutions. The frequency-based encoding methods combined with polarisation techniques successfully doubled data transmission capacity while maintaining robustness against turbulence. The tracking system successfully maintained stable connections under dynamic conditions. The camera-based system achieved high data rates by adapting to varying channel conditions, and the retroreflector approach provided efficient channel monitoring. These approaches provide practical methods to enhance the reliability of optical wireless communication in challenging real-world environments.

Declaration of Originality

I declare that this thesis was composed by myself, that the work contained herein is my own except where explicitly stated otherwise in the text, and that this work has not been submitted for any other degree or professional qualification except as specified.

Jianhui Chen
Edinburgh, Scotland, The United Kingdom
July 31, 2025

Acknowledgements

This research work is self-funded, with the necessary financial support provided from my family; this experience would not be possible without my parents' love unconditionally.

I would like to express my deepest gratitude to my supervisor, Professor Wasiu O. Popoola, for his invaluable guidance, unwavering support, and continuous encouragement throughout this research journey. His knowledge in optical wireless communication and insightful feedback have been instrumental in shaping this work. His patience in explaining the academic thoughts and willingness to engage in every project I worked on have significantly enriched my research experience.

Special thanks go to my colleagues and friends in or out of the academia. The countless hours of discussion and sharing everyday moments, ideas, troubleshooting experimental setups, and sharing both successes and setbacks have made this journey memorable. Particular acknowledgement goes to those who assisted with the underwater turbulence experiments and the development of tracking system hardware.

To my girlfriend, Manal, for your continuous supportive words and encouragement in those very late nights, it would have been more difficult to get to where I am without you. Thanks for being with me through those hard moments.

Contents

List of figures

List of tables

Acronyms and abbreviations

ADC analogue-to-digital converter

APD avalanche photodiode

AUV autonomous underwater vehicle

AWG arbitrary waveform generator

AWGN additive white Gaussian noise

BER bit error rate

BPSK binary Phase Shift Keying

BS beam splitter

CNN convolutional neural network

CSI channel state information

DoP degree of polarisation

DCO-OFDM DC-biased optical orthogonal frequency division multiplexing

PAPR peak-to-average power ratio

DC direct current

FEC forward error correction

FPS frame per second

FSK-SIM frequency-shift keying with subcarrier intensity modulation

FSO free-space optical

k-NN k-nearest neighbour

FSCM frequency-shift chirp modulation

FSK frequency-shift keying

ICI inter-channel interference

MIMO multiple-input multiple-output

IM/DD intensity modulation and direct detection

ISI inter-symbol interference

LD laser diode

LED light emitting diode

Msym/s mega symbols per second

OFDM orthogonal frequency division multiplexing

OOK on-off keying

OWC optical wireless communications

PAFsk phase, amplitude and frequency-shift keying

PAM pulse amplitude modulation

PBC polarising beam combiner

PBS polarising beam splitter

PD photodetector

PDF probability density function

PDM polarisation division multiplexing

PIN p-type intrinsic n-type diode

PMT photon multiplier tube

PPM pulse position modulation

PSD power spectral density

PSK phase-shift keying

QAM quadrature amplitude modulation

QKD quantum key distribution

RF radio frequency

Rx receiver

SI scintillation index

SIM subcarrier intensity modulation

SNR signal-to-noise-ratio

SPAD single photon avalanche diode

UCE underwater channel emulator

UOWC underwater optical wireless communications

VLC visible light communication

WDM wavelength division multiplexing

PAFsk-SIM phase-amplitude-frequency shift keying with subcarrier intensity modulation

IoT Internet of Things

IM intensity modulation

DD direct detection

VCSEL vertical-cavity surface-emitting laser

ML machine learning

DL deep learning

GK-DNN Gaussian kernel-based deep neural network

LSTM long short term memory

AMC adaptive modulation and coding

RIS reconfigurable intelligent surfaces

DCO DC-biased optical

ACO asymmetrically clipped optical

ASK amplitude-shift keying

CSS chirp spread spectrum

LoRa Long Range

DRL deep reinforcement learning

TDOA time difference of arrival

MEMS microelectromechanical systems

JMLD joint maximum likelihood detection

CAPD cluster algorithm of perception decisions

Nomenclatures

$\otimes$	Convolution operator
$\langle . \rangle$	Ensemble average operator
$\lfloor . \rfloor$	Floor operator
$\mathrm{mod}(\cdot, \cdot)$	Modulo operator
$\lvert . \rvert$	Absolute value
$Q(.)$	Q-function
α	APD electron ionization coefficient
α_n	Slot position index for n-th PPM symbol; $\alpha_n \in \{0, 1, \ldots, M-1\}$
α_{atten}	Channel attenuation coefficient
β	Modulation index
β_{APD}	APD hole ionization coefficient
$\Delta x, \Delta y$	Beam displacement
ΔT	Temperature variation
η	Quantum efficiency
η_t, η_r	Transmitter and receiver optical efficiencies
θ	Angle
λ	Wavelength
μ	Chirp rate in FSCM; $\mu = B/T_s$
ν	Optical frequency
σ_I^2	Scintillation index
σ_{MA}^2	Misalignment variance
τ	Time constant
ϕ	Phase
ϕ_i	Phase of i-th subcarrier
ϕ_x, ϕ_y	Phase components for orthogonal polarisations
ω	Angular frequency
ω_0	Beam waist radius
ω_i	Angular frequency of i-th subcarrier
$\mathscr{R}$	Photodetector responsivity

$a(\lambda)$	Absorption coefficient
$a_w(\lambda)$	Water absorption coefficient
$a_p(\lambda)$	Particle absorption coefficient
$a_{\text{CDOM}}(\lambda)$	CDOM absorption coefficient
a, b, c	Generalized Gamma Distribution fitting parameters
A	Junction area
A_c	Carrier amplitude
A_m	Amplitude level for M-PAM modulation
A_i	Amplitude of i-th subcarrier
A_{thresh}	Blue pixel threshold in camera detection
$A_{\text{FSM}}, E_{\text{FSM}}$	FSM azimuth and elevation angles
$b(\lambda)$	Scattering coefficient
$b_w(\lambda)$	Water scattering coefficient
$b_p(\lambda)$	Particle scattering coefficient
B	Bandwidth
c	Speed of light in vacuum
$c(\lambda)$	Total attenuation coefficient
C_n^2	Atmospheric structure parameter
D	Distance from centre to tracking PDs
D_r	Receiver aperture diameter
D_t	Transmitter aperture diameter
E_b	Energy per bit
E_s	Symbol energy
E_g	Bandgap energy
E_x, E_y	Electric field components
E'_x, E'_y	Transformed electric field components after retroreflection
$\|E_x\|, \|E_y\|$	Electric field magnitudes
$\vec{E}$	Electric field vector
f	Frequency
f_c	Carrier frequency
f_m	Frequency of m-th symbol in FSK
$f_m(t)$	Chirp frequency function for symbol m
$f_0(t)$	Basic chirp frequency; $f_0(t) = \mu t$

$f_{-3\text{dB}}$	-3dB bandwidth
$F(G_{\text{APD}})$	APD excess noise factor
G_{APD}	APD multiplication gain factor
G_x, G_y	Horizontal and vertical gradient components
$G_x(x,y), G_y(x,y)$	Gradient components in edge detection
$G(x,y)$	Gradient magnitude in edge detection
$G_\sigma(x,y)$	Gaussian filter function
$\text{Gain}(f)$	Adaptive transmit power gain as function of channel fuzziness
h	Planck's constant
$h(t)$	Channel impulse response
I	Received irradiance
$I(x,y)$	Intensity distribution
I_0	Maximum optical intensity
I_n, Q_n	In-phase and quadrature components for QAM
I_{bias}	DC bias current
I_{MA}	Misaligned intensity
$I_{\text{smooth}}(x,y)$	Smoothed image intensity
I_x, I_y	Gamma-gamma random variables
i	Subcarrier index
J_{ij}	Jones matrix element, $i,j \in \{1,2\}$
k	Boltzmann's constant
k_b	Number of bits per symbol; $k_b = \log_2 M$
k_{APD}	APD material parameter for gain calculation
k_{eff}	APD ionization coefficient ratio; $k_{\text{eff}} = \beta_{\text{APD}}/\alpha$
L	Link distance
m	Symbol index in FSCM
$m(t)$	Normalised modulating signal
M	Modulation order
M_a	Amplitude modulation order
M_f	Frequency modulation order
M_p	Phase modulation order
M_{pa}	Combined phase-amplitude (QAM) modulation order
M_{QAM}	QAM modulation order

n	Refractive index
$n(t)$	Noise signal
N	Number of subcarriers or frames (context-dependent)
N_{frames}	Number of frames in camera processing
N_0	Noise power spectral density
$p(t)$	Pulse shaping function
P_{ave}	Average transmitted optical power
P_{MAnorm}	Normalised power under misalignment
P_r	Received optical power
$P_t(t)$	Transmitted optical power
$P_t^x(t), P_t^y(t)$	Polarisation state powers
P_e	Error probability
$P_{e\sqrt{M}}$	Symbol error probability for square M-QAM constellation
P_{det}	Detection probability
P_{aligned}	Probability of beam alignment
P_{tracking}	Probability of tracking activation
P_{failure}	Probability of tracking failure
q	Elementary charge
q_{vis}	Size distribution parameter depending on visibility conditions
r	Receiver radius
r_{disp}	Radial displacement
r_{data}	Data PD lens radius
r_{PD}	Tracking PD radius
$r_{\text{threshold}}$	Threshold displacement radius
r_{detect}	Maximum detection range
R_b	Bit rate
R_L	Load resistance
R_s	Symbol rate
R_{beam}	Beam waist radius at receiver
R^2	Coefficient of determination
$s(t)$	Modulated signal (generic)
S_x, S_y	Sobel operators for edge detection
S_{filter}	Gaussian filter kernel size

SNR	Signal-to-noise ratio
SNR_{rx}	Received signal-to-noise ratio
BER	Bit error rate
SER	Symbol error rate
SI	Scintillation index (alternative to σ_I^2)
T	Temperature
T_b	Bit duration
T_{opt}	Optical transmission coefficient
T_s	Symbol duration
T_{sample}	Sampling period
$T_{\text{high}}, T_{\text{low}}$	Upper and lower thresholds for edge detection
TH	Tracking threshold
DLR, TD	Differential tracking signals (Left-Right, Top-Down)
ECF	Estimated Channel Fuzziness
WT	Warning threshold
v_s	Carrier saturation velocity
V	Visibility in kilometres
V_B	Breakdown voltage
V_R	Reverse bias voltage
V_{pp}	Peak-to-peak voltage
V_{pp}^x, V_{pp}^y	Peak-to-peak voltages for polarisation states
$V_{pp}^{\text{Tx,meas}}$	Measured peak-to-peak voltage at transmitter
$V_{pp}^{\text{Rx,est}}$	Estimated peak-to-peak voltage at receiver
w	Depletion region width
w_{EL}	Weight parameter in Exponential Lognormal distribution
x, y	Spatial coordinates
x_0, y_0	Initial beam position
$x_{\text{Lim}}, y_{\text{Lim}}$	Integration limits
$x_m(t)$	Time domain FSCM waveform for symbol m
$\hat{x}, \hat{y}$	Orthogonal polarisation unit vectors
$y(t)$	Received signal
z	Propagation distance variable

Chapter 1
Introduction

1.1 Motivation and Scope

Optical wireless communications (OWC) has emerged as a transformative technology that addresses the rapidly increasing demands for high speed wireless connectivity across diverse application domains. The exponential growth in data traffic, driven by bandwidth-intensive applications including high definition video streaming, virtual reality, and Internet of Things (IoT) deployments, has created a heavy strain on existing radio frequency (RF) spectrum resources. This spectrum scarcity crisis, coupled with the inherent limitations of RF systems including electromagnetic interference susceptibility and regulatory constraints, has positioned OWC as a compelling alternative for next generation wireless networks [1, 2].

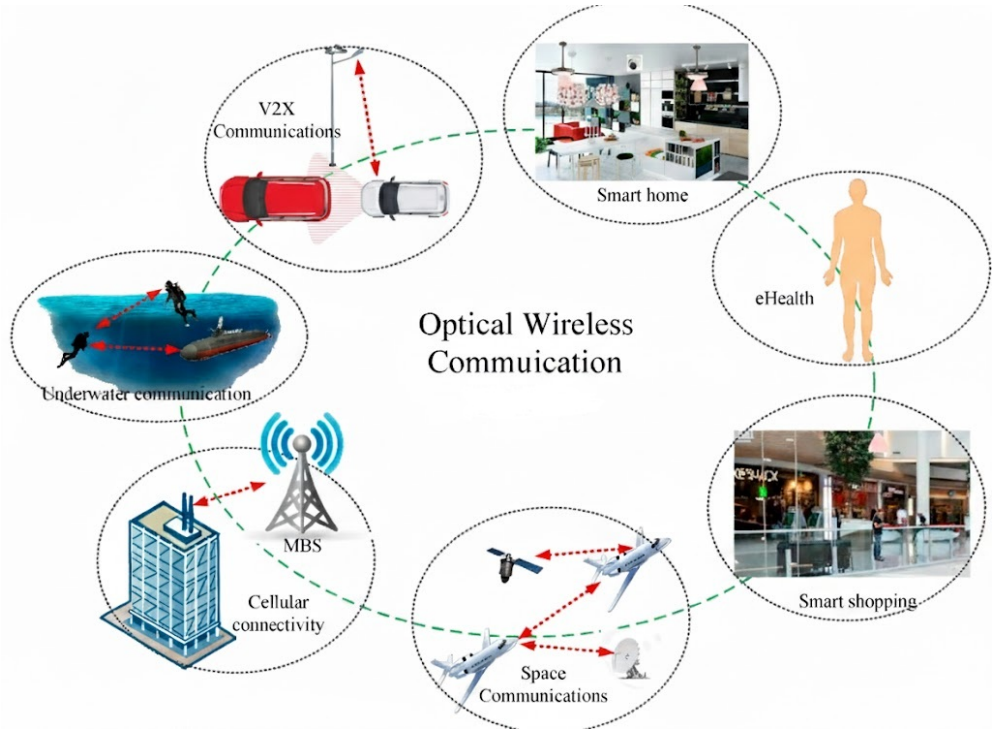

Figure 1.1: *An illustration of potential OWC network applications.*

The breadth of OWC applications spans from terrestrial to aquatic and space environments,

with some examples illustrated in Fig. 1.1. These applications include vehicle-to-everything (V2X) communications, mobile base station (MBS) connectivity for cellular network backhaul, underwater communication systems, smart home automation, electronic health (eHealth) monitoring, smart shopping retail environments, space communications for satellite links, and etc. Each application domain leverages the unique advantages of optical wireless links whilst confronting distinct environmental and operational challenges.

The fundamental advantage of OWC systems lies in their exploitation of the vast unlicensed optical spectrum, spanning more than 400 THz of bandwidth compared to the severely congested RF spectrum below 300 GHz [3], as presented in Fig. 1.2. This immense spectral resource enables OWC systems to achieve data rates exceeding 100 Gbps, far surpassing the capabilities of traditional RF systems [4]. Additionally, the inherent directionality of optical beams provides enhanced security through reduced susceptibility to eavesdropping, while the immunity to electromagnetic interference makes OWC particularly attractive for deployment in electromagnetically sensitive environments such as hospitals, aircraft, and industrial facilities [2].

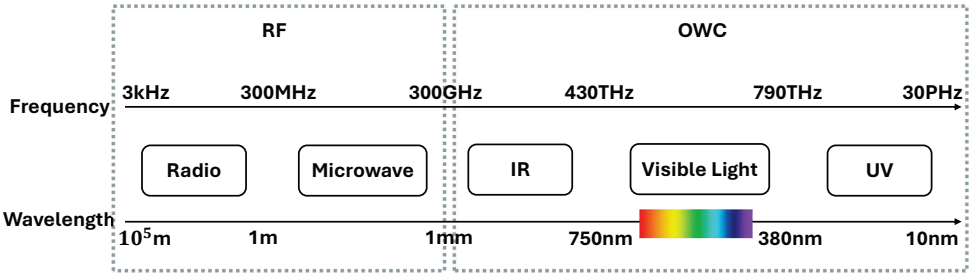

Figure 1.2: *The spectrum of RF, microwave, IR, visible light and UV bands.*

The versatility of OWC technology manifests across multiple application domains, each presenting unique opportunities and challenges. Free-space optical (FSO) communication enables high capacity backhaul connections for cellular networks, particularly in scenarios where fibre installation is impractical or cost prohibitive. Visible light communication (VLC) leverages the ubiquitous lighting infrastructure (eg. light emitting diode (LED)) to provide simultaneous illumination and communication, offering energy efficient solutions for indoor connectivity. Underwater optical wireless communications (UOWC) addresses the critical communication needs of marine applications, including autonomous underwater vehicle (AUV), ocean monitoring systems, and offshore industrial operations, where RF signals experience severe attenu-

ation [5].

However, the practical deployment of OWC systems faces significant challenges arising from the hostile effects of the propagation environment. Unlike guided optical communication through fibre cables, wireless optical signals traverse uncontrolled media that introduce various impairments including atmospheric turbulence, scattering, absorption, and dynamic misalignment between transceivers. These channel-induced effects manifest as intensity fluctuations, beam wander, and signal distortion that can severely degrade system performance and reliability.

Atmospheric turbulence, caused by temperature and pressure variations, induces random fluctuations in the refractive index along the propagation path, resulting in received optical intensity scintillation and beam wander that can cause temporary link outages and decoding errors. In underwater environments, turbulence effects are compounded by absorption and scattering from suspended particles, with additional challenges from bubbles and thermal variations. The dynamic nature of these impairments, particularly in mobile scenarios, necessitates robust communication techniques that can maintain reliable operation across varying channel conditions.

Current OWC systems typically address these challenges through isolated approaches, such as forward error correction (FEC) coding, adaptive optics, or diversity techniques. However, these solutions often provide limited performance gains and may be insufficient for next generation applications requiring ultra reliable and low latency communication. The increasing deployment of OWC in various applications, including autonomous vehicle communication, emergency response networks, and industrial automation, demands more robust approaches that address multiple impairment sources simultaneously.

Conventional OWC systems have predominantly relied on amplitude-based modulation schemes such as on-off keying (OOK) and pulse amplitude modulation (PAM) [6, 7]. Although these schemes are straightforward to implement, they encode information in the amplitude of the optical signal and are therefore inherently susceptible to turbulence-induced amplitude fading. Random intensity fluctuations caused by thermal gradients, salinity variations, and air bubble formation directly corrupt the received amplitude, leading to degraded BER and link outages under moderate to strong turbulence conditions. Overcoming this limitation calls for modulation strategies that do not rely on amplitude as the primary information-bearing dimension. To this end, this thesis proposes frequency-based modulation schemes, namely

frequency-shift keying (FSK)-subcarrier intensity modulation (SIM) and frequency-shift chirp modulation (FSCM) combined with polarisation division multiplexing (PDM), alongside an active beam tracking system and feedback-free adaptive transmission strategies. Together, these contributions help to overcome the amplitude-fading vulnerability and enhance link robustness across both UOWC and FSO channels.

This thesis addresses the fundamental challenge of establishing robust OWC links in hostile channel conditions through comprehensive approaches that encompass resilient modulation techniques, intelligent tracking system, adaptive transmission strategies, and integrated sensing capabilities. The research scope extends across multiple OWC domains, with particular emphasis on UOWC systems where channel impairments are most severe, and FSO systems where practical deployment challenges are most pronounced.

1.2 Objectives

The primary objective of this thesis is to develop and demonstrate novel and practical techniques for enhancing the robustness of OWC systems against hostile channel effects, thereby enabling reliable high speed wireless communication in challenging propagation environments. This overarching goal is achieved through the following specific research objectives:

Objective 1: Development of Resilient Modulation Schemes - To investigate and develop robust modulation techniques that exploit multiple signal dimensions to provide inherent resilience against channel-induced impairments. This includes the empirical evaluation of frequency-based modulation schemes, including FSK implemented by SIM and FSCM, combined with PDM to achieve enhanced robustness whilst maintaining competitive spectral efficiency.

Objective 2: Design of fine Tracking Systems - To develop real-time beam tracking mechanisms that actively compensate for dynamic misalignment effects in mobile OWC scenarios. This encompasses the design of photodetector array-based sensing systems, control algorithms for precision beam steering, and experimental validation of tracking performance under various misalignment conditions.

Objective 3: Implementation of Adaptive Transmission Strategies - To create intelligent adaptation mechanisms that dynamically optimise system parameters based on real-time channel conditions. This includes the development of camera-based channel estimation techniques,

machine learning algorithms for parameter optimisation, and adaptive power control strategies that maximise throughput whilst maintaining reliability constraints.

Objective 4: Development of Alternative Channel State Estimation Techniques - To explore more accurate and efficient approach for channel state information (CSI) acquisition in OWC systems. This involves investigating retroreflector-based architectures that leverage polarisation transformations for direct channel monitoring whilst maintaining primary communication functions.

Objective 5: Experimental Validation and Performance Characterisation - To provide comprehensive experimental validation of proposed techniques through laboratory demonstrations and field trials. This includes the development of testbed platforms, performance evaluation under realistic channel conditions, and comparison with existing state-of-the-art approaches.

These objectives collectively address the multifaceted nature of channel robustness in OWC systems, ranging from physical layer innovations to system level architectural enhancements. The research approach emphasises practical implementation feasibility whilst maintaining theoretical rigour, ensuring that proposed solutions are both scientifically sound and deployable in real-world scenarios.

1.3 Contributions and Publications

1.3.1 Contributions to Knowledge

This thesis presents both theoretical understanding and practical implementation to the field of robust optical wireless communication:

Experimental work for Frequency-Based Modulation with PDM: A comprehensive empirical investigation of frequency-based modulation schemes combined with polarisation division multiplexing for enhanced robustness in turbulent UOWC channels. The research demonstrates that FSK-SIM and FSCM, when combined with PDM, achieve up to 6 dB improvement in receiver sensitivity under strong turbulence conditions whilst doubling spectral efficiency.

Real-Time Beam Tracking Architecture: Development of a novel fine tracking system architecture employing photodetector arrays and fast steering control for dynamic misalignment

compensation in FSO links. The proposed system achieves sub-millisecond response times and maintains link availability under beam displacement scenarios that would cause complete link failure in untracked systems.

Adaptive Camera-Based Channel State Estimation: Introduction of machine learning enhanced camera-based CSI estimation techniques that enable real-time adaptation for transmission parameters. The proposed approach achieves high CSI estimation accuracy and enables proactive adaptation to changing channel conditions in both turbulent UOWC and foggy FSO environments.

Retroreflector-based Channel State Estimation: Development of a CSI estimation architecture for OWC systems that exploits polarisation transformations in retroreflected signals. The framework demonstrates the feasibility of using retroreflected optical signals for real-time channel characterisation and adaptive resource allocation without requiring feedback channels or receiver modifications, validated in both turbulent UOWC and foggy FSO channels.

Practical Performance Analysis: Experimental characterisation of proposed techniques across multiple channel conditions, providing valuable insights into the practical limitations and trade-offs of robust OWC systems. The research provides empirical evidence supporting theoretical predictions and offers design guidelines for practical system deployment.

1.3.2 List of Publications

The research contributions of this thesis have been documented through peer reviewed publications in leading international journals and conference proceedings:

Journal Publications:

1. Jianhui Chen, Tilahun Zerihun Gutema, and Wasiu O. Popoola, ”Adaptive optical wireless communication systems with camera-based underwater turbulence and fog channel estimation,” Appl. Opt. 64, 4878-4886 (2025)

2. J. Chen, T. Z. Gutema and W. O. Popoola, ”Modeling, Design and Implementation of Beam Tracking for Misalignment Mitigation in Optical Wireless Communications,” in IEEE Open Journal of the Communications Society, vol. 6, pp. 9090-9099, 2025, doi: 10.1109/OJ-COMS.2025.3624621.

Journal papers 1 and 2, listed above, are associated with the findings of Chapters 6 and 5, respectively.

Conference Publications:

1. J. Chen, C. T. Geldard, E. Guler, A. Hamilton and W. O. Popoola, "An Experimental Demonstration of FSK-SIM-PDM Underwater Optical Wireless Communications," 2022 Sixth Underwater Communications and Networking Conference (UComms), Lerici, Italy, 2022, pp. 1-4, doi: 10.1109/UComms56954.2022.9905701.

2. T. Z. Gutema, J. Chen, T. Adiono and W. O. Popoola, "Comparative Study of Frequency-based Modulations for Visible Light Communication," 2024 IEEE Wireless Communications and Networking Conference (WCNC), Dubai, United Arab Emirates, 2024, pp. 1-6, doi: 10.1109/WCNC57260.2024.10571121.

3. Chen, J., Geldard, C.T. and Popoola, W.O., A Demonstration of Frequency-Based Modulation for Underwater Optical Wireless Communication. In 2023 seventh Underwater Acoustics Conference and Exhibition (UACE), Kalamata, Greece, 2023, pp. 577-584, doi: https://www.uaconferences.org/proceedings/proceedings-2023.

4. Chen, J., Gutema, T. Z., and Popoola, W. O., Beam Tracking for Misalignment Mitigation in Optical Wireless Communication. In 2025 IEEE International Symposium on Personal, Indoor and Mobile Radio Communications (PIMRC), Istanbul, Turkey, 2025.

5. The content in chapter 7 has been modified into a conference paper and submitted to IEEE 15th International Symposium on Communication Systems, Networks and Digital Signal Processing (CSNDSP), the paper is still under review.

The conference paper 1, 2, and 3 are related to the findings in chapter 4, and the conference paper 4 is related to the chapter 5. These publications demonstrate the impact and recognition of the research within the international scientific community, with contributions spanning both theoretical advances and practical implementation strategies.

1.4 Thesis Outline

This thesis is organised into eight chapters that systematically address the challenges of achieving robust OWC in hostile OWC channel environments. The structure progresses from the-

oretical foundations through specific technical contributions to comprehensive experimental validation and future perspectives.

Chapter 2: Background establishes the fundamental principles of optical wireless communication systems, providing essential theoretical background on OWC architectures, optical sources and detectors, and channel propagation characteristics.

Chapter 3: Literature Review presents a comprehensive survey of state-of-the-art robust techniques for OWC systems, analysing existing approaches to channel robustness including advanced modulation schemes, machine learning-based techniques, and system-level design strategies.

Chapter 4: Empirical Study of Frequency-Based Signalling with Polarisation Division Multiplexing investigates the combination of frequency-based modulation techniques with polarisation multiplexing to address the challenges of hostile channel and spectral efficiency in UOWC systems. The chapter presents detailed experimental evaluation of FSK-SIM and FSCM combined with PDM across various channel conditions, demonstrating superior performance compared to conventional amplitude-based schemes.

Chapter 5: Fine Tracking System for Optical Wireless Communication describes the development of a fine beam tracking system that actively compensates for dynamic misalignment in FSO scenarios. The chapter covers the theoretical modelling of misalignment effects, system architecture design, control algorithm development, and comprehensive experimental validation under both static and dynamic conditions.

Chapter 6: Adaptive Camera-Based Channel State Estimation introduces machine learning-enhanced camera-based techniques for CSI estimation and adaptive transmission optimisation. The chapter demonstrates how to use camera with machine learning and image process algorithms to extract CSI from captured images, enabling proactive adaptation to varying channel conditions across turbulent UOWC and foggy FSO environments.

Chapter 7: Retroreflector-based Channel State Estimation explores an alternative approach to CSI acquisition that complements the camera-based method in Chapter 6. The chapter presents retroreflector-based channel monitoring through polarisation analysis, implementation strategies, and experimental demonstrations in both turbulent UOWC and foggy FSO channels, achieving comparable performance improvements with reduced computational complexity.

Chapter 8: Conclusion and Outlook summarises the key findings and contributions of the thesis, discusses limitations of proposed approaches, and identifies promising directions for future research. The chapter provides a critical assessment of achieved objectives and outlines the potential impact of developed techniques on practical OWC system deployment.

Chapter 2
Background

2.1 Introduction

The development of robust OWC systems, as motivated in Chapter 1, requires thorough understanding of the fundamental physical layer principles, system components, and channel propagation characteristics that determine communication performance. This chapter introduces the theoretical foundations for comprehending the proposed robust techniques developed in subsequent chapters.

The unique characteristics of OWC systems, particularly the constraint of non-negative optical intensity and the direct detection paradigm, fundamentally differentiate them from RF systems and impose specific requirements on system design. These principles explains why conventional wireless communication techniques cannot be directly applied to optical channels and why specialised robust approaches for OWC are necessary.

This chapter describes three fundamental aspects of OWC systems. Section 2.2 presents the operational principles of intensity modulation (IM)/direct detection (DD) systems, describing the basic mathematical framework for signal transmission and reception. Section 2.3 introduces and analyses the characteristics of optical sources and photodetectors. Section 2.4 characterises the hostile channel effects in both atmospheric and underwater environments, providing the theoretical basis for understanding the robustness challenges addressed throughout this thesis. Section 2.5 introduces the modulation schemes and multiplexing techniques commonly used in OWC systems, serving as a reference for the advanced schemes reviewed in Chapter 3.

2.2 Overview of Optical Wireless Communication

The operational principle of OWC systems mainly relies on coherent OWC modulation and intensity modulation and direct detection (IM/DD). From a perspective of practice, this thesis will focus on IM/DD implementation and development, due to its simplicity, cost-effectiveness,

and compatibility with existing optoelectronic components [8]. Unlike coherent optical systems that modulate phase or frequency requiring complex transceivers, IM/DD systems encode information through variations in optical intensity, enabling direct optical signal detection without local oscillators or phase synchronisation. Figure. 2.1 presents a block diagram for a typical OWC system. The information bits are modulated and processed to the format which is proper for the driver circuit first, and then modulate the light resources (LED, laser, etc.). The light then go through the optical front ends to be reshaped or collimated for achieving the transmission distance or meeting the application requirements, and arrives at the receiver side through the OWC channel. The photodetectors (PIN, APD, etc.) convert the optical power after optical front ends at the receiver side to the electrical signal. Then the demodulation blocks retrieve the transmitted data and information and output the bits.

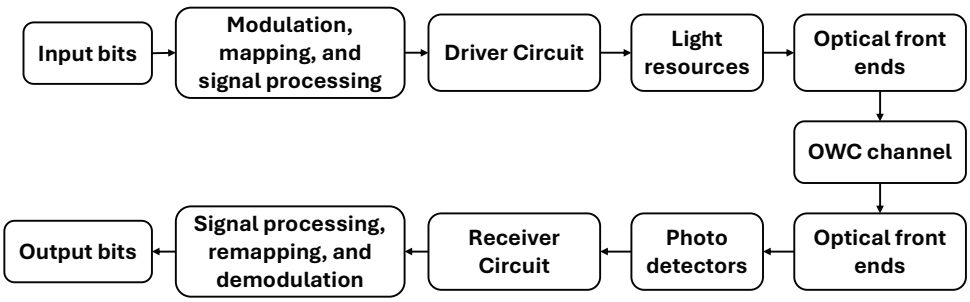

Figure 2.1: *System components of a typical OWC link*

In mathematical terms, the transmitted optical power in an IM/DD system can be expressed as [5]:

$$P_t(t) = P_{\text{ave}}[1 + \beta m(t)], \quad 0 \leq \beta \leq 1, \tag{2.1}$$

where P_{ave} denotes the average transmitted optical power, β represents the modulation index determining modulation depth, and $m(t)$ is the modulated electrical signal satisfying $|m(t)| \leq 1$ to ensure non-negative optical power [5]. The constraint on non-negative intensity fundamentally differentiates OWC from RF systems, imposing unique requirements on modulation formats and signal processing techniques.

The received electrical signal after photodetection and channel propagation follows [9]:

$$y(t) = \mathscr{R} P_t(t) \otimes h(t) + n(t), \tag{2.2}$$

where $\mathscr{R}$ represents photodetector responsivity, $h(t)$ denotes the channel impulse response incorporating all propagation effects, $\otimes$ indicates convolution, and $n(t)$ encompasses various noise sources including thermal noise, shot noise, and ambient light interference [9].

OWC systems span multiple application domains, each characterised by distinct propagation environments, performance requirements, and implementation constraints. FSO communication operates through atmospheric channels for terrestrial and space applications, achieving data rates exceeding 100 Gbps over kilometres with narrow beam divergence angles below 1 mrad [2]. UOWC exploits the blue-green spectral window (450-550 nm) where seawater exhibits minimum attenuation, enabling high-speed submarine communications with data rates reaching 30 Gbps in laboratory demonstrations [10]. VLC utilises solid-state lighting infrastructure for dual-purpose illumination and communication, particularly attractive for indoor environments where LED penetration exceeds 90% [11].

The wavelength selection for OWC systems depends critically on application requirements and channel characteristics. OWC with using ultraviolet light (200-280 nm) enables non-line-of-sight scattering communication with enhanced security due to strong atmospheric absorption preventing long-range eavesdropping [12]. Visible light systems (380-780 nm) leverage existing illumination infrastructure, achieving spectral efficiencies exceeding 5 bits/s/Hz through advanced modulation [13]. OWC with infrared light (780-1600 nm) provides eye-safe operation at higher power levels, with atmospheric transmission windows at 850, 1330, and 1550 nm offering reduced attenuation below 0.2 dB/km in clear conditions [14].

2.3 Optical Sources and Detectors

The performance and reliability of OWC systems fundamentally depend on the semiconductor optical sources and photodetectors that enable optical-to-electrical and electrical-to-optical conversion.

2.3.1 Light Emitting Diodes

LEDs constitute the primary optical sources for short range OWC applications, particularly VLC systems, owing to their functionality for illumination and communication, energy efficiency exceeding 150 lumens per watt, and operational lifetimes surpassing 50,000 hours [15].

The emission mechanism in LEDs involves spontaneous recombination of electron-hole pairs across the semiconductor bandgap, producing incoherent light with Lambertian radiation patterns suitable for wide area coverage [16]. As shown in Fig. 2.2, this process occurs within a forward-biased PN junction, where electrons from the N-type region and holes from the P-type region are injected across the depletion region. When these minority carriers recombine in the active region, the energy equal to the bandgap energy $E_g = h\nu$ is released as a photon, where h is Planck's constant and ν is the optical frequency [3]. The emission wavelength is therefore determined by the semiconductor material composition, with common materials including GaAs for infrared emission (850-940 nm), AlGaInP for red and amber LEDs (620-650 nm), and InGaN for blue and green LEDs (450-550 nm) [17].

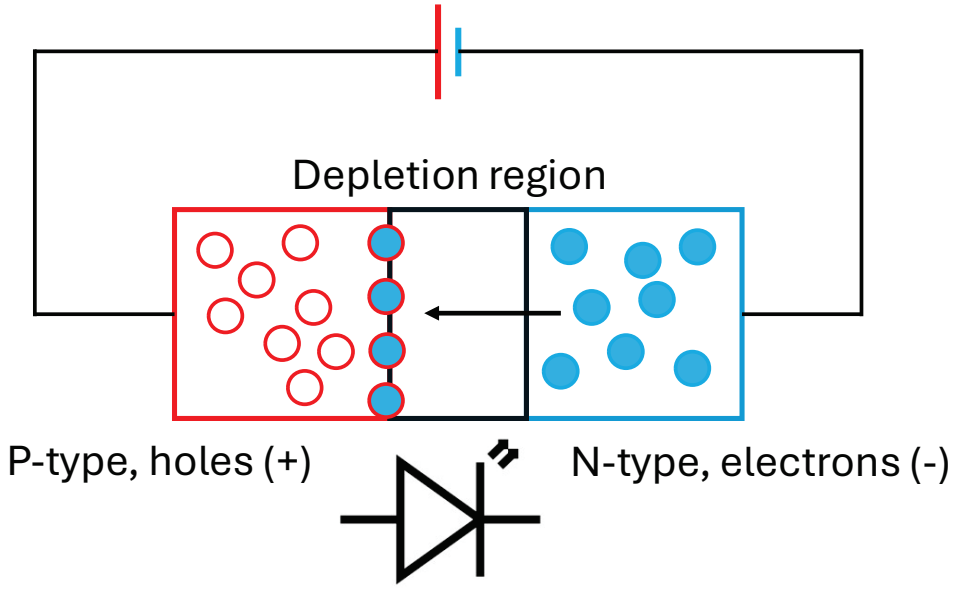

Figure 2.2: *LED under forward bias condition.*

The spectral characteristics of LED emission follow from the energy distribution of carriers and the density of states in the semiconductor, resulting in spectral width [18]:

$$\Delta\lambda = \frac{1.8kT\lambda^2}{hc}, \tag{2.3}$$

where k represents Boltzmann's constant, T denotes junction temperature, λ is the centre wavelength, h is Planck's constant, and c represents the speed of light [18]. This relatively broad spectral width (typically 20-50 nm) provides immunity to chromatic dispersion but limits spec-

tral efficiency in wavelength division multiplexing applications [3].

The modulation bandwidth of conventional phosphor-converted white LEDs remains fundamentally constrained by the slow phosphor response time, limiting direct modulation to approximately 3-20 MHz [9]. Advanced LED architectures have been developed to overcome bandwidth limitations. Micro-LEDs (μ-LEDs) with active areas below 100 μm^2 achieve modulation bandwidths exceeding 1 GHz through reduced junction capacitance and enhanced carrier extraction [19].

2.3.2 Laser (Light Amplification by Stimulated Emission of Radiation)

Semiconductor laser diodes (LD) provide high performance characteristics for long-range and high-speed OWC applications through stimulated emission, offering coherent output with spectral line widths below 1 nm, modulation bandwidths exceeding 25 GHz, and wall-plug efficiencies approaching 70% [20]. Unlike LEDs which rely on spontaneous emission, laser diodes use heavily doped PN junctions with heterostructure designs that create quantum wells to confine carriers and photons [17]. Under sufficient forward bias, the injected carrier density in the active region exceeds the transparency level, achieving population inversion where the probability of stimulated emission exceeds absorption [3]. Figure. 2.3 demonstrates the PN junction in laser, which is similar to LED, but there is two different reflecting surfaces to ensure photons radiated spatially coherent. After recombinations between holes and electrons, the emitted photons will enter a cavity where they are reflected between two mirrors in order to repeat the stimulated emission process. One mirror has a reflectance close to 100% whilst the other is much lower, meaning most of photons may escape from one side only and the residual light will go another side. Thus, the emitted photons from laser become spatially coherent due to the bounce between these mirrors in the cavity.

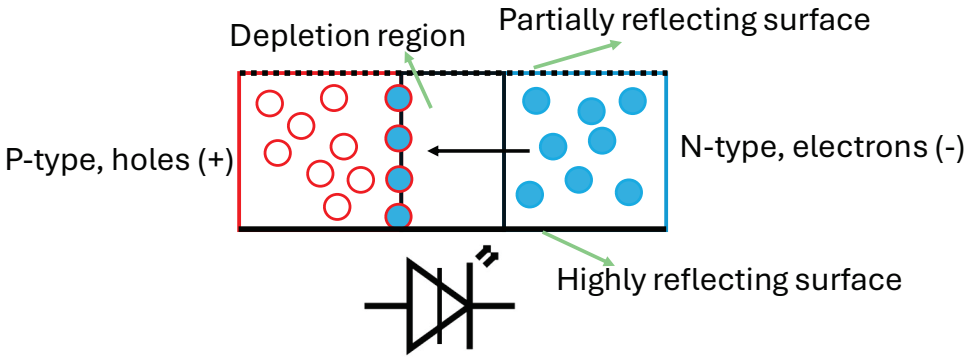

Figure 2.3: *Laser under forward bias condition.*

Vertical-cavity surface-emitting laser (VCSEL)s have emerged as particularly attractive sources for OWC, providing circular beam profiles with divergence angles below 10°, single-mode operation with side-mode suppression ratios exceeding 30 dB, and array integration capability for spatial multiplexing [21]. The coherent nature of laser emission enables advanced modulation formats including coherent detection schemes, but with increased system complexity [20]. Recent demonstrations of injection-locked VCSELs have achieved modulation bandwidths exceeding 40 GHz, enabling data rates approaching 100 Gbps in laboratory settings [22].

2.3.3 Photodetectors

Photodetection in OWC systems converts incident optical power to electrical signals through various mechanisms depending on device architecture. When photodiodes operate under reverse bias conditions, the electric field in the depletion region separates photo-generated electron-hole pairs before recombination [3], as shown in Fig. 2.4. When a photon with energy $h\nu \geq E_g$ is absorbed in the depletion region or within a diffusion length of it, the resulting electron-hole pair is swept apart by the built-in electric field, generating photocurrent proportional to incident optical power [23].

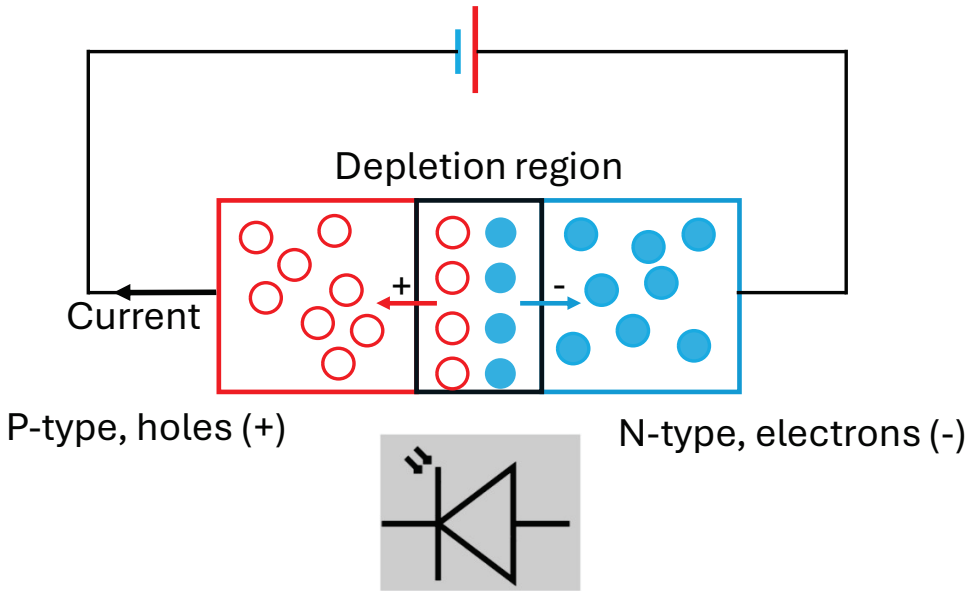

Figure 2.4: *PIN photodiode under reverse bias condition.*

PIN photodiodes remain the major option of OWC receivers, especially in IM/DD, offering predictable performance with bandwidths determined by the transit time-bandwidth product [24]:

$$f_{-3\text{dB}} = \frac{0.44 v_s}{w}, \tag{2.4}$$

where v_s represents carrier saturation velocity and w denotes depletion region width [24]. The PIN structure inserts a lightly doped intrinsic (I) region between the P and N regions, creating a wide depletion region with uniform electric field that maximises the absorption volume and carrier drift velocity whilst minimising junction capacitance. Commercial PIN photodiodes achieve bandwidths exceeding 10 GHz with active areas optimised for specific applications [25].

APDs provide internal gain through impact ionisation, achieving multiplication factors described by [23]:

$$G_{\text{APD}} = \frac{1}{1 - \left(\frac{V_R}{V_B}\right)^{k_{\text{APD}}}}, \tag{2.5}$$

where V_R represents reverse bias voltage, V_B denotes breakdown voltage, and k_{APD} ranges from 2-6 depending on semiconductor material [23]. In the high-field multiplication region of the

APD structure, photo-generated carriers gain sufficient kinetic energy from the electric field to create secondary electron-hole pairs through collision with lattice atoms, resulting in avalanche multiplication [24]. The process continues until carriers exit the multiplication region, with the total gain determined by the ionisation coefficients for electrons (α) and holes (β_{APD}). However, the gain-bandwidth product limitation and excess noise factor described by McIntyre's formula $F(G_{\text{APD}}) = k_{\text{eff}}G_{\text{APD}} + (1-k_{\text{eff}})(2-1/G_{\text{APD}})$ (where $k_{\text{eff}} = \beta_{\text{APD}}/\alpha$ represents the ionisation coefficient ratio) requires careful optimisation for specific applications [26].

There are two more types of detectors that will be introduced due to their use in state of the art works discussed below, they are the single photon avalanche diode (SPAD), and the photon multiplier tube (PMT). These are both high gain detectors useful with very weak received signals [27]. The SPAD is similar to an APD but is operated in the Geiger region, so that a single incident photon induces an avalanche of electrical charge carriers that are directly detectable. Thus, allowing individual photons to be detected [28]. In a PMT on the other hand, a photon incident on a conducting surface causes the emission of an electron via the photo-electric effect, this electron is then accelerated towards a plate with higher electric potential. The electron has high energy due to the acceleration and, upon interaction with the plate, causes the emission of more electrons. This process is repeated in a cascade to achieve a very high gain. Both the SPAD and PMT use different processes to achieve very high gains, but both come with a trade-off of requiring a very high bias voltage and coming at a high cost. A comparison of the key characteristics of these four detector types is summarised in Table 2.1.

Detector	**Internal Gain**	**Bandwidth**	**Sensitivity**
PIN	Unity	Moderate	Moderate
APD	Moderate	Limited by gain-bandwidth product	Higher than PIN
SPAD	Very high	Limited by dead time	Single-photon
PMT	Very high	Moderate	Single-photon

Table 2.1: *Comparison of photodetector types for OWC applications.*

2.4 Channel Effects in OWC

The propagation of optical signals through various media introduces fundamental channel impairments that significantly affect the reliability and performance of OWC systems. A simpli-

fied block diagram of OWC system is presented in Fig. 2.5. When light propagates from one transceiver to another along the OWC channel, the optical beam will be affected in different ways according to the channel conditions. The main possible ways of how the light will be affected are presented in Fig. 2.6.

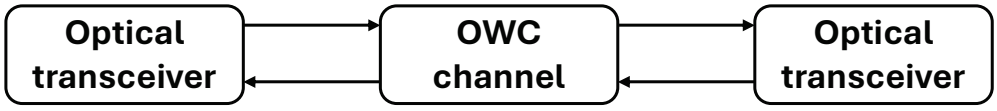

Figure 2.5: *Simple block diagram of the OWC system model.*

Reflection occurs when light encounters a boundary between two media with different refractive indices, causing the optical wave to return to the incident medium. Specular reflection from smooth surfaces obeys the Law of Reflection, where the angle of incidence equals the angle of reflection, both measured relative to the surface normal. In contrast, diffuse reflection from rough surfaces scatters incident light in multiple directions due to microscopic surface irregularities, though each individual reflection still follows the Law of Reflection locally. Transmission describes the propagation of light through a medium without change in direction, as illustrated by normal incidence where the optical beam enters perpendicularly to the interface. When light traverses an interface between media with differing refractive indices at oblique angles, refraction occurs, manifesting as a change in propagation direction. This phenomenon is governed by Snell's Law, which relates the incident and refracted angles to the refractive indices of the two media. Absorption represents the conversion of optical energy into other forms, predominantly thermal energy, through interaction with the medium's constituent molecules or atoms. The wave nature of light gives rise to diffraction, wherein electromagnetic waves bend and spread when encountering apertures or obstacles with dimensions comparable to the wavelength. Scattering describes the interaction between light and particles or density fluctuations within the medium, causing redirection of photons in various directions. The scattering characteristics, including angular distribution and polarisation dependence, are determined by particle size relative to wavelength and the refractive index contrast between scatterers and the surrounding medium.

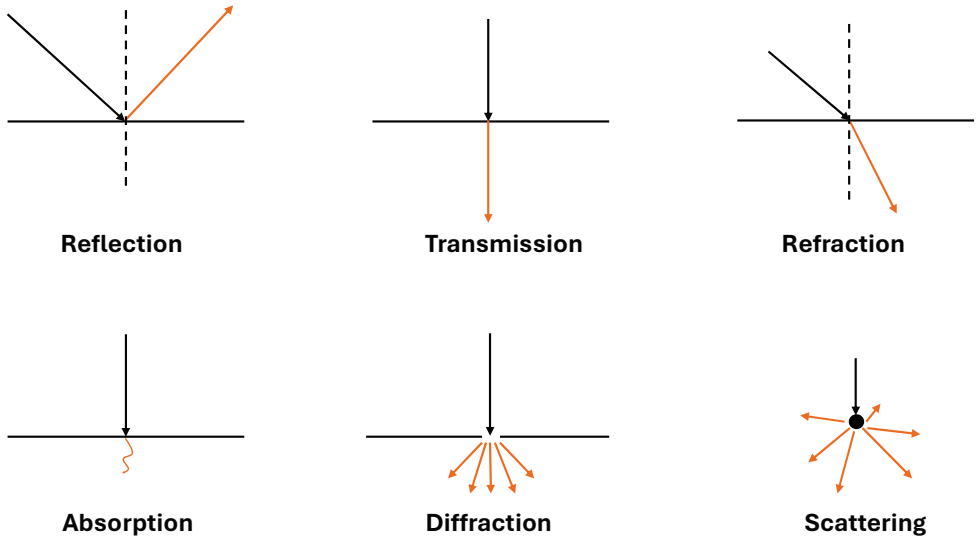

Figure 2.6: *A demonstration of light behaviour along the propagation path.*

In this thesis, the FSO and UOWC channel will be investigated. And understanding these channel effects is important for developing robust communication strategies and system designs that can maintain reliable links under diverse environmental conditions.

2.4.1 Free-space Optical Channel

Atmospheric optical channels exhibit complex propagation characteristics dominated by molecular and aerosol interactions, atmospheric turbulence, and weather phenomena that collectively determine link availability and performance [29–32]. The fundamental challenge in FSO communication arises from the dynamic nature of atmospheric conditions, which can vary on timescales ranging from microseconds for turbulence effects to hours for weather pattern changes, necessitating adaptive system designs capable of maintaining reliable connectivity. The atmospheric channel introduces both deterministic losses through absorption and scattering mechanisms, and stochastic variations through turbulence-induced refractive index fluctuations that cause beam spreading, wandering, and intensity scintillation [33].

The received power in FSO systems follows the modified link budget equation [14]:

$$P_r = P_t \eta_t \eta_r \left(\frac{D_r}{D_t + \theta L} \right)^2 \exp(-\alpha_{\text{atten}} L) \mathscr{L}_{\text{turb}}, \tag{2.6}$$

where η_t and η_r represent transmitter and receiver optical efficiencies, D_r denotes receiver aperture diameter, D_t is transmitter aperture, θ represents beam divergence, α_{atten} accounts for atmospheric attenuation, and $\mathscr{L}_{\text{turb}}$ represents turbulence-induced losses [14].

Atmospheric attenuation arises from wavelength-dependent absorption by molecular constituents including water vapour, carbon dioxide, oxygen, and ozone, combined with scattering by aerosol particles suspended in the atmosphere. The molecular absorption creates distinct transmission windows in the near-infrared spectrum at 850 nm, 1330 nm, and 1550 nm, where atmospheric losses are minimised to below 0.2 dB/km under clear conditions [34]. Aerosol scattering, predominantly through Mie scattering mechanisms for particles comparable to optical wavelengths, exhibits strong dependence on atmospheric visibility and weather conditions. For wavelengths between 550-1550 nm, the attenuation coefficient follows Kruse and Kim model [35–38]:

$$\alpha_{\text{atten}} = \frac{3.91}{V}\left(\frac{\lambda}{550}\right)^{-q_{\text{vis}}}, \tag{2.7}$$

where V represents visibility in kilometres and q_{vis} depends on visibility conditions, the relationship between V and q_{vis} is shown in Table 2.2 [35–37].

Visibility Range (V)	**Condition**	**Value of q_{vis}**
$V \geq 50$ km	High Visibility	1.6
6 km $< V <$ 50 km	Average Visibility	1.3
1 km $< V <$ 6 km	Haze	$0.16V + 0.34$
0.5 km $< V <$ 1 km	Mist / Fog	$V - 0.5$
$V <$ 0.5 km	Dense Fog	0

Table 2.2: *Values of q_{vis} for different visibility ranges V*

Atmospheric turbulence induces refractive index fluctuations through temperature and pressure variations along the propagation path, creating a spatially and temporally varying channel [39]. The turbulence effects manifest as beam spreading beyond diffraction limits, beam wandering causing pointing errors, and intensity scintillation producing temporal fading and received intensity fluctuation that can exceed 20 dB in strong turbulence conditions.

2.4.2 Underwater Optical Wireless Channel

The underwater optical channel presents unique propagation challenges characterised by strong wavelength-dependent attenuation, multiple scattering from suspended particles, turbulence from temperature and salinity gradients, and background noise from solar radiation and bioluminescence [40]. The optical properties of seawater vary significantly with geographic location, depth, seasonal biological activity, and proximity to coastal regions, creating a highly heterogeneous communication medium that requires adaptive system designs. Unlike atmospheric channels where transmission windows exist across broad spectral regions, underwater channels exhibit a narrow blue-green transmission window between 450-550 nm where seawater absorption is minimised, fundamentally constraining wavelength selection for UOWC systems [41].

The reliability of UOWC links is primarily affected by two phenomena: underwater turbidity and underwater turbulence [42].

Underwater turbidity, caused by suspended organic and inorganic particles including phytoplankton, zooplankton, mineral sediments, and dissolved organic matter, degrades optical signals through both absorption and scattering processes. Absorption converts photon energy into other forms such as heat or chemical energy, leading to exponential signal attenuation with distance that fundamentally limits transmission range. Scattering deflects photons from their original propagation paths, with forward scattering dominating in most natural waters due to particle sizes typically exceeding optical wavelengths. Multiple scattering events cause temporal pulse dispersion that limits achievable data rates, spatial beam spreading that reduces received power, and depolarisation effects that degrade polarisation-based modulation schemes [5, 43].

The total attenuation coefficient combines absorption and scattering effects from multiple constituents [44]:

$$c(\lambda) = a(\lambda) + b(\lambda) = a_w(\lambda) + a_p(\lambda) + a_{CDOM}(\lambda) + b_w(\lambda) + b_p(\lambda), \tag{2.8}$$

where subscripts w, p, and CDOM denote water, particles, and coloured dissolved organic matter respectively [44].

Pure seawater exhibits minimum absorption near 420 nm at approximately 0.015 m^{-1}, establishing the fundamental limit for optical transmission in marine environments. The absorp-

tion increases rapidly outside the blue-green window, exceeding 1 m^{-1} at wavelengths below 400 nm due to dissolved salts and above 600 nm due to water molecule vibrational overtones. Molecular scattering in pure water follows [45]:

$$b_w(\lambda) = 0.00111 \left(\frac{400}{\lambda} \right)^{4.32}, \tag{2.9}$$

providing the fundamental scattering limit for UOWC performance [45].

Natural waters exhibit substantially higher attenuation than pure seawater due to biological and geological constituents. Phytoplankton containing chlorophyll-a introduces strong absorption peaks at 440 nm and 675 nm, with concentrations ranging from below 0.01 mg/m³ in oligotrophic open ocean waters to exceeding 10 mg/m³ in eutrophic coastal waters during algal blooms. Coloured dissolved organic matter (CDOM), primarily from decaying plant material, causes exponentially increasing absorption towards shorter wavelengths, significantly affecting coastal and harbour waters. Suspended sediments from riverine inputs and bottom resuspension in shallow waters increase both absorption and scattering, with particle size distributions determining the angular scattering pattern and polarisation properties [46].

Underwater turbulence arises from small-scale random variations in refractive index along the propagation path, mainly caused by temperature, bubbles, and salinity variations in the ocean [10]. Figure 2.7 illustrates this process: on the left, the optical beam propagates as straight, parallel wavefronts representing an undistorted plane wave; in the centre, the beam encounters turbulent eddies characterised by random refractive index fluctuations; on the right, the originally straight wavefronts emerge distorted and irregular as a result of the spatially varying refraction through the eddies. These wavefront distortions manifest at the receiver as random fluctuations in received optical intensity, a phenomenon known as scintillation. These variations result from mixing processes including internal waves, current shear, and convective instabilities, creating refractive index fluctuations that cause beam wander, spreading, and intensity scintillation analogous to atmospheric turbulence but with distinct spectral characteristics [7, 47–49].

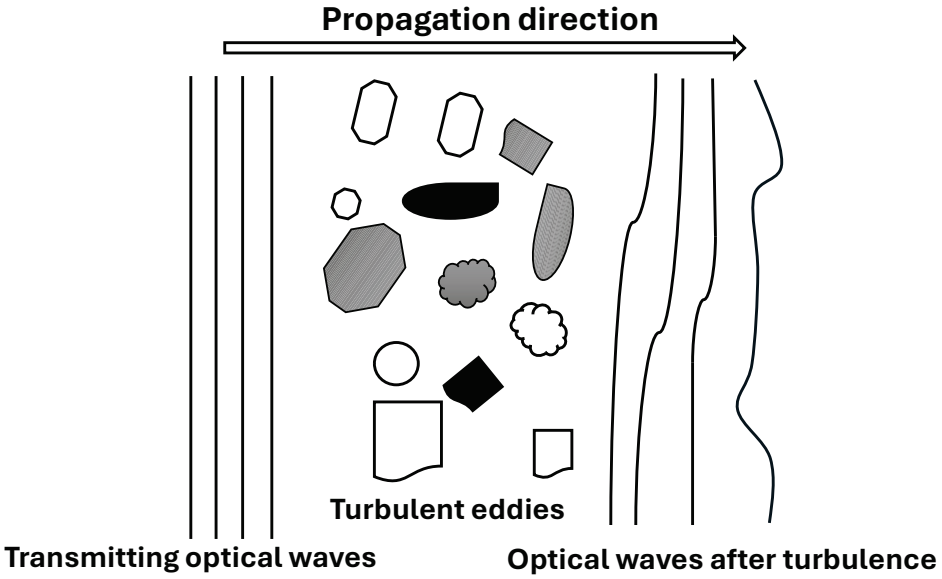

Figure 2.7: *Visualisation of optical waves travelling through OWC channel with turbulent eddies present where the resultant output optical waves are refracted.*

In OWC, these facts in turn cause the refractive index along the link to fluctuate, causing the beam to deviate from its original trajectory. The resultant fluctuations in the received optical intensity, I, can be quantified by the scintillation index (SI), σ_I^2, as [5]:

$$\sigma_I^2 = \frac{\langle I^2 \rangle - \langle I \rangle^2}{\langle I \rangle^2}, \tag{2.10}$$

where $\langle . \rangle$ represents the ensemble average. A higher value of σ_I^2 means there is a greater degree of turbulence induced fading within the channel.

2.5 Modulation Schemes and Multiplexing Techniques in OWC

The development of modulation techniques resilient to channel impairments represents a fundamental approach to enhancing OWC system robustness. Traditional amplitude modulation schemes, whilst simple to implement, show varying degrees of susceptibility to turbulence-induced fading and noise. This has driven research into advanced modulation formats that exploit multiple signal dimensions to provide inherent channel resilience [7].

Conventional modulation techniques such as OOK and M-ary PAM have been studied due to their implementation simplicity and compatibility with IM/DD systems [13, 50–52]. OOK, as the most straightforward binary modulation scheme, encodes digital information through the presence or absence of optical pulses. Its widespread adoption in VLC and FSO systems stems from minimal implementation complexity, requiring only simple threshold detection at the receiver without complicated signal processing. OOK achieves a spectral efficiency of 1 bit/s/Hz with minimal computational requirements, making it attractive for low-complexity implementations. However, its energy inefficiency becomes problematic in power constrained scenarios [53]. The unipolar nature of OOK results in suboptimal power efficiency, as the average transmitted power is only half the peak power for equally probable symbols. More critically, OOK's reliance on amplitude encoding renders it highly susceptible to turbulence-induced fading in FSO links and multipath-induced amplitude distortions in indoor VLC scenarios, limiting its applicability in challenging environments such as underwater or long-range free-space optical communications [7, 50]. The time-domain representation of the OOK signal is mathematically expressed as [3]:

$$s(t)_{\text{OOK}} = Ap(t), \quad 0 \leq t \leq T_b \tag{2.11}$$

where $A \in \{0, 1\}$ represents the binary data bit, $p(t)$ denotes the pulse shaping function, and T_b is the bit duration. Figure 2.8 illustrates a typical OOK modulated signal in the time domain. For illustrating, each symbol will last one second in the figure, as same as the following illustration figures. Under additive white Gaussian noise (AWGN) channel conditions, the theoretical BER performance of OOK with optimal threshold detection is given by [3]:

$$BER_{\text{OOK}} = Q\left(\sqrt{\frac{E_b}{N_0}}\right) \tag{2.12}$$

where $Q(\cdot)$ represents the Gaussian Q-function, E_b denotes the energy per bit, and N_0 is the single-sided noise power spectral density.

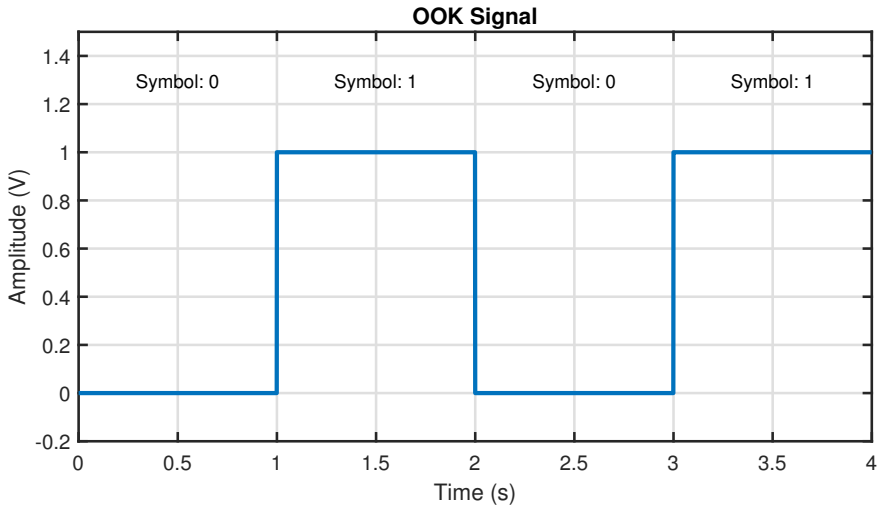

Figure 2.8: *OOK modulated signal in time domain.*

In addition, M-PAM offers improved spectral efficiency of $\log_2 M$ bit/s/Hz, though this improvement comes at the expense of signal-to-noise-ratio (SNR) requirements that increases with higher modulation order. By utilising M distinct amplitude levels, PAM extends beyond the binary limitation of OOK, enabling transmission of $\log_2 M$ bits per symbol. For IM/DD systems, all amplitude levels must satisfy the non-negativity constraint, with levels typically uniformly spaced to simplify implementation. The time-domain representation of M-PAM is expressed as [13]:

$$s(t)_{\text{M-PAM}} = A_m p(t), \quad 0 \leq t \leq T_s \tag{2.13}$$

where $A_m \in \{A_1, A_2, \ldots, A_M\}$ represents the m-th amplitude level ($m = 1, 2, \ldots, M$), $p(t)$ is the pulse shaping function, and T_s denotes the symbol duration. Figure 2.9 illustrates a 4-PAM signal in the time domain, where four distinct amplitude levels encode two bits per symbol. The theoretical BER performance of M-PAM under AWGN conditions is approximated as [13]:

$$BER_{\text{M-PAM}} = \frac{M-1}{M \log_2(M)} Q\left(\sqrt{\frac{(6 \log_2(M)) E_b}{(M^2-1) N_0}}\right) \tag{2.14}$$

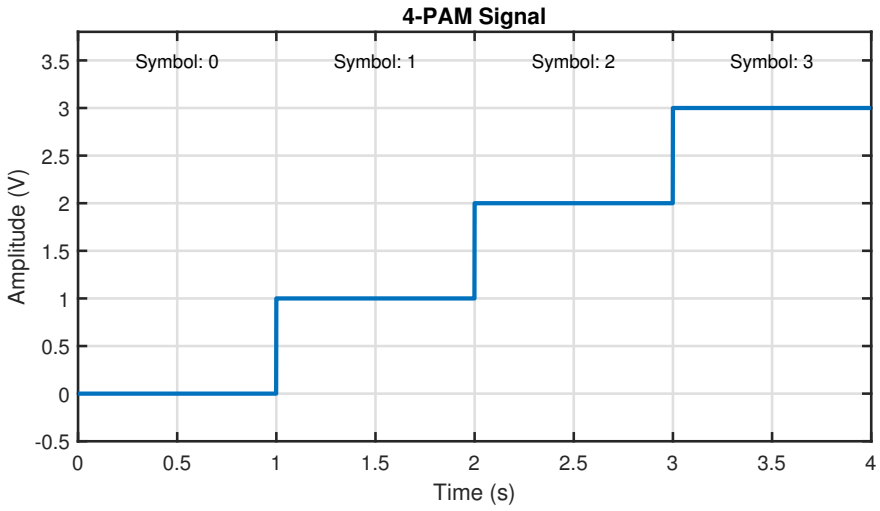

Figure 2.9: *4-PAM modulated signal in time domain.*

Experimental studies have demonstrated that 4-PAM requires approximately 5 dB additional SNR compared to OOK for equivalent BER performance in turbulent channels as reported in [50]. This SNR penalty escalates with higher modulation orders, as the reduced inter-level spacing increases susceptibility to noise and channel impairments. Beyond theoretical AWGN limitations, practical M-PAM implementations confront the nonlinear transfer characteristics of LEDs and laser diodes, which induce amplitude distortions that manifest as unequal spacing between received amplitude levels. These nonlinearities disproportionately affect higher-order PAM, resulting in error probability degradation that can be partially mitigated through pre-distortion techniques and adaptive equalization, albeit at increased system complexity [52]. Despite these challenges, M-PAM remains attractive for bandwidth limited VLC applications due to the moderate spectral efficiency improvements compared to OOK.

Orthogonal modulation techniques, particularly M-ary pulse position modulation (PPM) and M-FSK, present alternative trade-offs between power and bandwidth efficiency [54–56]. In M-PPM, information is encoded through the temporal position of a pulse within a symbol period divided into M time slots, providing inherent orthogonality between symbols that enhances robustness to certain channel impairments. PPM demonstrates higher power efficiency with increasing M, achieving up to 5 dB improvement over OOK at $M = 16$, albeit with bandwidth expansion by a factor of $M/\log_2 M$ as derived in [56]. This power efficiency advantage is from the fact that for a given symbol energy, the required E_b/N_0 for reliable detection decreases with increasing M, as reflected in the BER expression. Nevertheless, PPM's high peak-to-mean

optical power ratio and sensitivity to synchronisation errors necessitate complex equalisation techniques, limiting its practical deployment [57]. The strict slot-level timing requirements are particularly vulnerable to atmospheric turbulence, which induces temporal pulse spreading that blurs slot boundaries and directly translates to symbol errors. The time-domain representation of M-PPM is expressed as:

$$s_{\text{M-PPM}}(t) = \sqrt{\frac{2E_s}{T_s}} \sum_{n=-\infty}^{\infty} p(t - nT_s - \alpha_n T_s/M) \tag{2.15}$$

where E_s is the symbol energy, T_s is the symbol duration, and $\alpha_n \in \{0, 1, \ldots, M-1\}$ determines the slot position for the n-th symbol. The rectangular pulse shape is defined as:

$$p(t) = \begin{cases} 1, & 0 \leq t \leq T_s/M \\ 0, & \text{otherwise} \end{cases} \tag{2.16}$$

Figure 2.10 illustrates the distinctive structure of 4-PPM modulation, where the pulse position within four equally-sized slots conveys 2 bits of information per symbol. With maximum likelihood detection in AWGN channels, the BER performance is given by [56]:

$$BER_{\text{M-PPM}} = \frac{M}{2} Q\left(\sqrt{\log_2(M)\frac{E_b}{N_0}}\right) \tag{2.17}$$

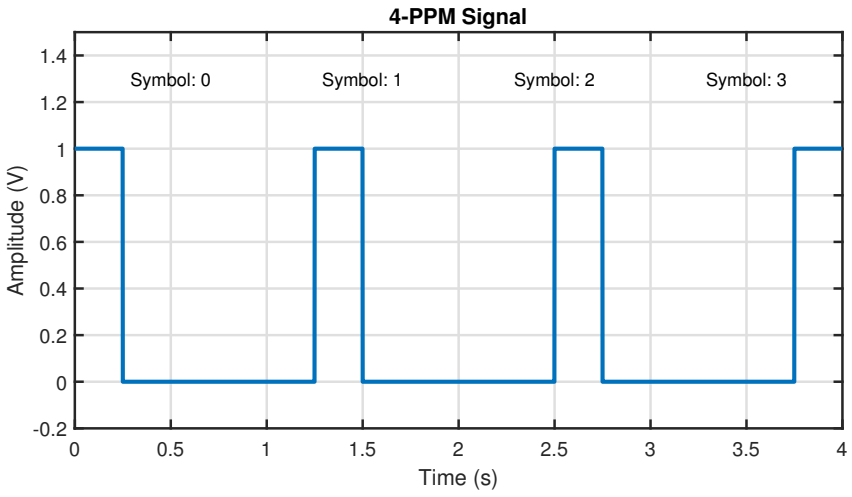

Figure 2.10: *4-PPM modulated signal in time domain.*

FSK maintains a constant envelope characteristic that simplifies transmitter design and provides inherent robustness to amplitude fluctuations induced by turbulence [51, 58]. By encoding information in the frequency domain rather than amplitude, FSK effectively decouples data transmission from intensity variations, offering significant advantages in fading channels. In M-FSK, M distinct frequencies are employed, with frequency separation typically chosen to ensure orthogonality between symbols, thereby minimising inter-symbol interference. The time domain representation of an M-FSK modulated signal is given as [51]:

$$s(t)_{\text{M-FSK}} = \sqrt{\frac{2E_s}{T_s}} \cos(2\pi f_m t + \theta), \quad 0 \leq t \leq T_s \tag{2.18}$$

where E_s is the symbol energy, f_m is the frequency of the m-th symbol ($m = 1, 2, \ldots, M$), θ is the phase of the sinusoidal carrier, and T_s is the symbol duration. Figure 2.11 shows the time domain representation of 2-FSK and 4-FSK modulated signals where 2 and 4 distinct frequencies can be observed, respectively. FSK decoding can be carried out coherently or non-coherently through matched filtering and envelope detection. The BER for non-coherent orthogonal M-FSK is given as [51]:

$$BER_{\text{M-FSK}_{\text{Non-coherent}}} = \sum_{n=1}^{M-1} (-1)^{n+1} \binom{M-1}{n} \frac{1}{n+1} \exp\left(-\frac{n k_b E_b}{(n+1)N_0}\right) \tag{2.19}$$

where $k_b = \log_2(M)$ is the number of bits per symbol.

Recent implementations of FSK in VLC systems have demonstrated energy-efficient operation for IoT applications, achieving reliable communication at SNR levels 3 dB lower than comparable OOK systems [59]. The non-coherent detection approach, whilst sacrificing approximately 1-2 dB in SNR performance compared to coherent detection, eliminates the need for carrier phase recovery and significantly reduces receiver complexity. This simplicity, combined with amplitude-fading immunity, positions FSK as an attractive candidate for robust OWC systems operating under hostile channel conditions, particularly where implementation complexity needs to be minimised.

However, the performance of FSK is sensitive to the frequency-selected channel. And to address this, FSCM, also known as chirp spread spectrum (CSS) in RF, has been adapted from Long Range (LoRa) communications for optical wireless applications [60, 61]. FSCM linearly

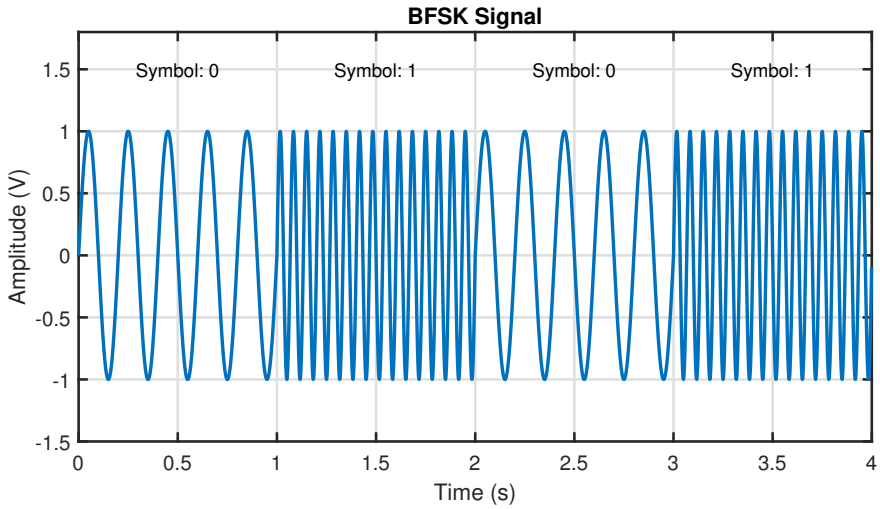

(a) *2-FSK modulated signal*

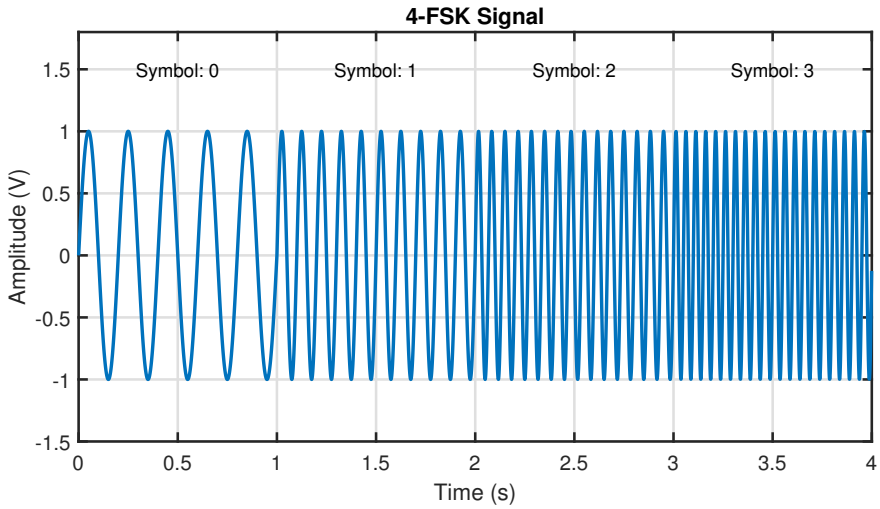

(b) *4-FSK modulated signal*

Figure 2.11: *FSK modulated signal in time domain*

sweeps the instantaneous frequency across the available bandwidth, providing inherent frequency diversity that mitigates selective fading effects. Theoretical analysis reveals that FSCM achieves a processing gain proportional to the time-bandwidth product, offering flexible trade-offs between data rate and robustness [60, 62, 63]. The chirp-based structure distributes symbol energy across the entire bandwidth-time space, ensuring that even severe narrowband interference or frequency-selective fading affects only a portion of the transmitted energy. Experimental validations in bandwidth-constrained VLC systems have demonstrated BER improvements of up to two orders of magnitude compared to conventional FSK under equivalent channel conditions, establishing FSCM as a promising modulation technique for fortifying link robustness in adverse propagation environments.

phase-shift keying (PSK) modulates information by varying the phase of an electrical sinusoidal carrier whilst maintaining constant amplitude, providing inherent robustness against amplitude variations induced by turbulence-induced fading [51]. In M-ary PSK, M distinct phase states are uniformly distributed around the unit circle, enabling a spectral efficiency of $\log_2 M$ bit/s/Hz. The constant envelope property facilitates efficient operation of optical transmitters near saturation without concerns of nonlinear amplitude distortion, a significant advantage over amplitude-based modulation schemes. The time domain representation of the M-PSK electrical signal is written as [3]:

$$s_{\text{M-PSK}}(t) = p(t)\cos\left(2\pi f_c t + \frac{2\pi}{M}(m-1)\right) \tag{2.20}$$

where f_c is the frequency of the sinusoidal carrier, $p(t)$ is the pulse shaping function, and $m \in \{1, 2, \ldots, M\}$ represents the symbol index. M-PSK symbols can be represented in the in-phase and quadrature components of the carrier signal. The BER performance of the M-PSK modulation in an AWGN channel can be written as [3]:

$$BER_{\text{M-PSK}} = 2Q\left(\sqrt{\frac{2E_b}{N_0}}\sin\left(\frac{\pi}{M}\right)\right) \tag{2.21}$$

Figure 2.12 illustrates binary Phase Shift Keying (BPSK) modulation characteristics in both time and constellation domains, demonstrating the antipodal symbol placement that maximizes Euclidean distance for binary transmission. Figure 2.13 demonstrates the increased constellation density for QPSK, where the improvement in spectral efficiency comes at the cost of

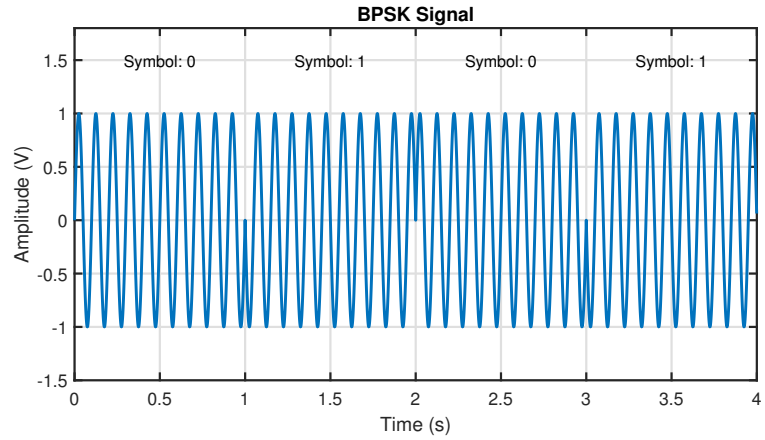

(a) *BPSK modulated signal in time domain*

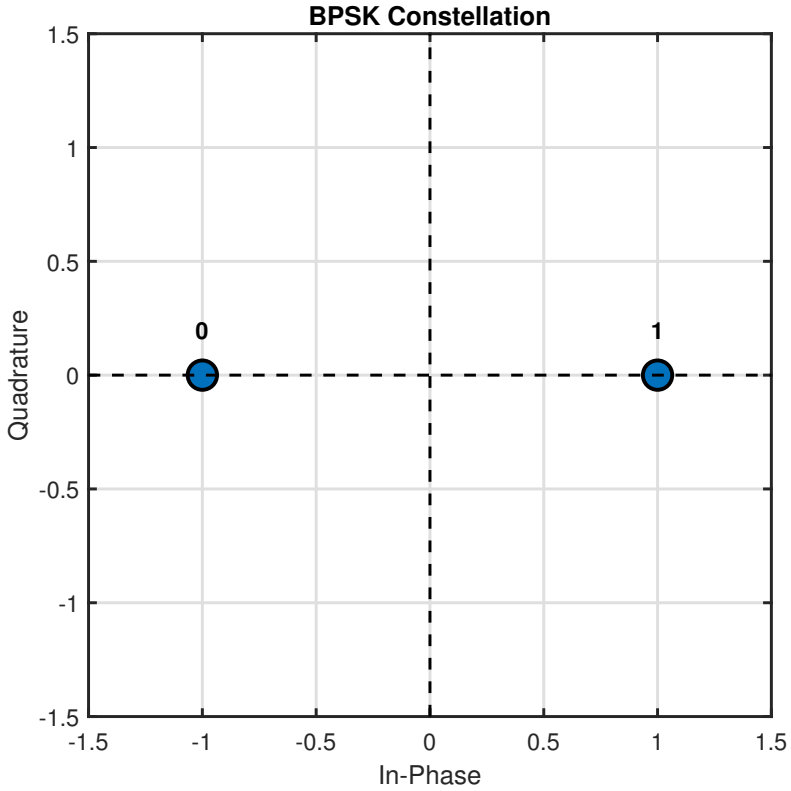

(b) *Constellation points of BPSK modulated signal*

Figure 2.12: *BPSK modulated signal*

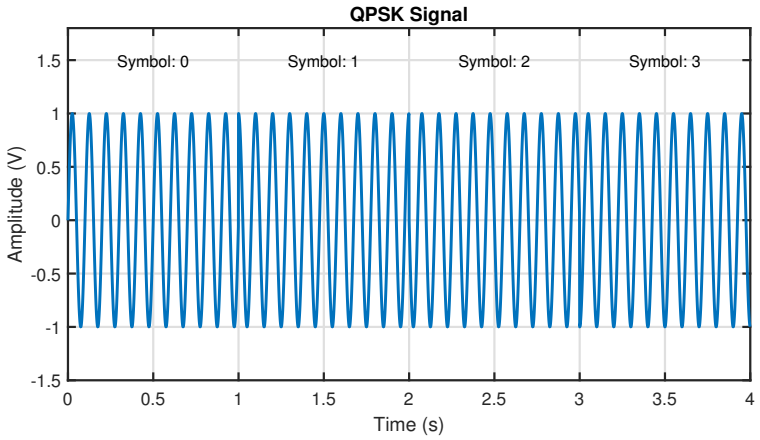

(a) *QPSK modulated signal in time domain*

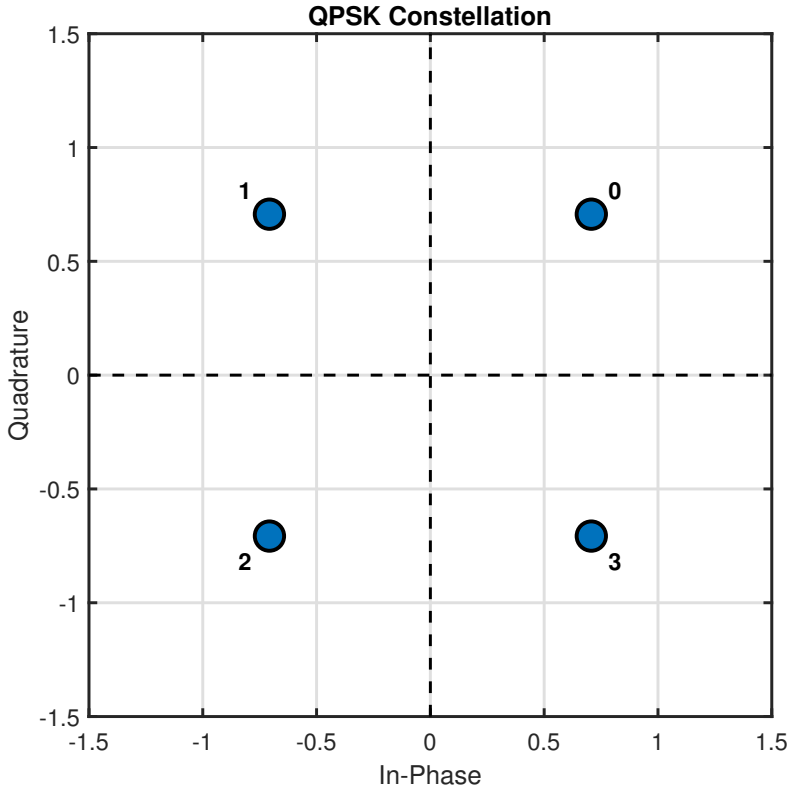

(b) *Constellation points of QPSK modulated signal*

Figure 2.13: *QPSK modulated signal*

reduced angular separation between constellation points, thereby increasing susceptibility to phase noise. Additionally, phase noise from laser sources and atmospheric turbulence-induced phase distortions can significantly degrade performance, particularly for higher-order modulations where inter-symbol angular distances reduced [64]. Despite these challenges, PSK remains popular in OWC systems requiring amplitude-fading resilience and spectral efficiency.

quadrature amplitude modulation (QAM) combines amplitude and phase modulation to achieve high spectral efficiency, representing one of the most bandwidth-efficient modulation schemes available for OWC systems. By modulating both the in-phase (I) and quadrature (Q) components of the carrier, QAM achieves superior spectral efficiency compared to PSK of equivalent order, as constellation points can be arranged in a two-dimensional rectangular grid rather than confined to a circle. This geometric advantage provides greater minimum Euclidean distance between symbols for a given average power, translating to improved BER performance relative to PSK at the same modulation order. The time-domain signal representation of the QAM modulated signal can be written as a function of its in-phase and quadrature components as [13]:

$$s(t) = A_c \sum_{n=-\infty}^{\infty} \left[I_n \cos(2\pi f_c t) - Q_n \sin(2\pi f_c t) \right] p(t - nT) \tag{2.22}$$

where A_c is the carrier amplitude, I_n is the amplitude of the in-phase component, Q_n is the amplitude of the quadrature component, f_c is the carrier frequency, $p(t)$ is the pulse shaping function, and T is the symbol period. The BER of a QAM modulated signal can be expressed as [51]:

$$BER_{\text{QAM}} = 1 - (1 - P_{e\sqrt{M_{\text{QAM}}}})^2, \tag{2.23}$$

where the symbol error probability is:

$$P_{e\sqrt{M_{\text{QAM}}}} = 2 \left(1 - \frac{1}{\sqrt{M_{\text{QAM}}}} \right) Q \left(\sqrt{\frac{3}{M_{\text{QAM}} - 1} \frac{E_b}{N_0}} \right), \tag{2.24}$$

Figure 2.14 illustrates the constellation structure of 16-QAM with one subcarrier modulated, demonstrating the rectangular grid arrangement that provides $\log_2 16 = 4$ bit/s/Hz spectral efficiency. The non-uniform Euclidean distances between constellation points result in non-

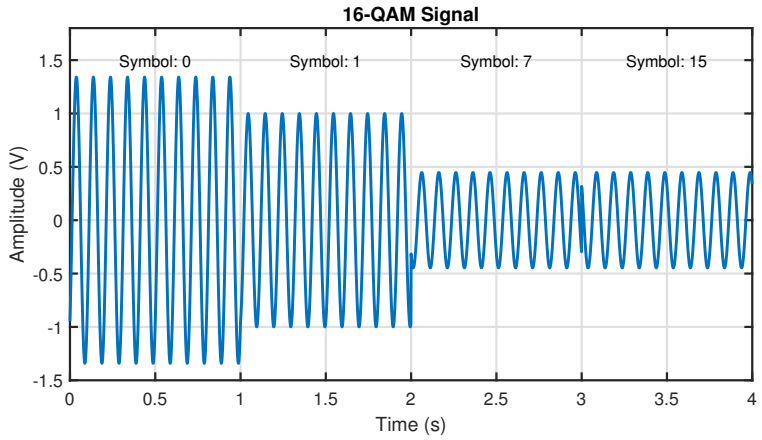

(a) *16-QAM modulated signal in time domain*

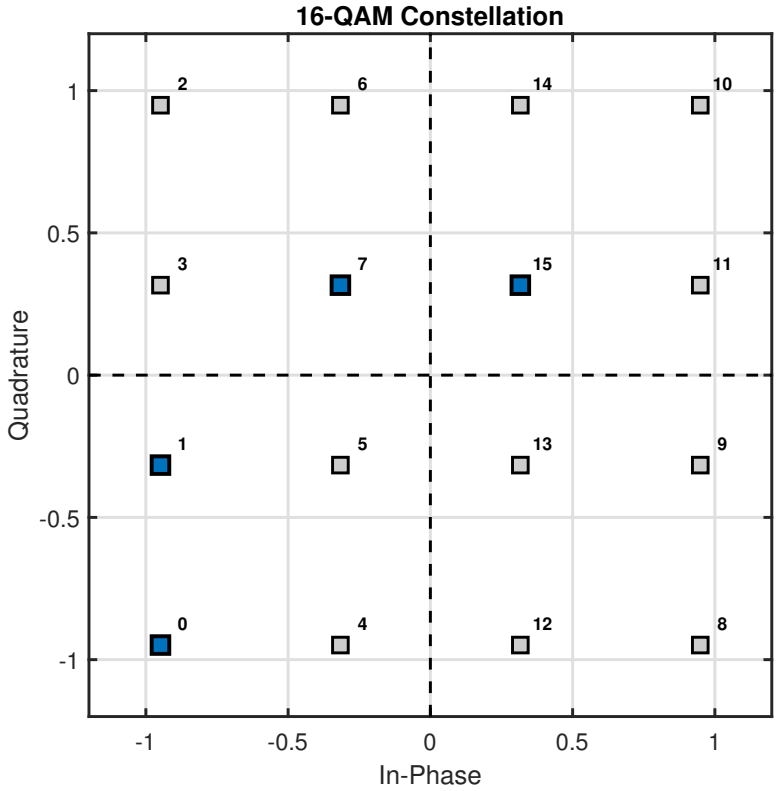

(b) *Constellation points of 16-QAM modulated signal*

Figure 2.14: *16-QAM modulated signal*

uniform error probabilities, with corner symbols exhibiting lower error rates than edge or interior symbols. QAM has been deployed in high-speed VLC systems, with demonstrations achieving multi-Gbps data rates through DC-biased optical orthogonal frequency division multiplexing (DCO-OFDM) implementations [13]. However, the dual encoding on both amplitude and phase renders QAM particularly vulnerable to both turbulence-induced fading and phase noise, representing a significant challenge for hostile channel environments. High-order QAM (64-QAM and above) requires relatively clear SNR conditions and typically necessitates adaptive modulation schemes that dynamically adjust modulation order based on instantaneous channel conditions. Furthermore, the high peak-to-average power ratio (PAPR) characteristic of QAM signals demands careful consideration of transmitter linearity to avoid nonlinear distortion effects that can cause constellation warping and inter-symbol interference.

The unique challenges of turbulent optical channels have motivated development of specialised modulation techniques that encode information in domains less susceptible to amplitude fluctuations. In OWC, SIM has emerged as particularly effective, encoding data in the frequency (FSK-SIM) or phase domain (PSK-SIM) rather than amplitude domain, thereby providing inherent resilience to turbulence-induced fading [6, 65]. Experimental demonstrations of FSK-SIM in turbulent underwater channels have achieved BER below 10^{-3} in conditions where conventional amplitude-based schemes experience error floors above 10^{-2} [66]. The combination of FSK with SIM exploits the differential resilience of frequency and amplitude to turbulence, with frequency and phase components maintaining stability even under scintillation conditions characterised by scintillation index values exceeding 0.45. In addition, when the data is encoded on the phase or frequency, channel state information (CSI) is not required at the receiver. When encoding data on the amplitude in addition to the phase, spectral efficiency of SIM may be further increased, while CSI is required for decoding as the optimal decoding threshold changes with varying fading. Thus, there is a trade-off in terms of the requirement of accurate CSI when decoding an amplitude modulated signal [65].

Recent advances have explored hierarchical modulation schemes that simultaneously exploit multiple signal dimensions to achieve enhanced robustness whilst maintaining high spectral efficiency. The three-dimensional hierarchical signalling technique, denoted as phase, amplitude and frequency-shift keying (PAFsk)-SIM, represents a significant innovation in this domain [67]. This approach leverages the differential resilience of frequency, phase, and amplitude to turbulence effects, implementing a hierarchical structure where FSK serves as the robust

base layer, with PSK and amplitude-shift keying (ASK) layers providing additional capacity when channel conditions permit. Experimental results demonstrate that PAFsk-SIM maintains reliable communication with the base FSK layer at SNR values 6 dB lower than required for full constellation recovery, enabling basic OWC communication link in deteriorating channel conditions [67]. Figure 2.15 (taken from [68]) gives an illustration of PAFsk-SIM waveform, with modulating 1 bit on frequency, 1 bit on phase, and 1 bit on amplitude, where the data is coded in all three dimensions.

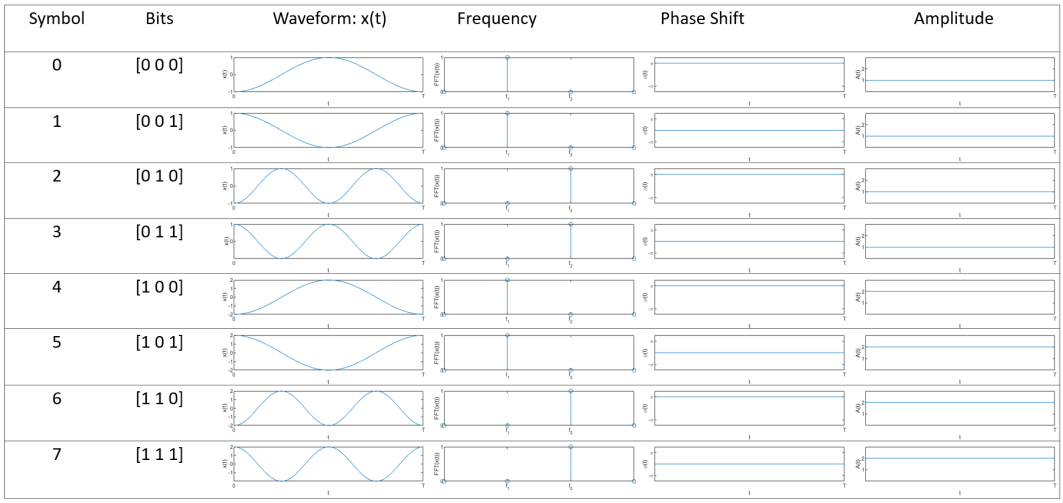

Figure 2.15: *An illustration of PAFsk-SIM bit mapping*

To compensate the poor spectral efficiency of frequency-based modulation schemes in OWC, PDM is introduced with an additional dimension for coherent light sources, effectively doubling system capacity without bandwidth expansion [69, 70]. Experimental demonstrations combining PDM with advanced modulation formats have achieved aggregate data rates exceeding 10 Gbps in turbulent underwater channels [71, 72]. However, PDM performance in turbulent conditions remains sensitive to polarisation-dependent loss and polarisation mode dispersion, with depolarisation effects causing up to 3 dB power penalty in strong turbulence and long distance [73].

To make the most use of the frequency resources of the channel frequency bandwidth, multiple subcarriers can be modulated to carry data. Orthogonal frequency division multiplexing (OFDM) with SIM and its variants adapted for IM/DD systems have been investigated for their inherent resilience to inter-symbol interference and ability to exploit frequency diversity [74]. Various OFDM adaptations including DC-biased optical (DCO)-OFDM, asymmetrically

clipped optical (ACO)-OFDM, and layered ACO-OFDM have been developed to address the constraints of optical intensity modulation [75]. Recent implementations incorporating adaptive bit and power loading have demonstrated spectral efficiencies approaching theoretical limits, with data rates exceeding 25 Gbps achieved in OWC systems through wavelength division multiplexing (WDM) combined with OFDM [71, 76].

Spatial mode multiplexing in fibre-coupled OWC systems provides an alternative dimension for capacity enhancement whilst maintaining resilience against misalignment. Recent theoretical frameworks demonstrate that zero-forcing beam forming in IM/DD systems can achieve over 200% capacity improvement through exploitation of orthogonal spatial modes, with experimental validation confirming robust performance under lateral displacements up to 2 mm [77, 78]. Few-mode fiber configurations maintain 150% capacity enhancement whilst tolerating angular misalignments exceeding 5 mrad without active tracking, offering practical advantages for indoor OWC deployments [78].

2.6 Summary

This chapter has established the fundamental theoretical foundations of optical wireless communication systems. The principles of intensity modulation with direct detection were presented, demonstrating how OWC systems encode information through optical intensity variations whilst maintaining the non-negativity constraint unique to optical signals. The analysis of optical sources and photodetectors revealed the performance trade-offs between different technologies, with LEDs providing cost-effective solutions for short-range applications and laser diodes enabling high-speed, long-distance communication.

The characterisation of channel effects in both atmospheric and underwater environments identified the primary impairments affecting OWC system performance. Atmospheric turbulence induces refractive index fluctuations causing beam spreading, wandering, and intensity scintillation, whilst molecular and aerosol interactions create wavelength-dependent attenuation. Underwater channels exhibit even more severe constraints, with strong absorption limiting transmission to the blue-green spectral window and turbulence from temperature and salinity variations causing significant signal degradation quantified through the scintillation index.

These fundamental principles and channel models provide the theoretical framework for understanding the performance limitations of OWC systems and motivate the development of robust

communication techniques capable of maintaining reliable operation in hostile propagation environments. The modulation schemes and multiplexing techniques introduced in Section 2.5 provide the signal-domain context for understanding the advanced robust techniques reviewed in Chapter 3.

Chapter 3
Literature Review on Robust Optical Wireless Communication Techniques

3.1 Introduction

Having established the fundamental principles and channel characteristics of OWC systems in Chapter 2, this chapter lists the state-of-the-art techniques developed to address the hostile channel effects that limit system performance. The challenge of maintaining reliable communication in the presence of turbulence-induced fading, atmospheric absorption, scattering, and dynamic misalignment has driven extensive research across multiple technical domains.

This chapter is going to introduce the existing approaches to robust OWC from two complementary strategies: intelligent signal processing techniques leveraging machine learning for channel estimation and equalisation, and system-level architectural innovations for adaptive system parameter management. Understanding the capabilities and limitations of these existing techniques is essential for identifying research gaps and establishing the context for the novel contributions of this thesis.

This chapter provides a comprehensive review of robust OWC techniques, evaluating their performance, implementation complexity, and practical deployment constraints. Section 3.2 describes the application of machine learning and deep learning for channel estimation, equalisation, and adaptive transmission. Section 3.3 reviews system-level approaches including beam tracking, adaptive modulation and coding, and reconfigurable architectures. Section 3.4 identifies the research gaps that motivate the contributions of this thesis. Section 3.5 summarises the key findings and their implications for robust OWC technology.

3.2 Machine Learning-Based Techniques

Alongside the modulation schemes introduced in Section 2.5, the application of machine learning (ML) and deep learning (DL) techniques to OWC systems represents a complementary

approach for addressing non-linear channel impairments and enabling adaptive system optimisation. These data-driven approaches offer powerful tools for channel estimation, equalisation, and resource allocation that surpass the capabilities of traditional signal processing methods.

Neural network-based equalisers have demonstrated better performance compared to conventional linear equalisers in compensating for the complex non-linearities present in OWC channels. Gaussian kernel-based deep neural network (GK-DNN) achieve up to 3 dB improvement in receiver sensitivity for PAM-based VLC systems, effectively mitigating the combined effects of LED nonlinearity, bandwidth limitations, and multipath dispersion [79]. The GK-DNN architecture exploits the universal approximation capabilities of neural networks whilst incorporating domain knowledge through Gaussian kernel preprocessing, reducing training complexity by approximately 40% compared to conventional deep neural networks [80].

Long short term memory (LSTM) networks have proven particularly effective in tracking time-varying channel impairments by exploiting temporal correlations in the received signal [81,82]. LSTM-based equalisers demonstrate robust performance in dynamic scenarios where conventional adaptive filters fail to converge, achieving BER improvements of up to one order of magnitude in mobile VLC applications. The recurrent architecture of LSTM networks enables them to maintain CSI across symbol periods, effectively compensating for slowly varying turbulence effects with coherence times exceeding the symbol duration.

Cluster algorithm of perception decisions (CAPD), enable non-linear decision boundary optimisation in the presence of signal-dependent noise characteristic of OWC systems [83, 84]. CAPD dynamically adjusts detection thresholds based on received signal statistics, providing up to 2 dB sensitivity improvement compared to fixed threshold detection in scenarios with ambient light interference. The integration of fuzzy logic with clustering approaches further enhances robustness to uncertainty in channel state estimation.

Joint maximum likelihood detection (JMLD) enhanced with neural network preprocessing has proven effective for suppressing backscattering self-interference in full-duplex UOWC systems [85]. The neural network component learns the statistical characteristics of interference patterns, enabling near-optimal detection with computational complexity reduced by a factor of 10^3 compared to exhaustive search methods. This hybrid approach maintains performance within 0.5 dB of optimal JMLD whilst enabling real-time implementation on embedded processors.

Deep reinforcement learning (DRL) algorithms have revolutionised adaptive transmission strategies in OWC systems by learning optimal policies through interaction with the channel environment [86, 87]. DRL agents trained using proximal policy optimisation achieve near-optimal power allocation and modulation selection decisions, adapting to time-varying channel conditions without requiring explicit channel models. Experimental demonstrations show that DRL-based adaptation improves system throughput by up to 30% compared to fixed transmission strategies whilst maintaining target BER constraints.

The application of convolutional neural network (CNN)s to image-based channel estimation exploits the spatial information captured by camera receivers to extract CSI with minimal computational overhead [88, 89]. CNN architectures specifically designed for OWC applications achieve channel estimation accuracy comparable to pilot-based methods whilst reducing overhead by up to 50%. Transfer learning techniques enable pre-trained networks to adapt to new channel conditions with minimal additional training, facilitating deployment across diverse environments.

Machine learning classification algorithms are also considered in OWC [80]. Two widely used are support Vector Machines (SVM) and K-Nearest Neighbours (K-NN). These two methods were selected for their complementary strengths in pattern recognition and classification tasks. Support Vector Machines operate by identifying optimal hyperplanes that maximise the separation between different classes in feature space [90]. The fundamental principle of the algorithm involves maximising the margin between support vectors of the nearest data points from distinct classes, thereby enhancing the model's generalisation capabilities for collected data. For scenarios involving non-linearly separable data, SVM implements kernel transformations to project the data into higher-dimensional spaces where linear separation becomes feasible.

K-Nearest Neighbours represents a non-parametric classification and regression methodology [91]. This algorithm demonstrates particularly robust performance when applied to well-structured, low-dimensional datasets. However, its efficiency diminishes significantly when processing large-scale or high-dimensional data structures. The algorithm's effectiveness is heavily dependent on two critical parameters: the selection of an appropriate k value and the choice of distance metric, both of which should be optimised for the specific application context.

Adaptive optical switching architectures employing machine learning for resource allocation have achieved sub-microsecond latency in data center networks, demonstrating 55% latency

reduction and 95% packet loss improvement through intelligent wavelength assignment [92]. Reconfigurable implementations with real-time traffic monitoring achieve additional 37% latency improvement, providing frameworks applicable to cognitive OWC systems [93].

Graph neural networks applied to multiple-input multiple-output (MIMO)-OWC systems enable efficient spatial multiplexing and interference management in dense deployment scenarios [94]. These approaches model the interference relationships between spatial streams as graph structures, achieving near-optimal performance with polynomial complexity scaling compared to exponential complexity of exhaustive search methods. The graph-based representation naturally captures the spatial correlation structure of MIMO channels, enabling effective generalisation to different antenna configurations.

The current learning method related research directions include development of physics-informed neural networks incorporating domain knowledge to improve generalisation and reduce training requirements. Integration of quantum communication principles with classical OWC offers potential for unconditional security and enhanced capacity [95], which requires more attention. In addition, application of terahertz frequencies for ultra-high-speed short-range optical wireless links represents a frontier area with significant potential for next-generation systems, and [96].

3.3 Robust System Design for Optical Wireless Communication

Beyond modulation and signal processing techniques, system-level approaches to robustness encompass architectural innovations and adaptive mechanisms that enhance OWC performance through intelligent resource management and environmental awareness. These techniques address the dynamic nature of OWC channels and challenges beyond the scope of physical layer solutions alone [2].

3.3.1 Beam Alignment and Tracking

Dynamic beam alignment represents a fundamental challenge in mobile OWC systems, particularly for narrow-beam laser communications where even small angular misalignments can cause complete link failure. Camera-based tracking systems utilising infrared LED markers demonstrate sub-millisecond response times, though processing latency remains limiting for

high-mobility scenarios [97]. Advanced implementations incorporate predictive algorithms that anticipate platform motion, reducing tracking error by up to 70% compared to reactive approaches [98].

Time difference of arrival (TDOA) algorithms provide enhanced tracking accuracy through triangulation, with simulation results confirming link availability improvements exceeding 20% in vehicular OWC applications [99]. The integration of TDOA with inertial measurement units enables robust tracking even during temporary signal blockages, maintaining alignment within 0.5 mrad for platform velocities up to 10 m/s.

Fiber-coupled receivers exploiting modal diversity provide passive misalignment tolerance through automatic mode selection, maintaining coupling efficiency variations below 3 dB for platform vibrations up to 100 Hz [78]. This approach reduces mechanical tracking requirements for indoor applications whilst achieving comparable robustness to active alignment systems.

Closed-loop tracking systems incorporating silicon photodetector arrays and adaptive optics eliminate mechanical components, achieving tracking rates up to 1 kHz with power consumption below 100 mW [100]. Liquid crystal spatial light modulators provide electronic beam steering with response times below 10 ms, though limited steering ranges of $\pm 5°$restrict their application to fine tracking adjustments [101].

Microelectromechanical systems (MEMS) mirrors offer wider steering ranges exceeding ±30°, though beam splitting requirements for feedback control inherently reduce received power by at least 50% [102]. The work utilising dual-mirror configurations separate tracking and communication functions, maintaining full optical power for data transmission whilst dedicating a low-power beacon for alignment. Furthermore, when combining with deep learning and machine learning, image-based tracking and MEMS-mirror configuration can extract beam position information from severely distorted optical channel [103, 104].

3.3.2 Channel State Information Estimation

CSI estimation techniques enable simultaneous channel monitoring and data transmission without dedicated pilot symbols or feedback channels [105]. OFDM-based CSI acquisition methods achieve accurate channel characterisation whilst maintaining gigabit-per-second communication rates, exploiting existing signal structures for channel measurement without additional overhead [106].

Camera-based CSI estimation systems leverage backscattered photons for real-time channel monitoring, eliminating feedback requirements in half-duplex systems [88, 89]. Computer vision algorithms extract environmental parameters including visibility, turbulence strength, and obstacle locations, enabling proactive link adaptation. However, computational requirements for real-time image processing currently limit update rates to approximately 10 Hz for embedded implementations [107].

3.3.3 Adaptive Modulation and Power Control

Adaptive modulation and coding (AMC) schemes dynamically adjust transmission parameters based on instantaneous channel conditions, maximising throughput whilst maintaining reliability constraints [108]. Rate adaptive systems employing probabilistic constellation shaping achieve capacity gains of up to 1.5 bits/symbol compared to uniform signalling, approaching Shannon limits within 0.5 dB at high SNR [109–111].

Power efficient adaptive strategies jointly optimise modulation format and transmit power for energy constrained applications, demonstrating particular relevance for solar powered UOWC nodes [112]. Machine learning-based prediction of channel evolution enables proactive adaptation, reducing feedback latency by up to 80% whilst maintaining near optimal performance [87].

3.3.4 Reconfigurable Intelligent Surfaces

Reconfigurable intelligent surfaces (RIS) represent an emerging paradigm offering unprecedented control over optical propagation environments through programmable phase modulation [113, 114]. Initial studies demonstrate potential SNR improvements exceeding 10 dB through intelligent beam focusing and interference nulling. Meta surface implementations provide sub-wavelength control enabling functionalities including beam steering, orbital angular momentum generation, and polarisation manipulation [115]. However, practical deployment faces challenges including limited modulation depth, wavelength dependence, and control complexity for large scale surfaces.

3.4 Research Gap and Goals

Despite significant advances in robust OWC techniques, critical research gaps persist that limit practical deployment and motivate the contributions of this thesis.

The majority of existing studies consider simulated channel models that fail to capture complex spatio temporal dynamics of real world optical channels, particularly combined effects of turbulence, scattering, and platform motion [116]. Experimental development with real-world channel models incorporating all time-varying relevant impairment factors still need more investigation, requiring more practical, accurate performance prediction and system optimisation. Furthermore, systematic comparative studies of modulation schemes under realistic and diverse channel conditions are notably limited [117], with the absence of standardised evaluation methodologies complicating technology selection for specific applications.

The computational complexity of advanced signal processing techniques, particularly ML-based approaches, poses significant implementation challenges on resource-constrained platforms [79]. Quantitative analyses of the trade-off between performance improvement and computational overhead remain largely unexplored, impeding practical deployment decisions. Additionally, the integration of multiple robust techniques into cohesive system designs has received limited attention, with most studies showing individual components in isolation rather than exploring potential joint corporation.

Real-time implementation constraints, including processing latency, power consumption, and hardware complexity, are frequently overlooked in theoretical studies. The gap between laboratory demonstrations and field deployable systems remains substantial, with environmental factors such as bio fouling in UOWC and ambient light variations in VLC inadequately addressed [118]. The specific gaps addressed in this thesis and the chapters in which they are resolved are summarised in Table 3.1.

Research Gap	**Addressed in**
Lack of experimental validation of frequency-based modulation with PDM under realistic UOWC turbulence and turbidity conditions	Chapter 4
Limited experimentally validated real-time beam tracking systems for OWC	Chapter 5
Absence of feedback-free CSI estimation enabling adaptive transmission in OWC	Chapters 6 and 7
Gap between laboratory demonstrations and practically deployable system designs	Chapters 5, 6, and 7

Table 3.1: *Research gaps and corresponding thesis chapters.*

The first gap is addressed in Chapter 4 through systematic BER measurements of FSK-SIM and FSCM with PDM across multiple channel conditions, including still water, temperature-induced turbulence, bubble-induced turbulence, and three levels of Jerlov turbidity, using a controlled laboratory UOWC channel emulator. The second gap is addressed in Chapter 5 through a fully built and experimentally tested photodetector-array-based fine tracking system with closed-loop beam steering, validated under both static and dynamic misalignment conditions. The third gap is addressed in Chapter 6 via a camera-based CSI estimation approach, where machine learning extracts channel state from captured beam images without any return channel, and in Chapter 7 via a retroreflector-based approach, where a portion of the transmitted beam is passively returned to the transmitter side for polarisation-based CSI estimation, again requiring no dedicated feedback path. The fourth gap is addressed across Chapters 5, 6, and 7, all of which demonstrate their respective systems in real hardware operating on live optical signals under realistic channel conditions rather than relying on simulation alone.

3.5 Summary

This chapter has presented a comprehensive review of robust techniques for optical wireless communication systems, examining advances in modulation schemes, machine learning applications, and system design strategies. The literature review demonstrate that frequency-based and hierarchical modulation schemes provide resilience to channel impairments, machine learn-

ing enables adaptive system behaviour surpassing traditional methods, and system-level innovations address challenges beyond physical layer and offer the potential joint corporation technology.

The identified research gaps, such as particularly the lack of experimental work in varying OWC channel, limited comparative studies in real OWC channel, and the gap between laboratory demonstrations and field deployments, provide motivation for the contributions presented in subsequent chapters in the thesis, as well as emphasise the importance of the robust OWC technology towards practical deployment in challenging environments.

Chapter 4

Empirical Study of Frequency-Based Signalling with Polarisation Division Multiplexing

4.1 Introduction

As established in Section 2.4, turbulence-induced amplitude fading is the primary impairment limiting reliability in UOWC systems, and Chapter 3 identified frequency-based modulation as a promising solution because encoding information on frequency rather than amplitude provides inherent immunity to such fluctuations [53, 66]. PDM is incorporated alongside these schemes to recover the spectral efficiency that frequency-based formats inherently trade away [70].

This chapter presents an empirical investigation and comparison of frequency-based modulation schemes combined with PDM in different UOWC channel conditions to address the dual challenges of channel resilience and spectral efficiency in UOWC systems. The key contribution of this chapter is the systematic empirical investigation of FSK-SIM and FSCM combined with PDM across multiple UOWC channel impairments, including still water, temperature-induced turbulence, bubble-induced turbulence, and turbidity, providing a quantitative comparison of these techniques and demonstrating that PDM can approximately double throughput while the resilience of frequency-based modulation is preserved.

The chapter is organised as follows: Section 4.2 introduces the frequency-based modulation techniques; Section 4.3 describes PDM principles and implementation; Section 4.4 details the experimental setup and channel evaluation; Section 4.5 presents the experimental results comparing FSK and FSCM with and without PDM; and Section 4.6 summarises the chapter findings.

4.2 Frequency-based Modulation Techniques in OWC

4.2.1 Frequency-shift Keying with Subcarrier Intensity Modulation

For the SIM considered, $m(t)$ from (2.1) with N subcarriers is given as:

$$m(t) = \sum_{i=1}^{N} A_i \cos(\omega_i t + \phi_i), \tag{4.1}$$

where A_i, ω_i and ϕ_i denote the i^{th} subcarrier signal's amplitude, frequency and phase respectively. When the signal propagates through a channel that is affected by turbulence, A_i is affected directly but ω_i and ϕ_i are not. Thus, data that is encoded on the phase or frequency of the subcarrier signal is shielded from the effect of turbulence induced fading [6, 66]. In order to implement FSK using SIM, data is encoded upon ω_i. Here, data carrying subcarriers are defined and symbols are mapped to these whilst A_i and ϕ_i are kept constant. When the signal propagates through a channel that is affected by turbulence induced fading, A_i will vary but ω_i and ϕ_i will not. This inherent resilience is exploited by encoding data on the frequency (and/or phase) of the subcarrier signal.

4.2.2 Frequency Shift Chirp Modulation

As introduced in Chapter 3, FSCM encodes each symbol as a cyclically frequency-shifted chirp waveform that spans the full modulation bandwidth [60]. Its continuous-time domain waveform can be represented by [60]:

$$x_m(t) = \cos\left(2\pi \int_0^t f_m(\tau)\, \mathrm{d}\tau\right). \tag{4.2}$$

Here, $f_m(t)$ denotes the frequency of the chirp signal which is evaluated from the basic chirp frequency, $f_0(t) = \mu t$ where $\mu = B/T_\mathrm{s}$ is the chirp rate. When the shifted frequency reaches the highest frequency within the symbol duration, it wraps down and starts from 0 Hz, this is realised by applying the *modulo* operator as [60]:

$$f_m(t) = \mathrm{mod}\left(\frac{m}{T_\mathrm{s}} + f_0(t),\ B\right). \tag{4.3}$$

Figure 4.1 illustrates the FSCM principle for representative symbols $m \in \{0, 1, 12, 33, 63\}$ with modulation parameters $M = 64$ and $B = 100$ kHz, adapted from [53]. The frequency-

time characteristics depicted in Fig. 4.1(a) and corresponding time-domain waveforms in Fig. 4.1(b) demonstrate the cyclic frequency shifting mechanism that distinguishes each symbol.

The fundamental chirp representing symbol $m = 0$ exhibits linear frequency variation from 0 Hz to the maximum bandwidth of 100 kHz over the symbol duration. Symbol $m = 1$ introduces a frequency offset of $1/T_s$, causing the instantaneous frequency to reach the bandwidth limit B before the symbol period expires, at which point the modulo operation wraps the frequency to 0 Hz and continues the linear sweep. This frequency wrapping behaviour becomes increasingly pronounced for higher-order symbols. For symbol $m = 12$, the initial frequency offset causes an earlier wrap point, whilst $m = 33$ demonstrates even more rapid frequency cycling within the symbol duration.

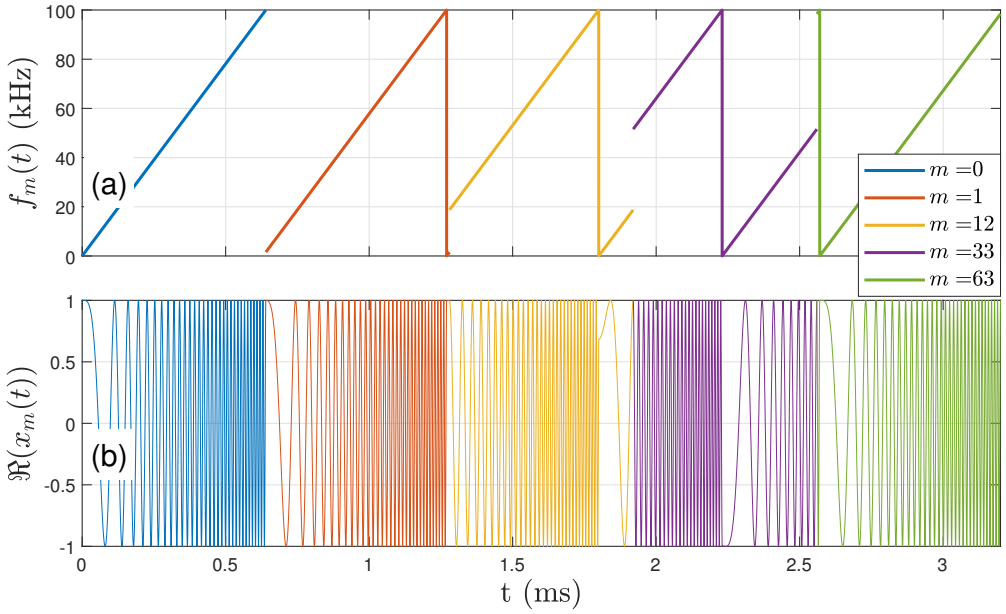

Figure 4.1: *An illustration of FSCM, M=64, B=100 kHz*

The case occurs with symbol $m = 63$, representing the highest symbol value in this 64-FSCM scheme. The initial frequency $63/T_s$ approaches the bandwidth limit B, resulting in almost immediate wrapping to 0 Hz followed by a linear frequency sweep occupying the majority of the symbol period. This progressive variation in frequency wrapping behaviour across different symbol values provides the orthogonality required for reliable symbol discrimination at the receiver.

4.2.3 Comparison between FSK and FSCM

In the SIM with FSK scheme, data is encoded onto the frequency of a subcarrier. Here, each symbol is made up of $N = M$ subcarriers, where M is the modulation order, with the frequency of the active subcarrier representing the data to be transmitted during a symbol duration. For the SIM with FSCM on the other hand, a data symbol is represented by a frequency chirp signal that occupies the entire modulation bandwidth. That is, data is encoded on a sweep of frequencies, rather than just one subcarrier [60]. The symbol structure of FSCM has potential advantages over FSK that can make it more resilient to hostile channel effects in UOWC. The power efficiency of both FSCM and FSK has been compared for terrestrial optical wireless communication (OWC), showing that the symbol structure of FSCM is more efficient and results in a lower signal-to-noise ratio (SNR) requirement than FSK [53].

Additionally, the unique advantage of SIM-chirp signaling arises from the symbol energy not being concentrated in a single frequency of the subcarrier signal but spread across a progressively increasing range of frequencies within the symbol duration. As a result, the entire energy of a data symbol is 'shielded' from severe attenuation suffered by any single signal frequency. Thus, 'spreading' the symbol energy over a range of subcarrier signal frequencies with chirp signalling offers resilience to the combined effects of the channel and limitation of the front-end devices. However, the spectral efficiency of frequency-based modulation is poor, thus, PDM is considered to be combined in this chapter.

4.3 Polarisation State along UOWC Link and Polarisation Division Multiplexing

The polarisation state evolution of optical signals propagating through atmospheric and underwater channels, and their interaction with optical elements, can be rigorously described using Jones calculus formalism. For a fully polarised monochromatic light beam, the electric field vector is represented in the Jones formalism as [119]:

$$\vec{E} = \begin{pmatrix} E_x \\ E_y \end{pmatrix} = \begin{pmatrix} |E_x|e^{j\phi_x} \\ |E_y|e^{j\phi_y} \end{pmatrix} \tag{4.4}$$

where E_x and E_y denote the complex amplitudes of the orthogonal electric field components, with $|E_x|$ and $|E_y|$ representing the field magnitudes, and ϕ_x and ϕ_y the respective phase components.

For partially polarised beams encountered in practical systems, the degree of polarisation (DoP) provides a quantitative metric of polarisation purity, calculated as [70]:

$$\text{DoP} = \frac{|V_{pp}^{y} - V_{pp}^{x}|}{V_{pp}^{y} + V_{pp}^{x}} \times 100\% \tag{4.5}$$

where V_{pp}^{x} and V_{pp}^{y} represent the measured peak-to-peak voltages corresponding to the orthogonal polarisation components. Over short distance links, experimental and analytical studies have demonstrated that polarisation states are broadly maintained over 10's of metres in underwater channels. The effect of turbulence on polarisation has been studied analytically [120, 121], with results indicating that polarisation properties are maintained in turbulent conditions. The effect of turbidity on polarisation has been investigated empirically [122], showing that polarisation state is preserved under single scattering conditions. The preservation of polarisation is attributed to small-angle scattering, where angles less than 10° result in negligible polarisation changes [123]. Thus, the maintaining polarisation state allows PDM to be used with UOWC.

Since the data rates achievable with frequency-based modulation are limited by their inherently low spectral efficiency, PDM is applied to compensate for this whilst maintaining the resilience to the effects of turbulence. PDM allows the use of the polarisation properties of light to transmit two orthogonal data streams within the same channel, effectively doubling the spectral efficiency compared to single polarisation systems [70, 71, 124, 125]. In addition, coherent polarisation-shift keying (PolSK) has been used to exploit polarisation properties for improved performance under turbulence [126].

In PDM systems, the transmitted optical signal can be represented as [70]:

$$P_t(t) = \exp\{j(\omega t + \phi)\} \left[\sqrt{P_t^{x}(t)} \cdot \hat{x} + \sqrt{P_t^{y}(t)} \cdot \hat{y} \right] \tag{4.6}$$

where the exponential term describes the optical carrier with angular frequency $\omega = 2\pi c/\lambda$, $P_t^{x}(t)$ and $P_t^{y}(t)$ represent the optical power of each polarisation state carrying independent data streams which align with (2.1), and $\hat{x}$, $\hat{y}$ denote the orthogonal polarisation unit vectors.

4.4 Experimental Evaluation

4.4.1 Experimental Setup

The experimental investigation was conducted using the setup illustrated in the block diagram in Fig. 4.2 and the demonstrating photo is shown in Fig. 4.3. Data streams for two orthogonal polarisation states were generated in MATLAB, employing frequency-shift keying with subcarrier intensity modulation (FSK-SIM), and then loaded onto a Keysight M8195A arbitrary waveform generator (AWG) for parallel transmission; the AWG was chosen for its dual-channel output with precise inter-channel synchronisation, which is essential for generating two independent PDM streams at the required symbol rates simultaneously. A direct current (DC) bias, I_{bias}, was combined with each signal via a bias-T to ensure positive, unipolar operation. These signals modulated two identical, orthogonally polarised Osram PL450b laser diodes (LDs). Laser diodes were preferred over LEDs because their coherent emission and modulation bandwidth exceeding 1 GHz are necessary to support the high symbol rates under investigation, while the 450 nm wavelength was selected because it falls within the blue-green transmission window of seawater (450–550 nm) where optical absorption is minimised [5]. The laser diodes are tuned to transmit s- and p-polarised beams with a DoP of 80%. The resulting optical signals were collimated and combined into a single beam using a Thorlabs PBS251/M, configured as a polarising beam combiner (PBC); this component was chosen for its high polarisation extinction ratio at 450 nm, which is critical for PDM operation as it ensures clean beam combination and suppresses inter-channel crosstalk before transmission through the underwater channel emulator (UCE).

At the receiver, a second Thorlabs PBS251/M, operating as a polarising beam splitter (PBS), separated the two polarisation states; the same high extinction ratio that makes it suitable at the transmitter also ensures low inter-polarisation interference at the detection stage. Each signal was then converted back into the electrical domain by an identical Femto HSPR-X-I-1G4-SI photodetector (PD), selected because its silicon responsivity at 450 nm and -3 dB bandwidth of approximately 900 MHz are well matched to the transmitted wavelength and are sufficient to resolve all symbol rates evaluated in this chapter. The analogue outputs were sampled by an Agilent DSA90804A oscilloscope, which was chosen for its high sampling rate and large memory depth that together allow 2000 consecutive transmission bursts per channel condition to be captured in a single acquisition, providing the statistical volume required for reliable BER estimation, and subsequently processed offline in MATLAB.

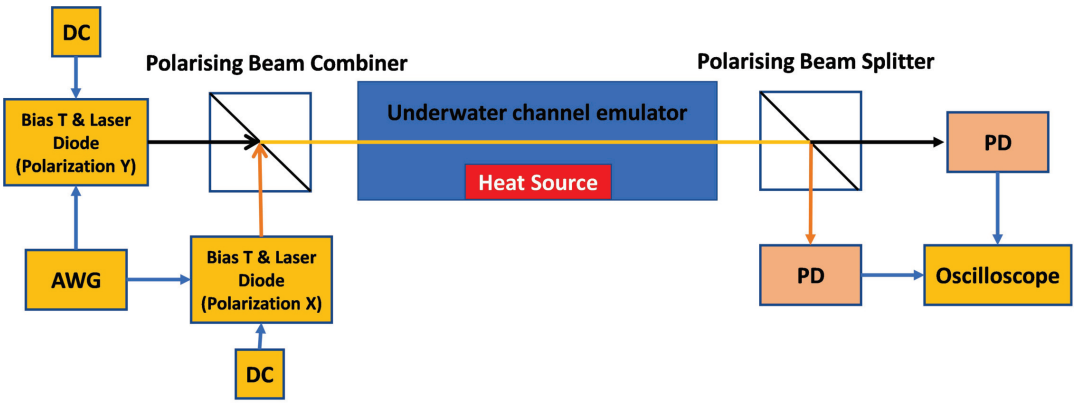

Figure 4.2: *The system block diagram of the experimental setup used in this investigation, including the laser diode (LD), arbitrary waveform generator (AWG), direct current (DC) source, and photodiode (PD).*

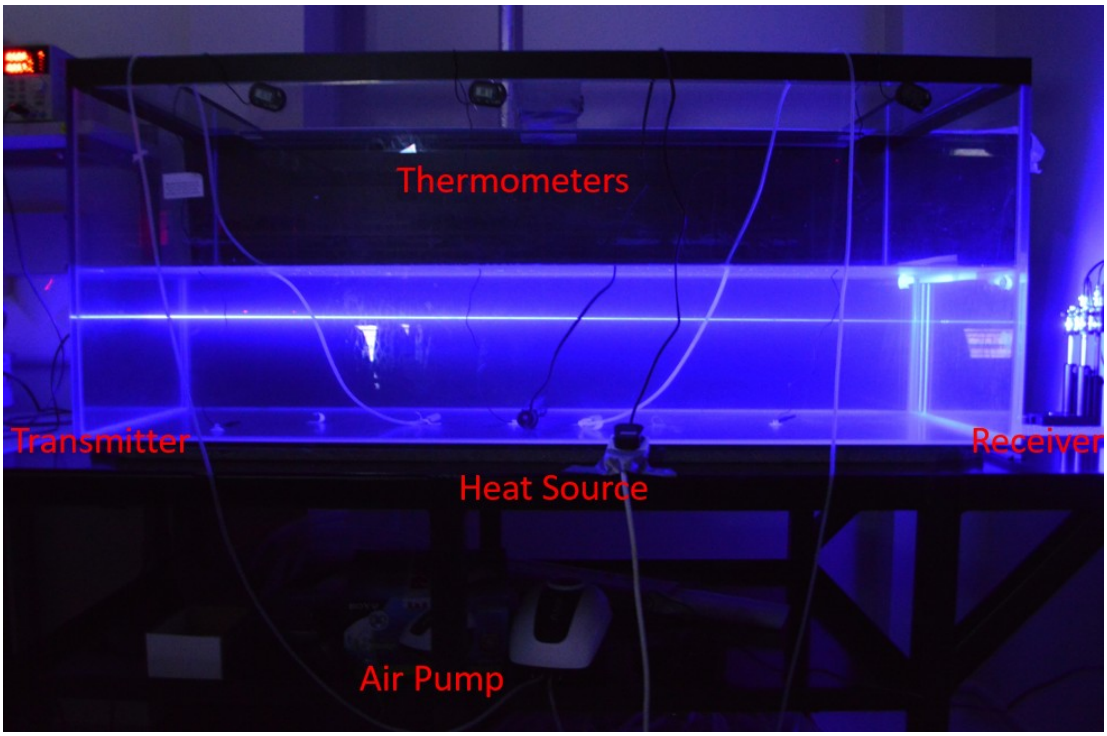

Figure 4.3: *The image for demonstrating the experimental setup.*

The UCE comprises a $1.5 \times 0.5 \times 0.5$ m^3 tank, which allows for the control of water conditions. For this study, the UCE was filled with 210 L of clear tap water. Turbulence was generated by inducing a temperature inhomogeneity along the propagation path using an aquarium heater positioned along the optical beam propagation path in the water tank. When activated, the heater emanates a thin layer of hot water, creating a thermal boundary with the cooler surrounding water. This temperature gradient induces turbulence within the channel. The orientation of the heating element relative to the optical beam determines the scattering characteristics: when parallel to the beam, photons traverse the fluctuating boundary layer multiple times, experiencing repeated scattering events; conversely, when perpendicular, photons undergo the lensing effect only once. This configuration allows control over the turbulence-induced scattering per link while maintaining a fixed transmission length [127]. The degree of turbulence in the channel is quantified by the scintillation index σ_I^2, defined in (2.10), which is computed from the 2000 received intensity samples collected at each experimental condition. To achieve a target σ_I^2 value, the heater power and its lateral distance from the optical beam axis were adjusted incrementally: positioning the heater closer to the beam and increasing its power raises the thermal gradient and in turn increases σ_I^2, while moving it further away reduces the turbulence strength. After each adjustment, a preliminary set of intensity measurements was taken and σ_I^2 was computed until the measured value stabilised within the desired range. For bubble-induced turbulence, the air pump flow rate was controlled via a flow divider valve; increasing the flow rate raises the bubble density in the beam path and increases σ_I^2 accordingly, providing repeatable and discrete turbulence strength settings. In this chapter, to account for the random nature of the turbulent and turbid channel and obtain representative BER results, data is transmitted over 2000 iterations, each containing packets of 400 random data bits.

To simulate turbid water conditions, different amount of antacid tablets were smashed and dissolved in the tap water to control the turbidity. The extinction coefficients for these conditions were previously measured in [42] and are shown in Fig. 4.4. To ensure the experimental conditions are relevant to real-world scenarios, the turbidity levels were chosen to approximate specific Jerlov water types, as classified in [128, 129]. The corresponding parameters are detailed in Table 4.1.

The statistical distribution of the received optical intensity depends on the physical mechanism driving the channel fluctuations. In still water, where turbulence is absent, the dominant contribution to intensity variation is receiver thermal noise and shot noise, both of which are

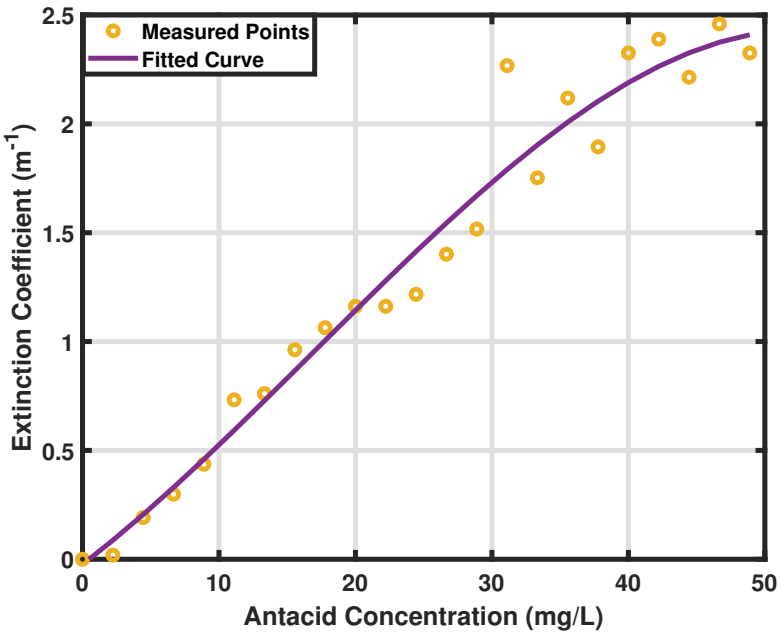

Figure 4.4: *Estimated channel extinction coefficients plotted against antacid concentration.*

Turbid Level	**Antacid Conc. (mg/L)**	$c(\lambda)$ **(m^{-1})**	**Approx. Jerlov Water Type [128]**
Turbid 1	4.76	0.2	Jerlov IB (clear open ocean)
Turbid 2	16.7	0.8	Jerlov 3C (coastal ocean)
Turbid 3	28.6	1.5	Jerlov 5C (harbour water)

Table 4.1: *Turbid water parameters considered in the experiments.*

well modelled by a Gaussian distribution. For temperature-induced turbulence, refractive index fluctuations arise from thermal gradients along the propagation path. Under weak-to-moderate turbulence conditions, Rytov perturbation theory predicts that the log-irradiance follows a normal distribution, which leads to the Generalised Gamma distribution as an appropriate model for the received intensity [130]. For bubble-induced turbulence, the channel impairment is fundamentally different in nature: random bubble passages through the beam produce discrete, deep-fading events that are exponentially distributed, superimposed on the log-normal background fluctuations present in all turbulent water. This combination of two independent fading mechanisms gives rise to the Exponential Log-Normal distribution as the theoretical model [131]. These theoretical distributions are used to fit the empirical received intensity data, and the quality of fit is assessed through the coefficient of determination R^2.

To demonstrate the differences among the three water conditions, the received intensity distributions and measured SI in both still and turbulent water are depicted in Figure 4.5. As expected, the received signal in still water conforms to a Gaussian distribution as illustrated in Figure 4.5a. On the other hand, the distribution in turbulence induced by temperature inhomogeneity fits a generalized Gamma distribution, as proposed in [130]. For bubble-induced turbulence, the received signal fits an exponential log-normal distribution, as proposed in [131]. The SI of the fitted distributions, σ^2_{fit}, and the corresponding coefficient of determination, R^2, are presented in Table 4.2, with the R^2 metric of fit being greater than 0.9, which indicates that they provide a good description of the data. Additionally, the Gaussian shape in still water is centred around a mean of 1, indicating that the shape is dominated by noise in the system. When temperature-induced turbulence is present, the shape of the generalised Gamma distribution skews to the right, but the tail is fairly long towards 0, which means the channel varies significantly within the range. This fading affects the received signal, leading to a severe degradation of the UOWC link. As for the bubble-induced turbulence, the exponential log-normal shape exhibits components around 0.1 and a primary peak centered around 1.15. This suggests that a bubble causes a deep fading event. This can be attributed to the fact that the bubble size is much larger than the wavelength of the laser light, so the light beam is refracted rather than scattered. As such, when the signal reaches the receiver after refraction, the dynamic range of the received signal is smaller compared to the case of temperature-inhomogeneity-induced turbulence.

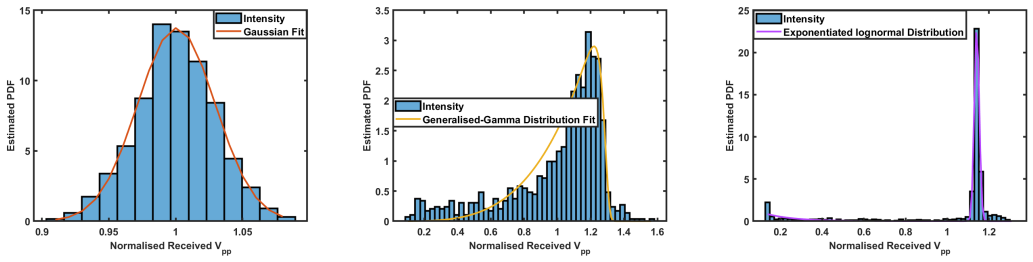

(a) Still water, $\sigma_I^2 \approx 0$

(b) Temperature turbulent water, $\sigma_I^2 \approx 0.10$, $\Delta T \approx 6$ K

(c) Bubble turbulent water, $\sigma_I^2 \approx 0.10$, $FR \approx 1.88$ L/min

Figure 4.5: *Histogram showing the estimated probability density function (PDF) of the received V_{pp} in still, temperature and bubble turbulent water*

Turbulence Type	Distribution Type	SI of Fit, σ_{fit}^2	Fitting Parameter
Still (no turbulence)	Gaussian	0.0008	$R^2 = 0.98$
Temperature fluctuation	Generalised Gamma [130]	0.0332	$R^2 = 0.93$
Bubble induced	Exponential Log-normal [131]	0.0394	$R^2 = 0.99$

Table 4.2: *The fitting parameters for fitted curve in Figure. 4.5*

4.4.2 Laser and System Characterisation

A preliminary evaluation was conducted to inform system parameter selection and to characterise the two parallel Tx-receiver (Rx) paths. Understanding any performance variations between the components in each polarisation state is critical for a fair comparison.

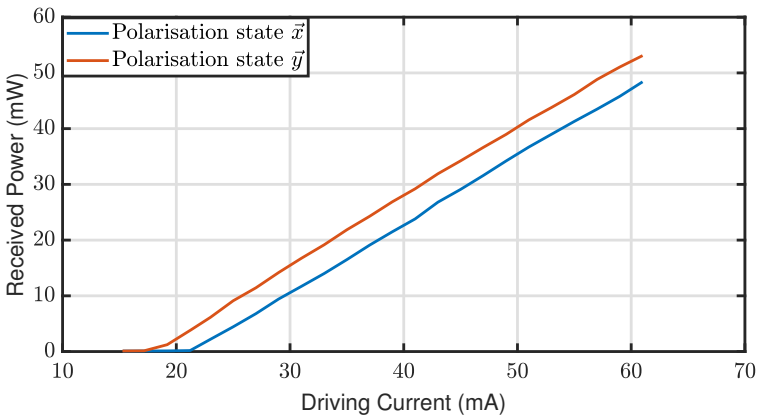

Figure 4.6: *P-I curve for the lasers in the two orthogonal polarisation states, measured after the polarising beam combiner.*

Figure 4.6 displays the optical power versus bias current (P-I) curves for the two lasers, measured at the output of the PBC. The threshold currents for the $\vec{x}$ and $\vec{y}$ polarised lasers are 18 mA and 22 mA, respectively. This difference implies that for an identical bias current, the $\vec{y}$ polarised laser would emit more optical power. Both lasers exhibit a high degree of linearity beyond their threshold currents, which is essential for IM/DD systems. To equalise the transmitted optical power from both sources, the bias currents were set based on these P-I curves. An I_{bias} of 43 mA was applied to the $\vec{x}$ laser and 40 mA to the $\vec{y}$ laser, ensuring that both transmitted approximately 27 mW of optical power.

The end-to-end normalised frequency response for each polarisation state is shown in Fig. 4.7. The two channels exhibit nearly identical responses, with a -3 dB bandwidth of approximately 900 MHz, followed by a steep roll-off. This bandwidth limitation, primarily dictated by the photodetectors, ultimately constrains the maximum achievable data rate of the system.

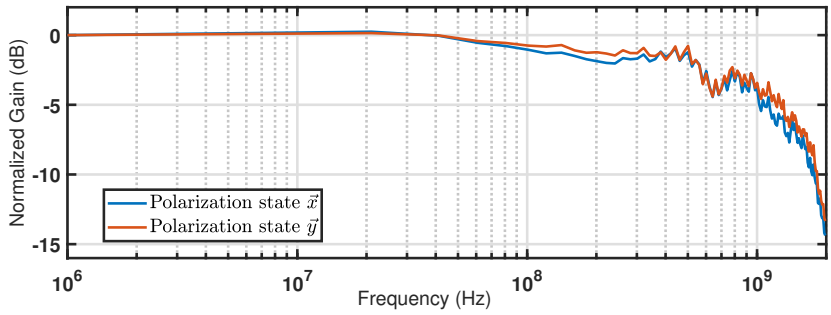

Figure 4.7: *Normalised frequency response of each polarisation state in still water.*

4.5 Results and Discussion

This section compares the performance of FSK without PDM and FSCM without PDM, then demonstrate how turbulence affect frequency-based modulation with PDM (e.g. FSK-PDM), and the performance of FSK with PDM and FSCM with PDM are compared at last.

4.5.1 FSK vs FSCM

Firstly, the performance of FSCM and FSK-SIM is compared experimentally in the previously described UOWC channel conditions. When only one polarisation state laser is used, we can get the performance of FSK and FSCM with no PDM.

Figure 4.8 presents the BER against symbol rate for FSCM and FSK with $M = \{2, 4, 8, 16\}$ at a given SNR. For both schemes, as the modulation order increases, the symbol rate at which the BER exceeds the forward error correction (FEC) limit of 3×10^{-3} decreases, as expected. Below the FEC limit, coding techniques can be applied to make the transmission effectively error-free. When the modulation order is 2, the BER curves of FSCM and FSK are close to each other, indicating that 2-FSCM has a similar performance to 2-FSK. However, when M is higher than 2, there are more subcarriers available in each symbol, and the advantages of using FSCM become apparent. Specifically, FSCM consistently achieves a higher symbol rate than FSK at modulation levels of 4, 8 and 16. These results are in-line with the theoretical expectation based on the description of FSCM and FSK in Section 4.2.3.

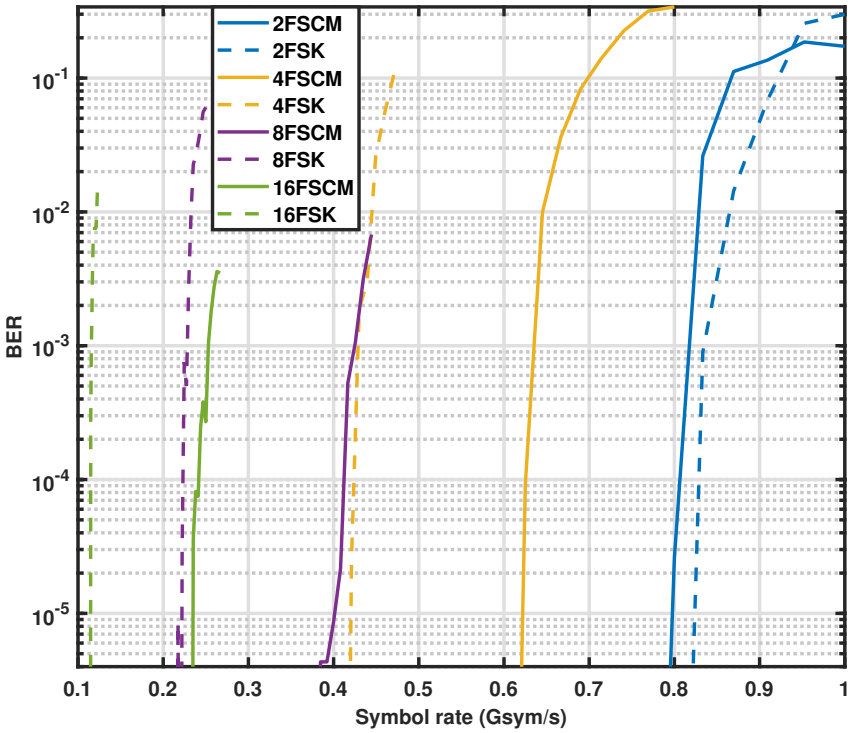

Figure 4.8: *BER against symbol rate for M-FSK and M-FSCM in still water.*

Figure 4.9 gives the comparative results between FSCM and FSK in the three conditions of turbid water in terms of the maximum achievable data rate. The turbidity of a channel can be characterised by its extinction coefficient, which represents the probability that a photon will experience an interaction over the link distance. As the extinction coefficient increases beyond 0.2 m^{-1}, the data rate falls as the received power decreases. When the extinction coefficient is

less than 0.2 m^{-1}, the maximum data rate is 1.25 Gbps, achieved with 8-FSCM, compared to a maximum of 850 Mbps achievable with 4-FSK. However, as turbidity increases, the performance of FSCM degrades faster than that of FSK, eventually becoming similar. At an extinction coefficient of 1.5 m^{-1}, 4-FSK and 8-FSK achieve the maximum data rate at around 560 Mbps, while 4-FSCM and 8-FSCM have the lowest data rates at about 380 Mbps and 480 Mbps. It can be concluded that both techniques suffer from decreasing SNR due to turbidity, but FSK maintains a more robust data transmission performance than FSCM under low SNR conditions. This behaviour can be understood from the detection mechanism of each scheme: in FSK-SIM, each symbol is decoded by comparing the power of competing subcarriers, a relative comparison that is immune to uniform channel-induced amplitude scaling. In FSCM, symbol detection relies on cross-correlation between the received chirp and reference waveforms; at very low SNR caused by severe turbidity or strong turbulence, noise degrades this correlation across all symbol candidates simultaneously, increasing the probability of error. FSK's single-frequency comparison is therefore more tolerant to low-SNR conditions.

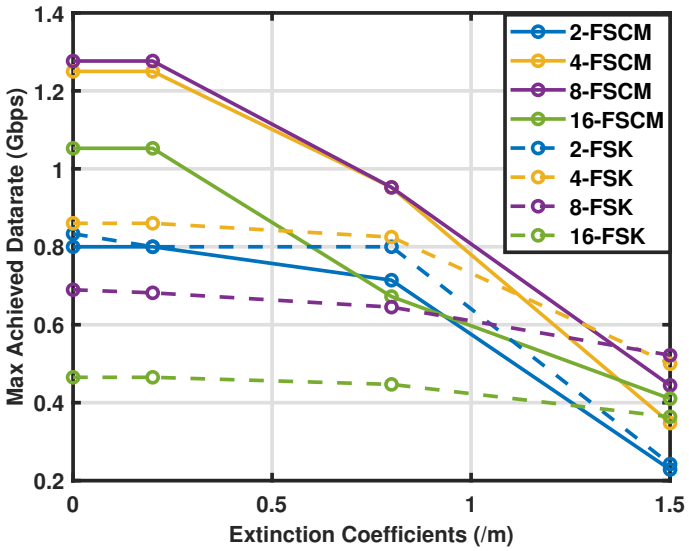

Figure 4.9: *Performance of M-FSK and M-FSCM in different turbidity levels.*

The results for maximum data rate achieved by FSCM and FSK in turbulent water are shown in Figure 4.10. When temperature-induced turbulence is present with a scintillation index (SI) of 0.15, 4-FSCM and 8-FSCM achieve the highest data rate of around 1 Gbps. However, FSCM's performance deteriorates rapidly with much stronger turbulence, with 4-FSCM degrading by approximately 65% at SI = 0.25, eventually approaching that of FSK. On the other hand, FSK

maintains a relatively stable performance trend, showing only about 36% reduction across the same turbulence range. Thus, it can be concluded that FSCM has some resilience against weak turbulence ($SI \approx 0.15$), but its performance degrades and is similar to that of FSK under strong turbulent conditions ($SI \approx 0.23$). A notable difference in performance is observed between the two types of turbulence. From Figure 4.10b, it is observed that 4-FSCM and 8-FSCM achieve the highest data rate, and can maintain a data rate of over 1 Gbps even with increasing bubble-induced turbulence up to $SI \approx 0.18$, experiencing around 10% degradation. FSK has a more robust performance trend but a lower data rate with modulation levels of 4, 8 and 16, the degradtion is less than 5%. Furthermore, both FSCM and FSK exhibit a slower deterioration in performance compared to conditions of temperature-induced turbulence. This indicates that the fading caused by temperature-induced turbulence has a greater impact on the UOWC channel than that from bubbles whose sizes are larger than the wavelength of the light beam.

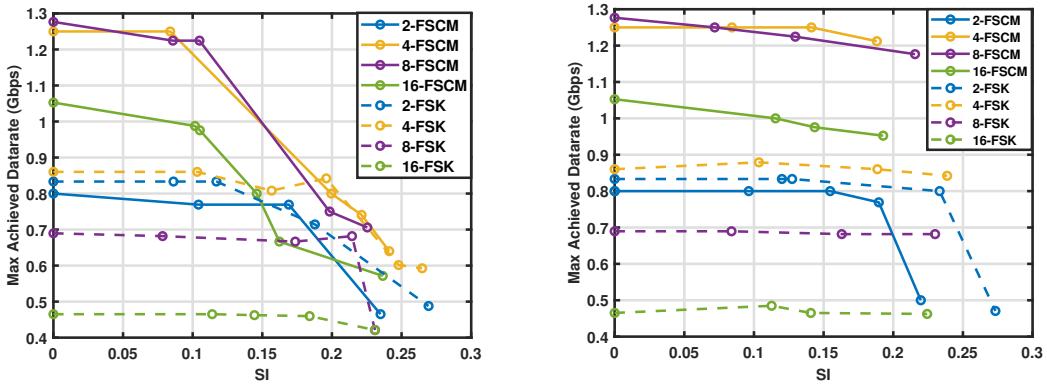

(a) *Temperature turbulent water* **(b)** *Bubble turbulent water*

Figure 4.10: *Maximum achievable data rate for M-FSK-SIM and M-FSCM-SIM under different levels of turbulence.*

The contrasting behaviour of FSCM and FSK across the two turbulence types can be understood from the underlying fading statistics. Temperature-induced turbulence produces spatially continuous and temporally correlated refractive index fluctuations, characterised by the Generalised Gamma distribution [130]. These sustained fluctuations coherently distort the chirp waveform across its full duration, progressively degrading the cross-correlation between the received signal and the reference chirp used in FSCM detection; this accounts for the approximately 65% reduction in 4-FSCM data rate as σ_I^2 rises from 0.15 to 0.25 in Fig. 4.10a. FSK, relying only on comparing instantaneous subcarrier power levels rather than waveform integrity across the symbol period, degrades more gradually at around 36% over the same range. Bubble-

induced turbulence, characterised by the Exponential Log-Normal distribution [131], imposes brief and localised deep-fading events rather than continuous waveform distortion. FSCM's wider instantaneous bandwidth means that such short-duration fades affect only a fraction of the chirp sweep, partially preserving the cross-correlation and limiting the data rate degradation to below 10% in Fig. 4.10b. This difference in sensitivity to the two turbulence types is consistent with the statistical channel models established in the literature and with the empirical distributions presented earlier in this chapter.

4.5.2 FSK with PDM

It is important to know how turbulence affects each polarised optical beam experimentally. In this case, two lasers with different polarisation state are applied. To demonstrate this, relative FSK-PDM performance is analysed, and the received intensity distributions for the two polarisation states ($\vec{x}$ and $\vec{y}$) in still and turbulent conditions are depicted in Fig. 4.11. In still water, the empirical probability density function (PDF) of both states exhibit a Gaussian-shaped PDF, confirmed by high R^2 values (0.97 for $\vec{x}$ and 0.95 for $\vec{y}$) for the Gaussian fits. In the presence of turbulence, the distributions deviate from Gaussian, with the R^2 values for the fits decreasing to 0.81 and 0.89, respectively, indicating that the Gaussian model is no longer adequate. Although the σ_I^2 values are similar for both states, slight differences in the distribution shapes are observable, which can be attributed to minor variations in optical alignment and the random nature of the turbulent eddies.

The received FSK-SIM-PDM signals are first evaluated using the power spectral density (PSD). Figure 4.12 shows the PSD at the $\vec{x}$ and $\vec{y}$ receivers when only one laser source is in use (i.e., 2-FSK-SIM) for a symbol rate of 740 mega symbols per second (Msym/s) in still water, as well as for $\vec{y}$ in turbulence. All three received PSDs exhibit two dominant frequencies, as is expected with 2-FSK-SIM. For the $\vec{y}$ polarised received signal, the dominant frequencies are around 50 dB above the noise floor. The PSD of the $\vec{x}$ polarised receiver shows the crosstalk component, which is a form of inter-channel interference (ICI). Here, the $\vec{x}$ polarised ICI term is shown to be below the noise floor of the $\vec{y}$ polarised component. Thus, the ICI term is negligible. Additionally, it is shown that the PSD of the $\vec{y}$ component in the turbulent channel condition is broadly similar to that of still water. This confirms that the frequency component of the subcarrier signal is shielded from the effect of turbulence.

Figure 4.13 shows the BER curve of FSK-SIM-PDM and the BER curves of the constituent

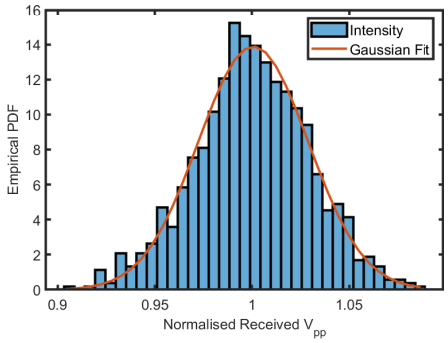

(a) *State* $\vec{x}$, $\sigma_I^2 = 8.7 \times 10^{-4}$

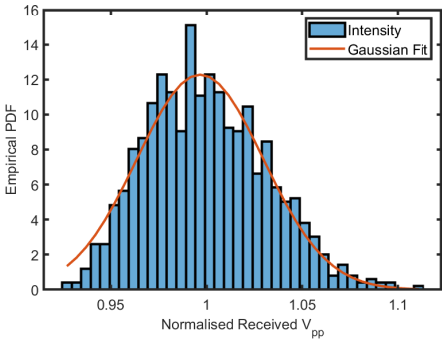

(b) *State* $\vec{y}$, $\sigma_I^2 = 9.8 \times 10^{-4}$

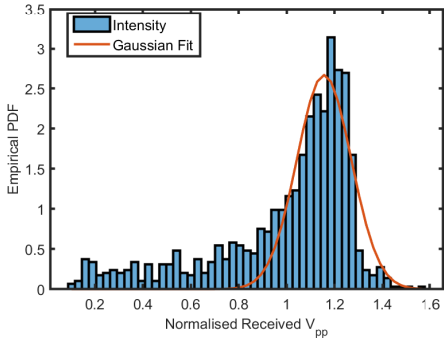

(c) *State* $\vec{x}$, $\sigma_I^2 = 0.083$

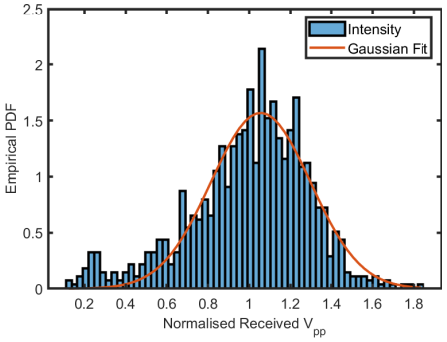

(d) *State* $\vec{y}$, $\sigma_I^2 = 0.084$

Figure 4.11: *Histograms showing the probability density function (PDF) of the received peak-to-peak voltage (V_{pp}) in still water (a, b) and turbulent condition (c, d), fitted with a Gaussian PDF.*

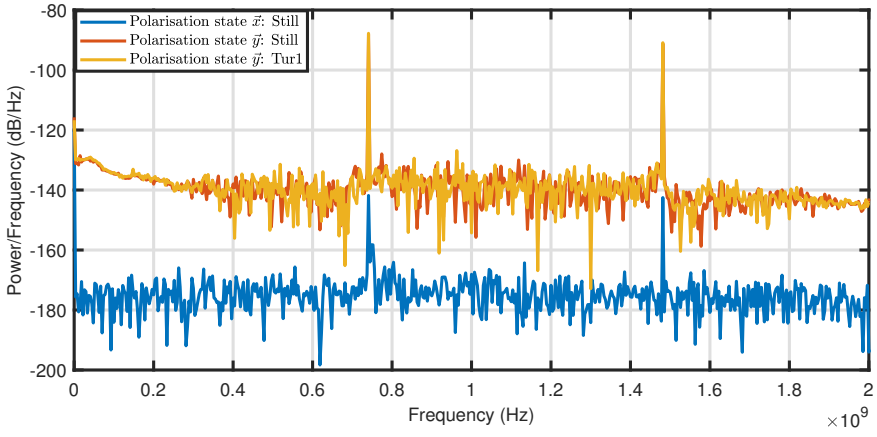

Figure 4.12: *The PSD of 2-FSK-SIM in still and turbulent 1 ($\sigma_I^2 \approx 0.10$) water, for a symbol rate of 740 Msym/s.*

FSK-SIM signals for the $\vec{x}$ and $\vec{y}$ polarisation states. The overall BER of FSK-SIM-PDM is the mean of the BER from the individual polarisation states. It is useful to compare the $\vec{x}$ and $\vec{y}$ BER curves. Both are expected to have identical BER. In Fig. 4.13, it is shown that the two polarisation states have similar performance in all water conditions considered. For all conditions, the BER performance of the two individual polarisation states are identical. Thus, it can be noted that PDM hardly distinguish the performance of FSK-SIM running in different polarisation state. For turbulence condition 2, when $\sigma_I^2 \approx 0.18$, the average BER values of FSK-SIM-PDM increase further, but there is no obvious gap between the curves under conditions of $\sigma_I^2 \approx 0.10$ and $\sigma_I^2 \approx 0.18$. This can be explained by FSK-SIM-PDM keeping the nature of FSK-SIM, where as long as the signal power is greater than the noise floor, it can be decoded accurately.

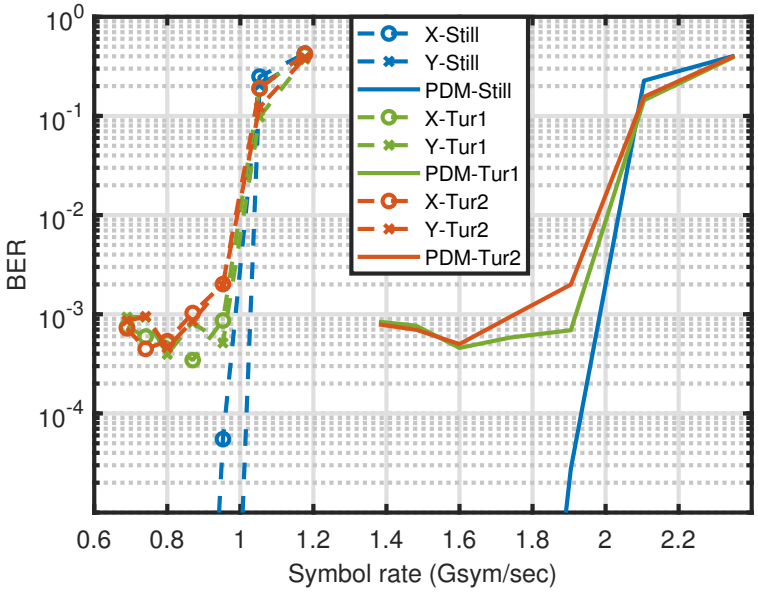

Figure 4.13: *BER vs symbol rate for 2-FSK-SIM-PDM and the individual 2-FSK-SIM carried in each polarisation state in still, turbulent 1 ($\sigma_I^2 \approx 0.10$) and turbulent 2 ($\sigma_I^2 \approx 0.18$) water channels.*

Figure 4.14 shows a comparison between 2-FSK-SIM and 2-FSK-SIM-PDM in different turbulence levels in terms of BER. As expected, the BER vs R_s curves exhibit a similar shape to those in Fig 4.13. Therefore, it can be concluded that the error performance of 2-FSK-SIM is not affected by using PDM, and ICI from orthogonal polarisation states is not degrading system performance.

Figure 4.15 summarises the maximum data rate achieved for which a BER below 10^{-3} is

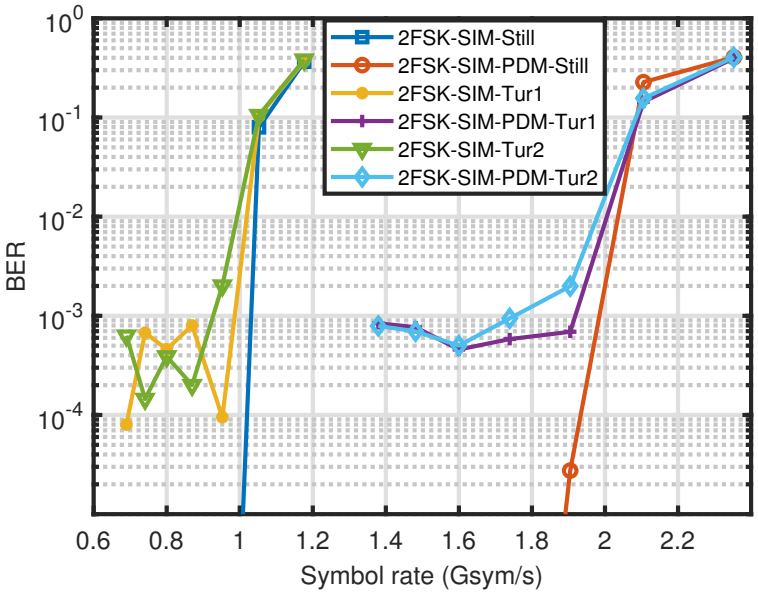

Figure 4.14: *BER curve for 2-FSK-SIM-PDM and 2-FSK-SIM only in still, turbulent 1 ($\sigma_I^2 \approx 0.10$) and turbulent 2 ($\sigma_I^2 \approx 0.18$) water channels.*

achieved under different underwater turbulence conditions. The maximum data rate achieved using 2-FSK-SIM-PDM is approximately double that of 2-FSK-SIM. The resilience to the effects of turbulence is confirmed through the maximum data rate in different water conditions. A data rate of 1.9 Gbps is achieved in still water using 2-FSK-SIM-PDM, and this performance is maintained when $\sigma_I^2 \approx 0.1$. Further, when $\sigma_I^2 \approx 0.18$, the data rate only falls by 8% to 1.75 Gbps. This relationship is repeated in 2-FSK-SIM, albeit with the data rates halved, with 0.95 Gbps achievable up to $\sigma_I^2 \approx 0.1$, falling by 10% to 0.85 Gbps.

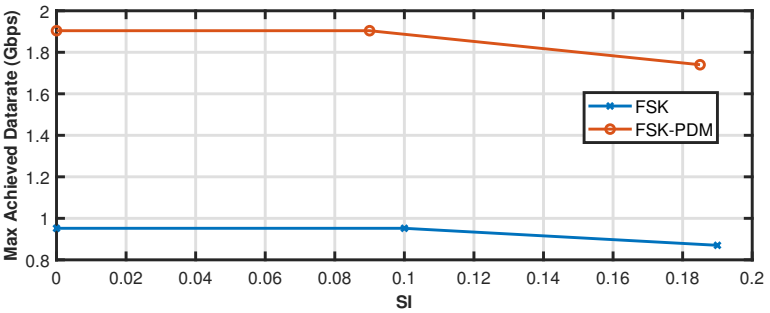

Figure 4.15: *A comparison of maximum achieved data rate across scintillation indices using 2-FSK-SIM-PDM and 2-FSK-SIM only.*

4.5.3 FSK with PDM vs FSCM with PDM

Having confirmed in Section 4.3 that the inter-channel interference introduced by PDM is negligible, this section compares the performance of FSK-SIM and FSCM with PDM across all tested channel conditions. Figure 4.16 shows the BER as a function of symbol rate (R_s) for M-FSK-SIM (single polarization, dashed lines) and M-FSK-SIM-PDM (dual polarization, solid lines) in still water. The observed trends demonstrate that for a fixed scheme (FSK or FSK-PDM), the BER increases with increasing symbol rate due to inter-symbol interference (ISI) becoming more significant as the symbol duration decreases relative to the channel dispersion and system bandwidth limitations. Also, for a fixed symbol rate, the BER increases with higher modulation order M, as the required frequency separation between subcarriers decreases, making the system more susceptible to noise and interference. Comparing FSK-SIM and FSK-SIM-PDM, the curves for the same modulation order M show very similar BER performance. This indicates that, in still water, the introduction of PDM does not significantly degrade the signal quality or introduce substantial crosstalk between the polarization channels, validating the effectiveness of the polarization combining/splitting. The primary benefit of PDM is doubling the data rate for a given symbol rate and modulation order. For example, 2-FSK-PDM achieves the highest symbol rate (approx. 2 GSym/s) below the FEC limit, corresponding to a data rate of 4 Gbps.

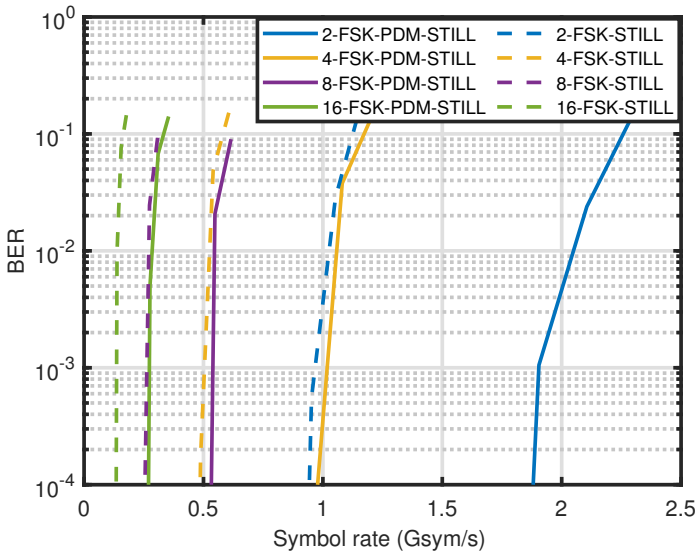

Figure 4.16: *BER versus symbol rate for M-FSK-SIM (dashed lines) and M-FSK-SIM-PDM (solid lines) with $M \in \{2, 4, 8, 16\}$ in still water.*

Figure 4.17 presents the corresponding BER curves for M-FSCM-SIM and M-FSCM-SIM-PDM in still water. Similar trends are observed: BER increases with symbol rate and modulation order. Again, the performance of FSCM-SIM and FSCM-SIM-PDM is nearly identical for the same M, confirming that PDM does not introduce significant penalties in still water for this scheme either. Comparing Fig. 4.17 with Fig. 4.16, FSCM-based schemes generally achieve lower BER for a given symbol rate and modulation order, or equivalently, support higher symbol rates at the FEC limit. For instance, 4-FSCM-PDM reaches the FEC limit at approximately 1.4 GSym/s (data rate 2.8 Gbps), whereas 4-FSK-PDM reaches it around 1.05 GSym/s (data rate 2.1 Gbps). This suggests FSCM-SIM may be inherently more robust or power-efficient, even in the absence of significant turbulence.

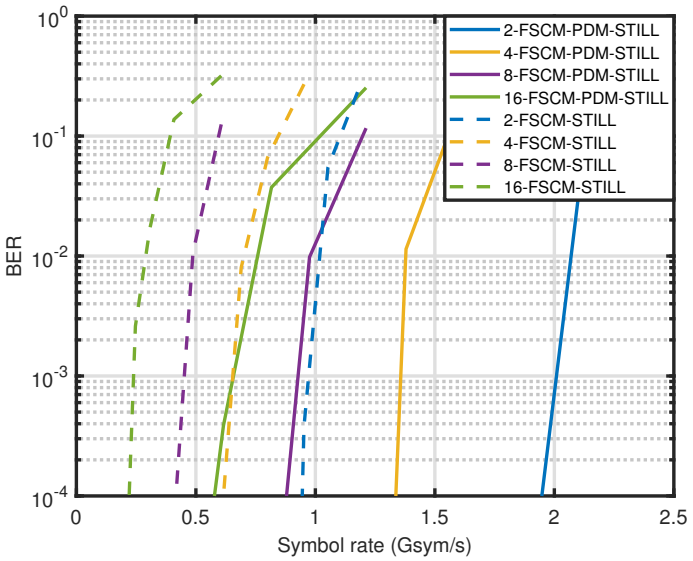

Figure 4.17: *BER versus symbol rate for M-FSCM-SIM (dashed lines) and M-FSCM-SIM-PDM (solid lines) with $M \in \{2, 4, 8, 16\}$ in still water.*

Figure 4.18a summarizes the maximum achievable data rate for M-FSK-SIM and M-FSK-SIM-PDM as a function of the measured SI under temperature-induced turbulence. For all modulation orders and turbulence levels, FSK-SIM-PDM achieves approximately double the data rate of FSK-SIM. The data rates for FSK-SIM show remarkable resilience to increasing turbulence, especially for lower modulation orders. For example, 2-FSK-PDM maintains a data rate close to 1.9 Gbps up to $\sigma_I^2 \approx 0.2$, only dropping slightly to around 1.75 Gbps at $\sigma_I^2 \approx 0.25$. Figure 4.18b shows the maximum data rates for M-FSCM-SIM and M-FSCM-SIM-PDM under temperature-induced turbulence. Similar to FSK, FSCM-SIM-PDM consistently

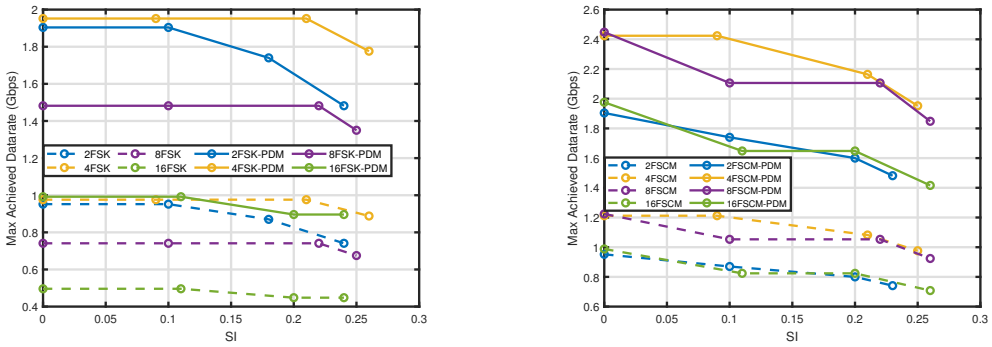

(a) *FSK-SIM* **(b)** *FSCM*

Figure 4.18: *Maximum achieved data rate in temperature-induced turbulence.*

achieves roughly double the data rate of FSCM-SIM. FSCM-SIM also demonstrates resilience to turbulence, although the performance degradation with increasing σ_I^2 appears slightly more pronounced compared to FSK-SIM. For example, 4-FSCM-PDM achieves around 2.4 Gbps in still water, dropping to 1.95 Gbps at $\sigma_I^2 \approx 0.25$. FSCM-PDM generally achieves higher data rates than FSK-PDM in still water and lower turbulence ($\sigma_I^2 \leq 0.1$). However, under stronger turbulence ($\sigma_I^2 \geq 0.2$), FSK-PDM seems to maintain its performance slightly better.

Figure 4.19a displays the maximum data rates achieved by FSK-based schemes under bubble-induced turbulence. The doubling of data rate with PDM persists. FSK-SIM demonstrates strong resilience, with data rates remaining relatively stable. For instance, 2-FSK-PDM and 4-FSK-PDM maintain rates around 1.9 Gbps in still water, dropping only to about 1.6 Gbps at $\sigma_I^2 \approx 0.25$. Figure 4.19b shows the performance of FSCM-based schemes under bubble-

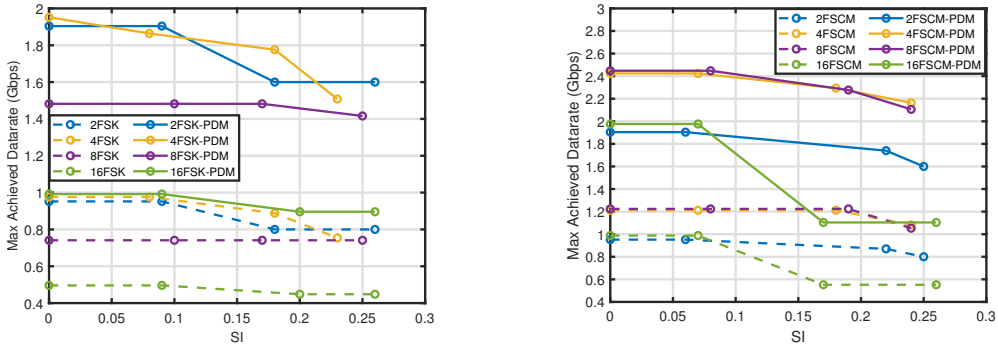

(a) *FSK* **(b)** *FSCM*

Figure 4.19: *Maximum achieved data rate in bubble-induced turbulence.*

induced turbulence. PDM consistently doubles the throughput. FSCM-SIM exhibits excellent resilience, arguably even better than FSK-SIM under these conditions. Notably, 4-FSCM-PDM and 8-FSCM-PDM achieve rates around 2.5 Gbps in still water, decreasing only to approximately 2.1 Gbps at $\sigma_I^2 \approx 0.25$. Under bubble-induced turbulence, FSCM-SIM consistently outperforms FSK-SIM.

Figure 4.20a illustrates the impact of water turbidity on the maximum data rates for FSK-based schemes. As the extinction coefficient increases, the data rate decreases significantly for all schemes due to lower SNR. PDM continues to provide a twofold increase in data rate. Figure 4.20b shows the performance of FSCM-based schemes under varying turbidity levels. The data rate doubling effect of PDM holds. Similar to FSK, increasing turbidity leads to a marked decrease in achievable data rates. Comparing the two schemes, FSCM-based approaches consistently achieve higher data rates than their FSK counterparts at the same turbidity level.

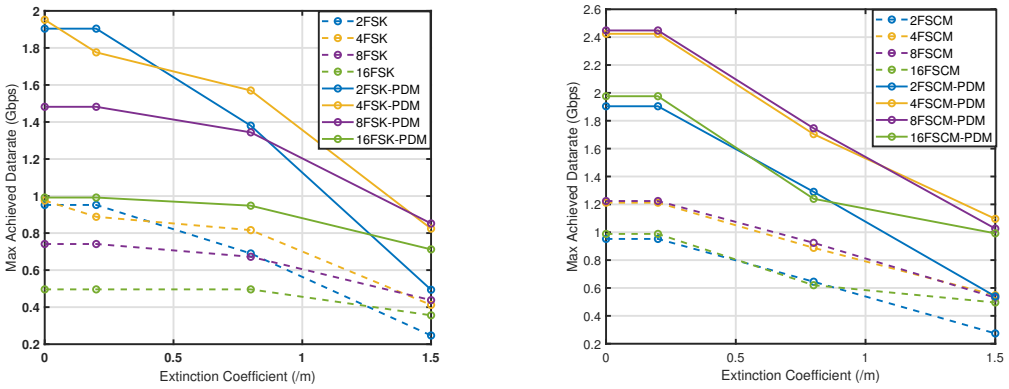

(a) *FSK* **(b)** *FSCM*

Figure 4.20: *Maximum achieved data rate in turbid water.*

4.6 Summary

This chapter presented an empirical study of frequency-based modulation schemes, FSK-SIM and FSCM, for UOWC channels, with a focus on their performance when combined with PDM. The experimental results demonstrated that both schemes are inherently resilient to turbulence-induced fading, as the information encoded in the frequency domain is largely unaffected by amplitude fluctuations. As discussed in Section 4.5, this robustness advantage of FSK over FSCM under severe turbidity and strong turbulence conditions stems from FSK's

relative subcarrier-power detection, which is resistant to amplitude fading, whereas FSCM's cross-correlation detection becomes less reliable as the SNR falls.

In still and low-turbidity water, FSCM consistently outperformed FSK in terms of achievable data rate, owing to its more efficient use of subcarriers. However, under severely attenuated (highly turbid) or strongly turbulent conditions, the simpler FSK scheme proved to be more robust. The study also confirmed that PDM is a highly effective technique for doubling the system throughput, introducing negligible crosstalk or performance degradation in the tested conditions. The 2-FSK-SIM-PDM system achieved a robust data rate of 1.75 Gbps even under moderate turbulence, validating the potential of this combined approach for building high-capacity, resilient UOWC links.

Chapter 5
Fine Tracking System for Optical Wireless Communication

5.1 Introduction

A primary challenge in establishing reliable OWC links, particularly over long distances or in mobile scenarios, is maintaining precise alignment between the transmitter and receiver. Misalignment, caused by factors such as building sway, platform vibration, or atmospheric beam wander, can lead to significant signal degradation and potential link failure. While resilient modulation schemes can mitigate the effects of fading, they cannot compensate for a complete loss of signal when the beam deviates from the detector's active area. Therefore, an active tracking system is proposed for ensuring link robustness. There are various optical beam tracking systems have been investigated and proposed in the literature [97, 99, 100, 102–104, 132], and a summary is as shown in Table. 5.1. Notwithstanding these promising advancements, significant hurdles in optical beam tracking persist, including complexities in practical implementation, prohibitive costs for some applications, and susceptibility to interference from fluctuating channel conditions.

To address these outstanding issues with a focus on accuracy and cost-effectiveness, this chapter details the design, modelling, and experimental demonstration of a fine beam tracking system for OWC. The system is designed to detect beam displacement in real-time and actuate a receiver board to maintain optimal alignment, thereby maximising the received signal power and ensuring link stability.

The chapter begins with a theoretical analysis of the effect of misalignment on a received Gaussian beam, quantifying the relationship between beam displacement and power loss. Following this, the principles and system model of the proposed tracking receiver are presented, including the design of the photodetector array and the control algorithm. The experimental setup, which incorporates a fast steering mirror to emulate dynamic misalignment, is then described in detail. The performance of the tracking system is evaluated under both static and dynamic conditions

Tracking Approach & Reference	Hardware Components	Operating Principle
Camera with LED Markers [97]	Camera with infrared LED markers	Visual serving with marker detection
TDOA Triangulation [99]	Multiple synchronized receivers	Time difference of arrival triangulation
Liquid Lens Adaptive Optics [100]	Silicon PD with liquid lenses	Adaptive focus adjustment for beam steering
MEMS Mirror Beam Steering [102]	MEMS mirror, beam splitter, PD array	Split beam for simultaneous data and tracking
MobileNetV2 Neural Network [103]	Underwater camera with MEMS mirror	Neural network extracts beam position from distorted images
ResNet Neural Network [104]	Underwater camera with MEMS mirror	Deep learning for position estimation through waves
Image-Based Real-time Tracking [132]	Mobile camera with processing unit	Real-time image analysis for beam centroid detection

Table 5.1: *Overview of Optical Beam Tracking Approaches in Literature*

in free-space and underwater channels. The results demonstrate the system's effectiveness in maintaining link integrity under various misalignment scenarios, highlighting its potential for practical OWC deployments.

5.2 Misalignment and Tracking System Modelling

5.2.1 Misalignment Impact on Received Signal Strength

To quantify the impact of misalignment on a VLC link, a two-dimensional (2D) simulation is developed based on a Gaussian beam model that explicitly incorporates beam displacement. At the receiver plane, the transverse intensity profile of the Gaussian beam is described by [133]:

$$I(x, y) = I_0 \cdot \exp\left(\frac{-2\left(x^2 + y^2\right)}{\omega_0^2}\right). \tag{5.1}$$

In this context, I_0 represents the maximum optical intensity at the beam's centre, while ω_0 denotes the beam waist radius at the receiver plane, defined as the radius where the beam's intensity drops to $1/e^2$ (approximately 13.5%) of its central maximum I_0. The variables x and y designate the coordinates of the position under consideration. In practical systems, the displacement is both random and time-varying, necessitating a tracking/alignment system.

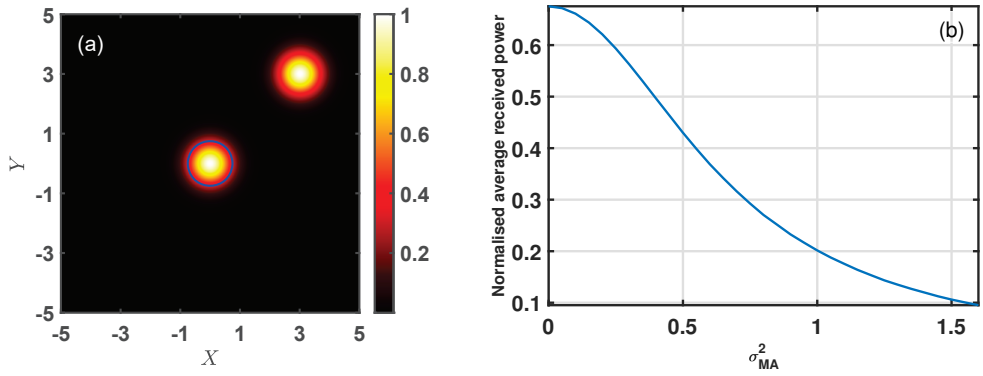

Figure 5.1: *(a) Gaussian optical beam position and power colour map; (b) The normalised average received power against different misaligned signal variance,* σ^2_{MA}

The intensity of a Gaussian beam, when misaligned and shifted by Δx and Δy from its initial

position (x_0,y_0), transforms to:

$$I_{\text{MA}}(x, y) = I(x_0 \pm \Delta x, y_0 \pm \Delta y). \tag{5.2}$$

Figure 5.1(a) illustrates both ideal and misaligned beam positions. In the ideal case, the Gaussian beam is perfectly centred at the origin $(x, y) = (0, 0)$. In a representative misaligned scenario, the centre of the beam is displaced to $(x, y) = (3, 3)$. As a direct consequence, a small-area receiver positioned at the origin (depicted by the blue circle) would receive no optical signal from this displaced beam. It is important to mention that both simulations utilise the normalised intensity, I_0, and the beam waist, ω_0, constrained within a $\pm 5\omega_0$ range on the X and Y axis. This integration boundary is chosen because, for a Gaussian beam with intensity profile $I \propto \exp(-2r^2/\omega_0^2)$, the fraction of total beam power falling outside a radius of $5\omega_0$ is $\exp(-2 \times 25) \approx 10^{-22}$, which is negligible for any practical purpose. Setting the simulation boundary at $\pm 5\omega_0$ therefore captures essentially all incident optical energy whilst keeping the numerical integration domain computationally tractable.

To assess the fractional power loss due to misalignment, the received optical power under misalignment is normalised by the total power incident on the receiver plane. This normalised power, P_{MAnorm}, is calculated as:

$$P_{\text{MAnorm}} = \frac{\int_{-r}^{r} \int_{-\sqrt{r^2-x^2}}^{\sqrt{r^2-x^2}} I_{\text{MA}} \mathrm{d}x\mathrm{d}y}{\int_{-x_{\text{Lim}}}^{x_{\text{Lim}}} \int_{-y_{\text{Lim}}}^{y_{\text{Lim}}} I \mathrm{d}x\mathrm{d}y}. \tag{5.3}$$

Here, x_{Lim} and y_{Lim} define the integration bounds (set to $\pm 5\omega_0$ to capture nearly all incident power). For this illustrative simulation, a receiver radius of $r = 0.75\omega_0$ is assumed. Figure 5.1(b) then shows how random misalignment, characterised by increasing variance σ^2_{MA}, affects this normalised received optical power. With no misalignment ($\sigma^2_{\text{MA}} = 0$), the simulation yields a peak normalised received power of 0.67. This value is less than unity because the assumed receiver radius ($r = 0.75\omega_0$) captures only 67% of the total incident Gaussian beam power. As the misalignment variance σ^2_{MA} increases from 0 to 1.6, the normalised received average optical power diminishes from 0.67 to 0.1, clearly demonstrating the detrimental impact of increasing beam deviation from the detector's active area.

5.2.2 The Proposed Tracking System

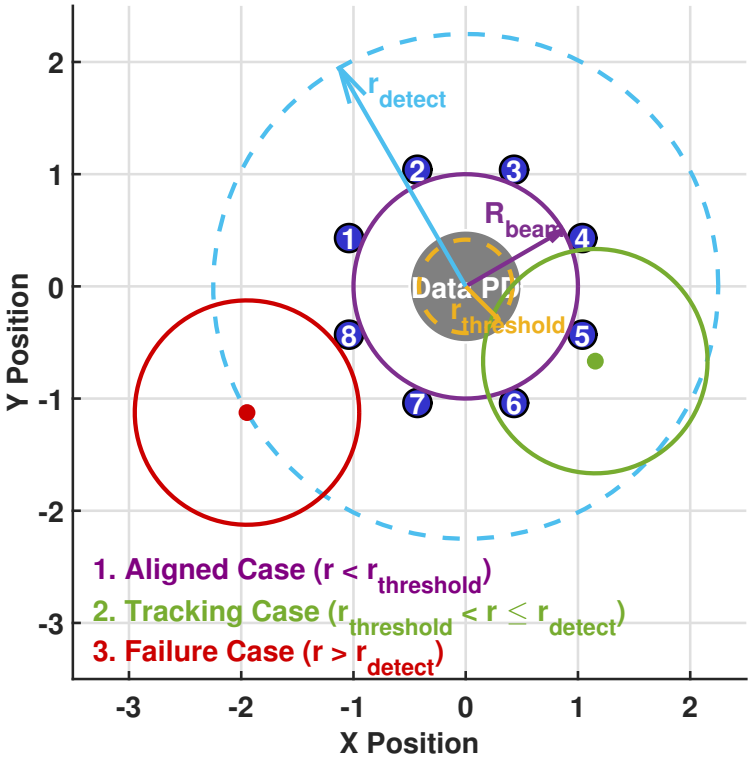

Figure 5.2: *Tracking system geometry and three operating conditions*

To mitigate the detrimental effects of misalignment in OWC systems, the receiver board illustrated in Fig. 5.2 is proposed. The board features a central data photodiode (PD) circumferentially surrounded by an array of eight tracking PDs. These tracking PDs are grouped into four pairs (e.g., PDs 1 and 2 form one pair), creating four distinct differential channels oriented to detect beam displacement from multiple directions. The data PD, located at the board's centre, is equipped with a lens/concentrator to maximise optical power reception. Due to its higher bandwidth compared to the tracking PDs, the data PD enables high-speed data transmission.

When misalignment occurs, the beam shifts from the central data photodiode (PD) towards the adjacent tracking PDs. As a result, the beam crosses one or more tracking PDs. The light received by the tracking PDs are processed via a microcontroller to estimate the misalignment and new location of the beam. The microcontroller then produces a control signal for the motors which adjusts the receiver board such that the data PD is moved to the light beam's new location. This system tracks the beam very well for as long as the misalignment is slower in speed than the combination of processing/actuator motor speed.

The operational logic for beam correction is governed by Algorithm 1. In essence, upon acquiring digitised readings from the four tracking channels, the microcontroller calculates differential intensity signals for both the left-right (DLR) and top-down (DTD) axis. It is important to note that before the readings are calculated into differential value, Kalman filtering is applied to reduce the fluctuation so that the differential intensity can be more accurate and less affected by the system noise. If the absolute magnitude of either differential signal exceeds a predefined threshold (TH), the corresponding motor (LRMotor or TDMotor) is activated. The motor's direction is determined by the sign of the differential signal, and its movement duration (StepLR/StepTD) is proportional to the extent by which the signal exceeds the threshold, thereby repositioning the receiver board to maximise the signal intensity at the data PD. In addition, it can also be noted that the algorithm only computes arithmetic operations with a fixed time duration, making it suitable for real-time implementation on basic low-cost microcontrollers.

5.2.3 The Tracking System Modelling

The tracking system shown in Fig. 5.2 is modelled here. Key parameters include $R_{\mathrm{beam}} = \omega_0$ shown by the purple arrow (beam waist radius), r_{data} (radius of data PD lens), D (distance from centre position to tracking PDs), r_{PD} (radius of each wide-area tracking PD), $r_{\mathrm{threshold}}$ (as the yellow arrow) shows displacement of the beam centre beyond which the SNR of received optical signal falls below a pre-defined threshold and r_{detect} (shown by the blue arrow) is the maximum detection range, given by $r_{\mathrm{detect}} = D + r_{\mathrm{PD}} + \omega_0$. In this receiver board design, a critical design constraint for effective tracking is:

$$r_{\mathrm{threshold}} + R_{\mathrm{beam}} \geq D. \tag{5.4}$$

This geometric constraint, given by (5.4), is fundamental: it guarantees that if the beam center drifts beyond the optimal alignment region ($r_{\mathrm{threshold}}$) but remains within the system's overall detection envelope (r_{detect}), at least one tracking PD channel will register the beam. This ensures that the system can detect the misaligned beam and initiate corrective action. Let the data PD location be (0,0). Following a misalignment, the new position of the beam centre, relative to the data PD's position, is given as, $r = \sqrt{\Delta x^2 + \Delta y^2}$. In this work, we assume the actuator range is greater than r, so that the beam always remains within the physical boundaries of the actuator. Based on this, we identify the following three operating conditions:

Algorithm 1 The Tracking Algorithm

Set threshold, TH
for Every time ADCs values are ready **do**
    $Channel1 \leftarrow ADC0$
    $Channel2 \leftarrow ADC1$
    $Channel3 \leftarrow ADC2$
    $Channel4 \leftarrow ADC3$
    $DLR \leftarrow (Channel1 + Channel3) - (Channel2 + Channel4)$
    $DTD \leftarrow (Channel1 + Channel2) - (Channel3 + Channel4)$
    if $abs(DLR) >= TH$ **then**
        $StepLR \leftarrow (abs(DLR) - TH)$
        if $DLR > 0$ **then**
            LRMotor moves to the left
        else if $DLR < 0$ **then**
            LRMotor moves to the right
        end if
    else if $abs(DLR) < TH$ **then**
        LRMotor stays idle
    end if
    if $abs(DTD) >= TH$ **then**
        $StepTD \leftarrow (abs(DTD) - TH)$
        if $DTD > 0$ **then**
            TDMotor moves upward
        else if $DTD < 0$ **then**
            TDMotor moves downward
        end if
    else if $abs(DTD) < TH$ **then**
        TDMotor stays idle
    end if
end for

Aligned Case: When the beam displacement $r \leq r_{\text{threshold}}$, the SNR is not below a predetermined threshold for a reliable communication. The beam is sufficiently aligned such that no tracking is required.

Tracking Case: When $r_{\text{threshold}} < r \leq r_{\text{detect}}$, the SNR falls below the threshold, but the beam still overlaps with one or more tracking PDs. The tracking system can detect misalignment and initiate corrective actions.

Failure Case: When $r > r_{\text{detect}}$, the beam does not overlap sufficiently with any tracking PD, making detection impossible. The tracking system fails, resulting in a deep fade.

Figure 5.2 illustrates these three operational conditions, with the purple, green, and red circles depicting sample beam positions for the aligned, tracking, and failure cases, respectively. Assuming misalignment to be a random process, the probability of the beam being sufficiently aligned, P_{aligned}, can be expressed by (5.5).

$$P_{\text{aligned}} = P(r \leq r_{\text{threshold}}). \tag{5.5}$$

Similarly, the probability of the tracking system being activated to correct misalignment, P_{tracking}, is given by (5.6).

$$P_{\text{tracking}} = P(r_{\text{threshold}} < r \leq r_{\text{detect}}). \tag{5.6}$$

Then, the probability of tracking system failure, P_{failure}, is defined by (5.7).

$$P_{\text{failure}} = P(r > r_{\text{detect}}). \tag{5.7}$$

For scenarios such as misalignment induced by the sway of high-rise buildings, the radial displacement, r, can be modelled using a Rayleigh distribution [134], as (5.8):

$$f_{\text{R}}(r) = \frac{r}{\sigma_{\text{MA}}^2} \exp\left(-\frac{r^2}{2\sigma_{\text{MA}}^2}\right), r \geq 0 \tag{5.8}$$

In (5.8), σ_{MA} represents the standard deviation of misalignment in each dimension. Utilising this distribution, the probabilities for each operating condition can be calculated as follows:

$$\begin{aligned} P_{\text{aligned}}(\sigma_{\text{MA}}) &= P(r \leq r_{\text{threshold}}) \\ &= 1 - \exp\left(-\frac{r_{\text{threshold}}^2}{2\sigma_{\text{MA}}^2}\right), \end{aligned} \tag{5.9}$$

$$
\begin{aligned}
P_{\text{tracking}}(\sigma_{\text{MA}}) &= P(r_{\text{threshold}} < r \leq r_{\text{detect}}) \\
&= \exp\left(-\frac{r_{\text{threshold}}^2}{2\sigma_{\text{MA}}^2}\right) - \exp\left(-\frac{r_{\text{detect}}^2}{2\sigma_{\text{MA}}^2}\right),
\end{aligned} \tag{5.10}
$$

$$
\begin{aligned}
P_{\text{failure}}(\sigma_{\text{MA}}) &= P(r > r_{\text{detect}}) \\
&= \exp\left(-\frac{r_{\text{detect}}^2}{2\sigma_{\text{MA}}^2}\right).
\end{aligned} \tag{5.11}
$$

The set of equations from (5.9) to (5.11) establishes a statistical framework to assess the likelihood of each operating condition (aligned, tracking, or failure) during the movement of the building, depending on the severity of the misalignment, σ_{MA}. This probabilistic model allows for the prediction of system performance under various misalignment scenarios and aids in the optimisation of critical geometric design parameters. It is important to note that the probability of alignment, as defined in (5.9), is contingent on the tracking system response speed (encompassing both the processing time and the motor actuation speed) being faster than the misalignment speed.

5.3 Experimental real-time demonstration

This section details the design and experimental evaluation of the tracking system modelled in previous section. The experimental investigation is designed to simulate building sway conditions. Angle of arrival (AOA) effects is not investigated, based on the premise that translational displacement effects are considerably more deleterious. The amount of sway in the experimental evaluation is guided by the serviceability standards for high-rise buildings (HRBs) that stipulate a maximum total building drift ration of $H/500$, where H is the height of the building. This standard, which corresponds to an approximate swaying angle of 0.115°, is intended to prevent non-structural damage such as cracking of partition walls [135]. Performance evaluation focusses on measuring the bit error rate (BER) and signal-to-noise ratio (SNR) across a range of controlled misalignment scenarios. A baseline SNR of -50 dB is established to represent a complete misalignment scenario, which corresponds to the noise floor where no discernible signal is received. Controlled misalignment is introduced into the experimental setup using a programmable fast steering mirror (FSM).

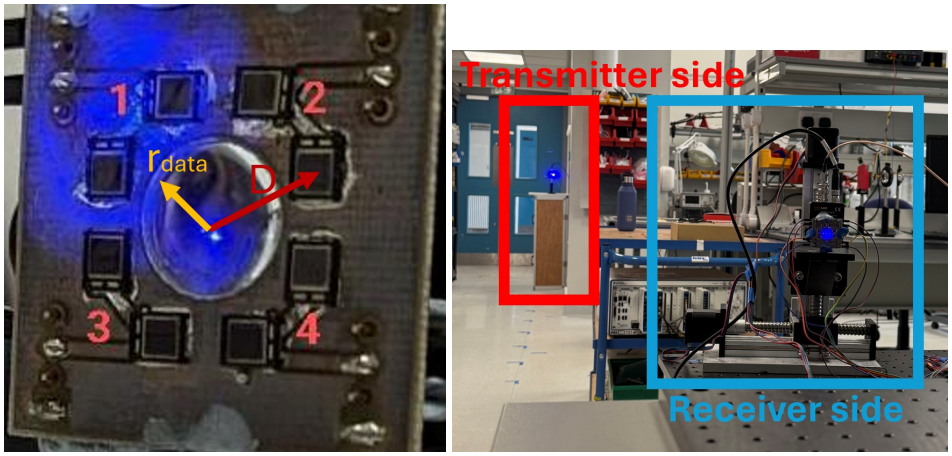

(a) *Receiver board* **(b)** *Propagation path*

Figure 5.3: *Demonstration of experimental setup*

5.3.1 Experimental Setup

The receiver board designed in this work is shown in Fig. 5.3(a). Each of the eight tracking photodiodes (SFH-2201) has an active radius (r_{PD}) of 0.6 mm. Other design parameters of the board are: Data PD lens effective radius (r_{data}) of 4 mm, centre-to-centre (D) of 9 mm between the data PD and the surrounding tracking PDs.

The experimental setup is illustrated by Fig. 5.4. Data modulation is based on 4-level frequency-shift keying subcarrier intensity modulation (4-FSK-SIM). This is implemented on a personal computer (PC-1) controlled Universal Software Radio Peripheral (USRP) X310. The choice of FSK-SIM is motivated by its constant envelope and inherent resilience to fading effect in received optical intensity, as this scheme encodes data onto the frequency of a subcarrier signal rather than its amplitude [67]. Within this experimental context, the use of FSK-SIM serves to distinctly isolate and highlight the tracking system's capability to counteract SNR degradation specifically attributable to misalignment. This allows for an unambiguous demonstration of the beam tracking system's performance, independent of the inherent robustness of the modulation scheme itself. The data signal from the USRP and the direct current (DC) bias, denoted as I_{bias}, are combined together using a bias-tee. The bias-tee output then intensity-modulates an Osram PL450b laser diode (LD). An optical front-end, comprising of an aperture and two collimating lenses, is employed to shape the output of the LD into a Gaussian beam profile. This optical beam subsequently propagates through an 8.5 m free-space channel towards a programmable fast steering mirror (FSM, model MR-15-30). The FSM is programmed to introduce controlled,

minor angular misalignments, which served to redirect the beam towards the receiver board, positioned at a distance of 1.1 m from the FSM. Figure 5.3(b) provides a visual depiction of the physical experimental arrangement, illustrating the FSM's perspective from which the transmitted beam is reflected towards the receiver assembly.

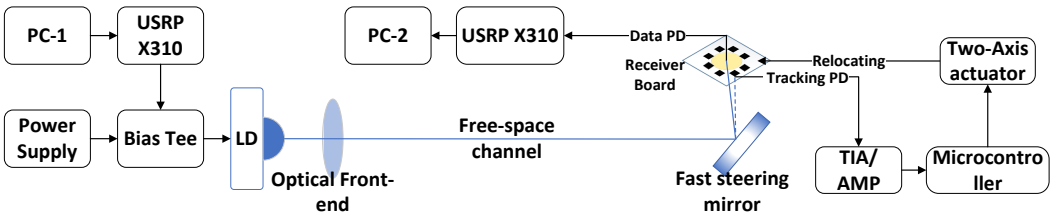

Figure 5.4: *The experimental setup diagram and proposed tracking scheme*

When the misaligned optical beam arrives at the receiver board, the current generated by PD is converted into readable voltage signal by the Transimpedance Amplifier and Post-Amplifier (TIA/AMP) circuit, and the system initiates real-time adjustments to the receiver board's position. Additionally, TIA/AMP circuit works under ± 15V and the current is between 69 mA to 74 mA. These positional adjustments are executed by a two-axis stage, which is driven by NEMA 17 stepper motors featuring a 1.8° step angle with a linear resolution of 0.025 mm per step. This stage provides a 10 cm travel range along both the X and Y axis. Control of the stepper motors is managed by DRV8825 driver modules. Data signal captured by the central data PD (Thorlabs PDA10AEC) is sampled by a second USRP X310 unit and subsequently processed and analysed in real-time on a dedicated personal computer (PC-2). Table 5.2 provides a summary of the operational response times of the experimental configuration. The initial detection phase, which is independent of motor activation, consistently requires 14 ms to complete. These empirically determined operational response times are substantially shorter

Operating distance (mm)	**Time Required (ms)**
Detection only	14
Motor operation for 0.25	14 + 15 = 29
Motor operation for 0.5	14 + 30 = 44
Motor operation for 0.75	14 + 45 = 59
Motor operation for 1.0	14 + 60 = 74

Table 5.2: *Operation Time Summary*

than the characteristic timescales of typical real-world misalignment phenomena. For instance, building sway frequently exhibits oscillation periods ranging from hundreds of milliseconds to several seconds [136], whilst wave-induced misalignments in underwater environments typically manifest on timescales of approximately 100 ms [137]. Consequently, the demonstrated response characteristics indicate the system's suitability for a broad spectrum of practical applications.

5.3.2 Channel Characterisation

The frequency response of the aligned system was first characterised. As shown in Fig. 5.5, the -3 dB bandwidth of the data PD is approximately 98 MHz. The frequency response of the designed tracking PD, measured before the microcontroller's analogue-to-digital converter (ADC), is shown in Fig. 5.6. The designed tracking channel has a much lower -3 dB bandwidth of around 1.6 MHz due to the much larger active area and higher gain. The plot also shows the processed differential voltage, which exhibits sharp drops at integer multiples of 500 kHz. This is an artifact of the microcontroller's 250 kHz per-channel sampling rate, which can lead to aliasing. To avoid this, the pilot signal frequency was set to 1.14 MHz.

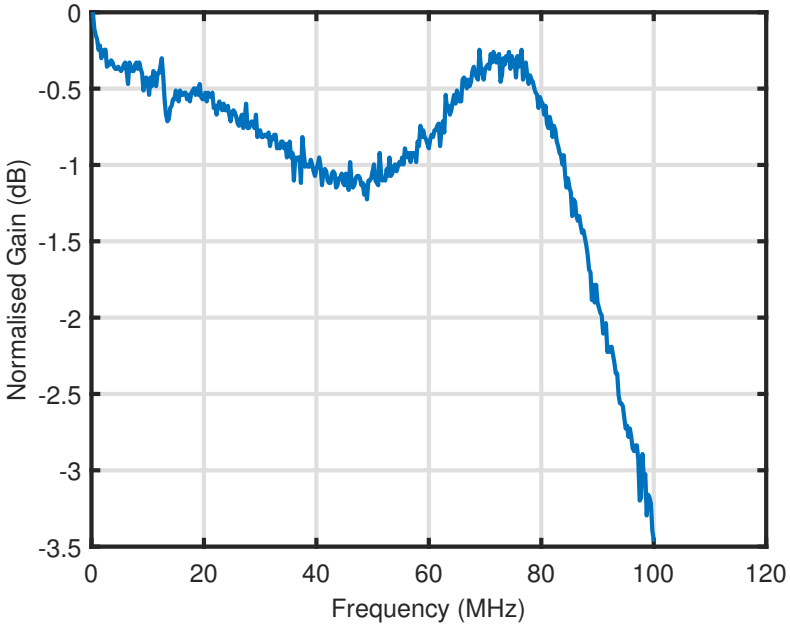

Figure 5.5: *Normalised frequency response of the data PD.*

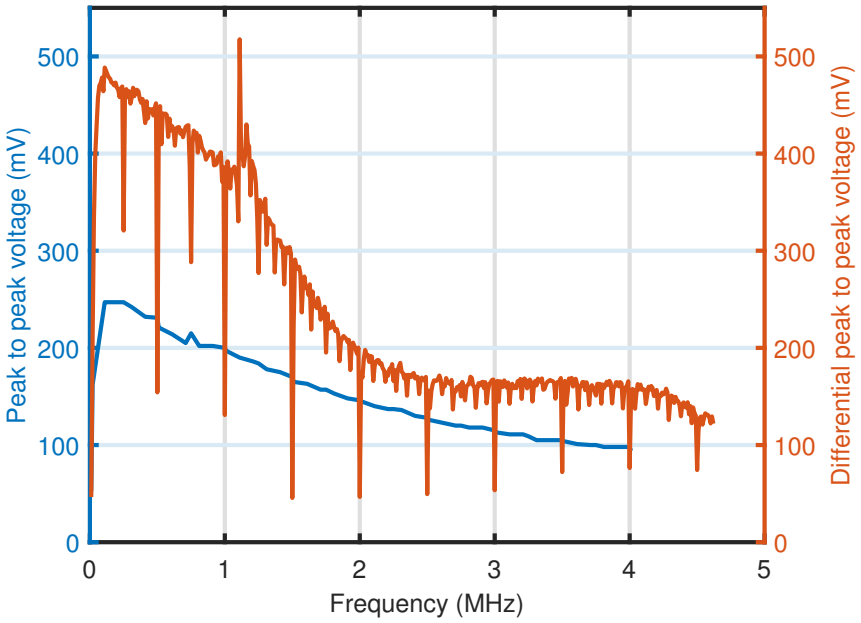

Figure 5.6: *Frequency response of the tracking PD path, showing the amplified signal before the microcontroller (left axis) and the processed differential voltage (right axis).*

5.3.3 Tracking System Static Evaluation

Prior to evaluating dynamic tracking, it is important to characterise the system's static response to misalignment, specifically its ability to detect displacement before corrective actions are initiated (i.e. detect the misaligned beam and work out the control signal for the stepper motors). For this static evaluation, the FSM is programmed to rotate incrementally within a range of $\pm 0.46°$ in the azimuth and elevation angles, causing the optical beam to scan a square area $17.57 \times 17.57\ \mathrm{mm}^2$ across the receiver board. During this phase, the step motors are disabled. Control signals from the microcontroller (indicative of detected misalignment) and the received signal strength from the data PD (via the USRP) are captured to assess the system's static detection performance.

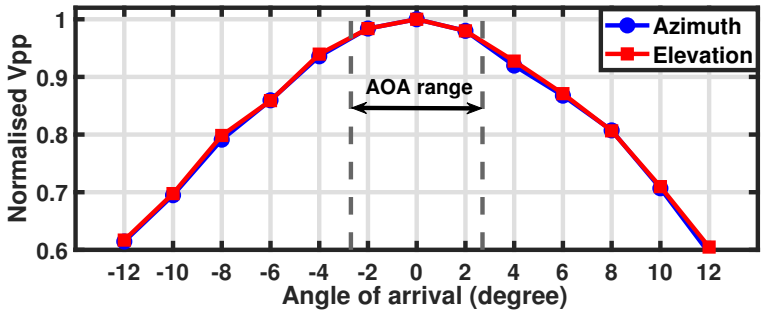

Figure 5.7: *Normalised received V_{pp} with different angle of arrival.*

To find out the effect of AOA in this work, the normalised received peak-to-peak voltage (V_{pp}) against different AOA is shown in Fig. 5.7. Since the distance from the mirror to the receiver board is 1.1 m and the range of the actuator is 10 cm along azimuth and elevation axis, we calculate the maximum angle of arrival in this work to be 2.7°. Figure. 5.7 shows the corresponding normalised V_{pp} is around 0.96, which means the AOA effect is very limited. Thus, given the small angular rotations employed and the large active area of the PD, any effects due to changes in the AOA at the receiver board are considered negligible for this static analysis. And the impact of AOA on the tracking system will be included in our follow-on long-range outdoor experimentation.

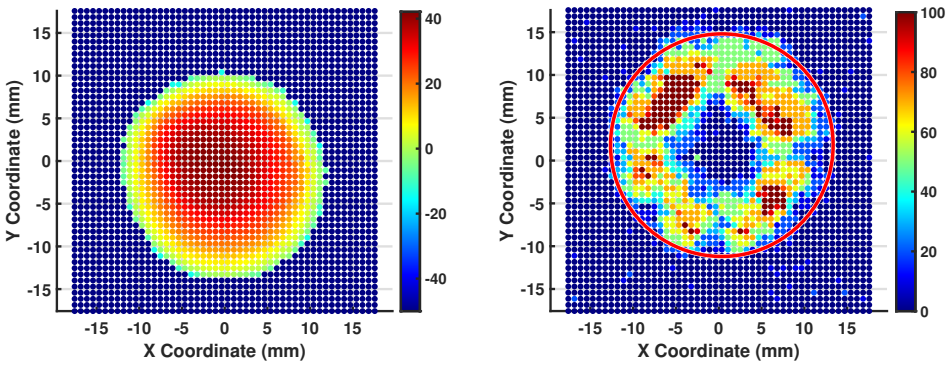

(a) *Profile of beam* **(b)** *Response of tracking PDs*

Figure 5.8: *Characterisation of the tracking system*

Figure 5.8(a) presents the empirically measured SNR across a 2D grid representing the receiver plane. The resulting map clearly reveals the Gaussian characteristics of the incident beam, with peak SNR (red) at its centre, which gradually diminishes (transitioning from red to yellow to green) with increasing radial distance. This experimentally obtained profile corroborates the

theoretical Gaussian beam model used in the earlier probability analysis (Section 5.2). Within this profile, the yellow region corresponds to an SNR of approximately 9 dB, occurring at a displacement of roughly 9 mm. The SNR value (9 dB) is set as the reference SNR threshold in this study, which defines an outage condition, as well as the trigger distance for corrective motor activation ($r_{\mathrm{threshold}}$). The 9 dB SNR threshold corresponds to a theoretical BER of 3.4×10^{-4} for 4-FSK-SIM modulation, providing a reliable link. With channel coding, this BER level can result in error-free transmission.

Figure 5.8(b) illustrates the combined sensitivity response of all four tracking channels, effectively mapping the system's overall reaction to beam misalignment. Each dot on the grid in Fig. 5.8(b) indicates the beam centre position, while its colour is indicative of the strength of the control signals sent to the step motors to correct the misalignment. This composite map reveals a distinct high-sensitivity ring-like pattern spatially correlating with the circular arrangement of the tracking PDs. The red circle in the figure shows the experimental maximum detection range (r_{detect}) of around 13 mm. Beyond this detection range, the system cannot react to the misalignment. And, as anticipated for the aligned case, the central dark blue area signifies a minimal tracking response when the beam is correctly centred on the data PD. Importantly, this high-sensitivity ring aligns closely with the theoretically defined "tracking case" boundary ($r_{\mathrm{threshold}} < r \leq r_{\mathrm{detect}}$). The map conclusively demonstrates that the tracking PD array provides comprehensive 360° coverage around the data PD, possessing sufficient sensitivity to detect misalignment regardless of its azimuthal direction.

To quantitatively assess the static performance of the system, the FSM is programmed to introduce random angular displacements along the azimuth and elevation axis (A_{FSM} and E_{FSM}) that follow the Gaussian normal distribution with the same deviation σ_{FSM}. For each σ_{FSM}, the FSM performs 1000 iterations of the corresponding misalignments. Thus, the beam will be randomly displaced following the Rayleigh distribution on the receiver board. The control signal from the microcontroller and the SNR from the data PD (via USRP) are recorded. The SNR here is measured per-symbol by pre-detection at receiver side in each transmission. The noise power are collected without data transmitted but with optical link to build a noise floor. Then the USRP captures blocks of received data containing both signal and noise power, and calculates the empirical SNR accordingly.

Figure 5.9 presents a detailed comparison between theoretical predictions and experimental measurements of failure probability, plotted as a function of angular deviation σ_{FSM}. The

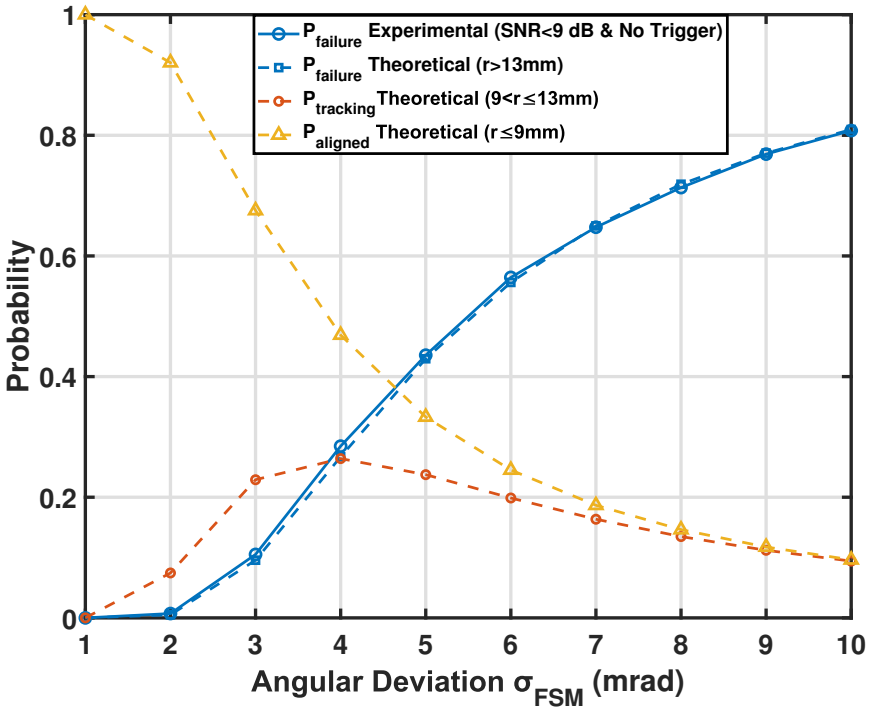

Figure 5.9: *Failure possibility in theory and experiments*

experimentally observed failure probability (solid blue line) is strictly defined as the case where the received SNR drops below the 9 dB threshold and no tracking trigger signal is generated by the microcontroller. The theoretically predicted failure probability (dashed lines) is derived from the Rayleigh displacement model in Equation 5.11, based on the criterion that the beam displacement r exceeds the defined detection range r_{detect} (13 mm). Strong agreement can be observed between the theoretical results ($r_{\text{detect}} = 13$ mm) and the experimental results from Fig. 5.8(b). Expectedly, the datasets exhibit a monotonic increase in the probability of failure with increasing angular deviation σ_{FSM}, asymptotically approaching approximately 0.8 at 10 mrad. When applying r_{detect} of 13 mm and $r_{\text{threshold}}$ of 9 mm, P_{aligned} and P_{tracking} can be derived by expression (9) and (10), shown as the dashed yellow and dashed red lines in Fig. 5.9, respectively. As the angular deviation σ_{FSM} increases, P_{aligned} (dashed yellow line) demonstrates a consistent decrease from near certainty at minimal deviations (approximately 1.0 at 1 mrad) towards a significantly lower probability (around 0.1) at 10 mrad. This illustrates the diminishing likelihood of the beam remaining within the $r_{\text{threshold}}$ for direct alignment as deviations become more pronounced. Conversely, P_{tracking} (solid red line) initially rises from a low probability at small deviations, reaching its peak likelihood (approximately 0.28) between 3 and 4 mrad of angular deviation. This peak indicates the range where the tracking

system is most frequently engaged, successfully correcting misalignments that fall within the $r_{\text{threshold}} < r \leq r_{\text{detect}}$ annulus. Beyond this peak, P_{tracking} also declines, tending towards a lower probability (around 0.1) at 10 mrad, as larger deviations increasingly result in tracking failure (P_{failure}).

5.3.4 Misalignment Path and Speed

For dynamic tracking experiments, the FSM is configured to generate a misalignment path emulating a two-dimensional ($A_{\text{FSM}}, E_{\text{FSM}}$) Gaussian random walk, with the same trajectory used for each experimental run to ensure comparability. This specific misalignment trajectory is pre-generated in MATLAB, using a fixed random seed for reproducibility, a low-pass filter for smoothing the path, and subsequently uploaded to the FSM controller. Figure 5.10 illustrates the dynamic characteristics of this FSM-induced misalignment, presenting both the spatial trajectory of the beam's displacement path and its corresponding instantaneous speed profile over time, as manifested at the receiver plane. The spatial misalignment components along the X and Y axis, introduced by the FSM, are generated following an independent Gaussian process characterised by a zero mean and a standard deviation of 1 mrad. Figure 5.10(a) displays the generated 2D displacement path of the centre of the beam relative to the receiver data PD (origin). The red circle (4 mm radius) represents the effective aperture of the data PD, while the green circle (9 mm radius) indicates the beam size at a displacement point. The displacement path is rendered as a series of discrete points due to the FSM controller's memory constraints, which inherently limits the point density of the stored trajectory. For this specific trajectory, the maximum spacing between any two consecutive displacement points is 2.2 mm. Additionally, as the distance between the FSM and the receiver board is 1.1 m and the maximum displacements are around 30 mm on the X axis and 40 mm on the Y axis at receiver board. Considering that the rotation is small, a small-angle approximation can be applied. So, it can be derived that the maximum swaying angles of the FSM considered in this work are 1.56° and 2.08° along the A_{FSM} and E_{FSM} axis, respectively. Figure 5.10(b) plots the corresponding instantaneous speed of the beam's displacement at the receiver plane, revealing that the induced misalignment speed reached a peak value of 10.8 mm/s for this particular path. This maximum speed highlights the dynamic challenge that the tracking system is designed to address during these motion evaluation tests.

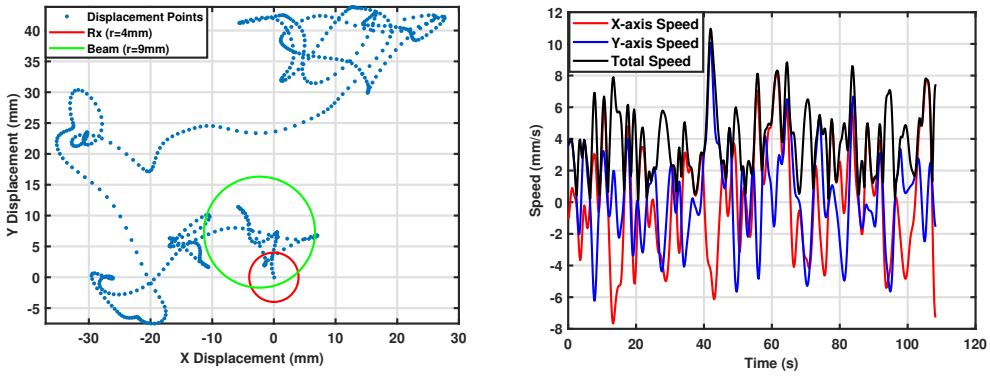

(a) *Displacement path* **(b)** *Displacement speed*

Figure 5.10: *Random misalignment at receiver generated by the fast steering mirror*

5.3.5 Tracking System Motion Evaluation

In this set of experiments, the tracking system's performance is assessed under varying maximum misalignment speeds, while maintaining the identical pre-defined random misalignment path (described in Section 5.3.4) for all speed conditions. The signal-to-noise ratio (SNR) of the received FSK-SIM symbols is continuously monitored over a 180-second period for each test, under two conditions: with the tracking system active and with it inactive (disabled). SNR data logging commenced concurrently with the initiation of the FSM-induced misalignment motion, ensuring that all measurements captured the system's performance throughout the dynamic event.

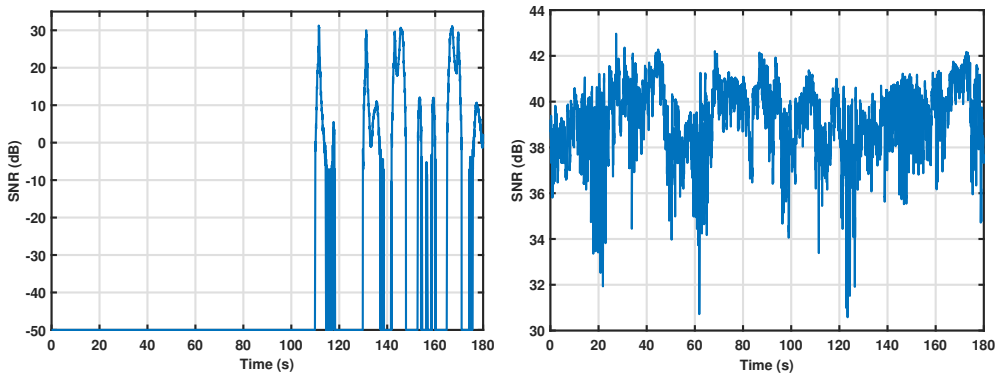

(a) *Without tracking* **(b)** *With tracking*

Figure 5.11: *Received SNR when the maximum speed is 8.8 mm/s*

When the maximum misalignment speed is set to 8.8 mm/s, the tracking system demonstrates its ability to maintain a strong SNR. Figure 5.11 presents a time-domain comparison of the

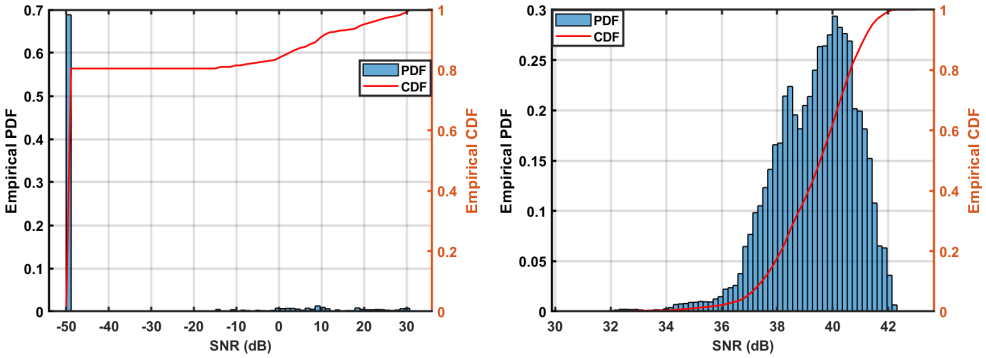

(a) *Without tracking* **(b)** *With tracking*

Figure 5.12: *Distribution of the received SNR when the maximum speed is 8.8 mm/s*

received SNR with and without the tracking system. Without tracking, the SNR trace exhibits substantial fluctuations, including extended periods of complete signal dropout (SNR at noise floor). In stark contrast, with the tracking system active, the SNR remains consistently high, showing only minor fluctuations, thereby underscoring the system's effectiveness in maintaining beam alignment at this particular speed. Figure 5.12 offers a statistical perspective on these SNR values through their probability density functions (PDFs) and cumulative distribution functions (CDFs). Without tracking, the CDF is 0.9 at the threshold SNR of 9 dB. That is, the SNR is below the 9 dB SNR threshold 90% of the time. However, with tracking, the system has zero outage probability at the same SNR threshold.

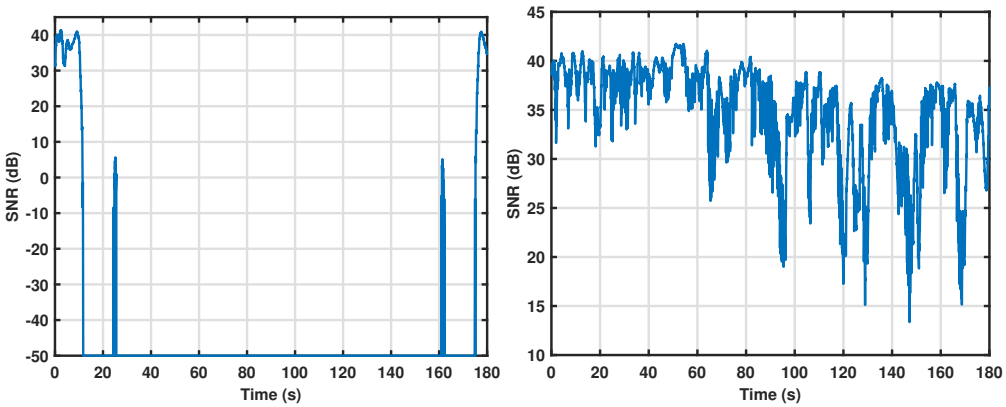

(a) *Without tracking* **(b)** *With tracking*

Figure 5.13: *Received SNR when the maximum speed is 10.8 mm/s*

Increasing the maximum misalignment speed to 10.8 mm/s further highlights the system's benefits. Figure 5.13 illustrates that without tracking, the signal is lost most of the time, with only

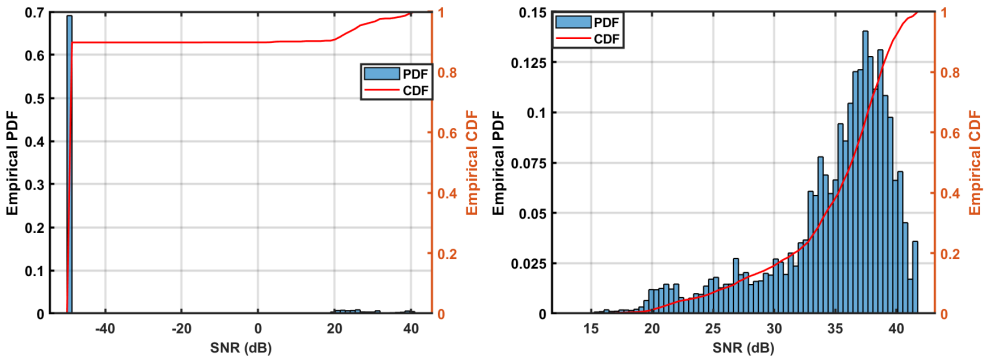

(a) *Without tracking* **(b)** *With tracking*

Figure 5.14: *Distribution of the received SNR when the maximum speed is 10.8 mm/s*

occasional connections. In contrast, with active tracking, the system maintains high SNR values throughout the 180 seconds test, showing less fluctuation, and thus demonstrating its ability to adapt efficiently to increased misalignment speed. The corresponding SNR distributions in Figure 5.14 confirm that the tracking system maintains a zero outage probability even at this 10.8 mm/s speed. In particular, while the outage probability remains zero, the variance of the 'with tracking' SNR distribution is observably larger compared to the 8.8 mm/s case. This increased variance, along with a slight decrease in the average received SNR, suggests that while the system remains fully operational and prevents outages, it encounters greater difficulty in remaining aligned as the misalignment speed increases.

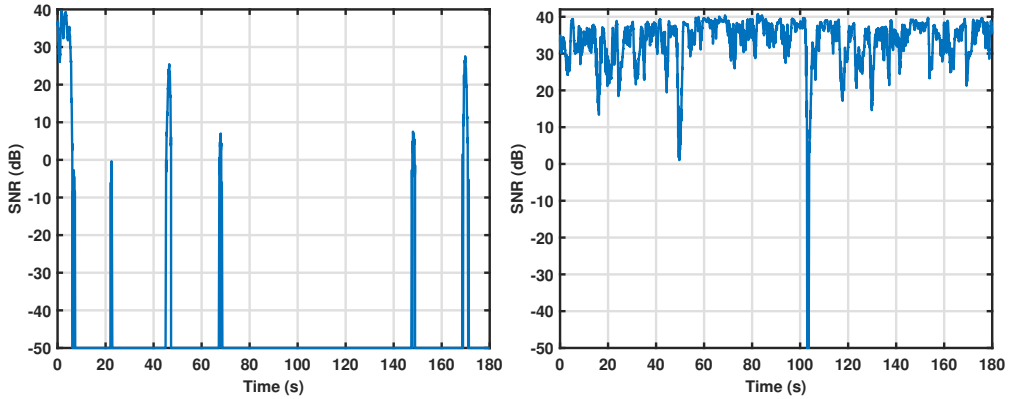

(a) *Without tracking* **(b)** *With tracking*

Figure 5.15: *Received SNR when the maximum speed is 17.4 mm/s*

A maximum misalignment speed of 17.4 mm/s appears to approach the preliminary operational limits of the current tracking system, where performance characteristics begin to no-

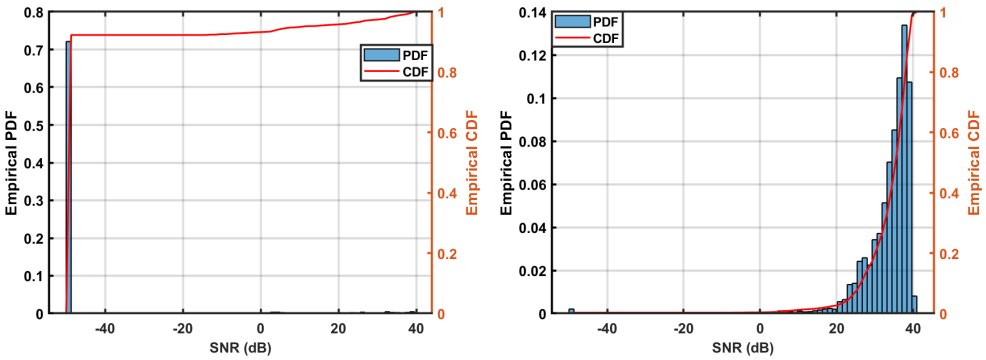

(a) *Without tracking* **(b)** *With tracking*

Figure 5.16: *Distribution of the received SNR when the maximum speed is 17.4 mm/s*

ticeably change. The SNR in Fig. 5.15 reveals that while the tracking system still provides substantial improvement over the no-tracking scenario, intermittent signal dropouts now occur. These dropouts manifest when the tracking mechanism attempts to re-acquire the beam, but momentary signal loss is experienced. This speed represents a threshold where the misalignment dynamics begin to challenge the system's capacity for complete real-time compensation. The SNR distributions in Figure 5.16 corroborate this observation. For the first time in these motion tests, a small fraction of the 'with tracking' SNR values fall below the 9 dB threshold, resulting in a non-zero outage probability of 1.1%. Furthermore, the variance of the 'with tracking' SNR increases from 2.19 to 1647.81, compared to the slower speed conditions, indicating greater fluctuations in signal quality even as the system largely maintains the communication link.

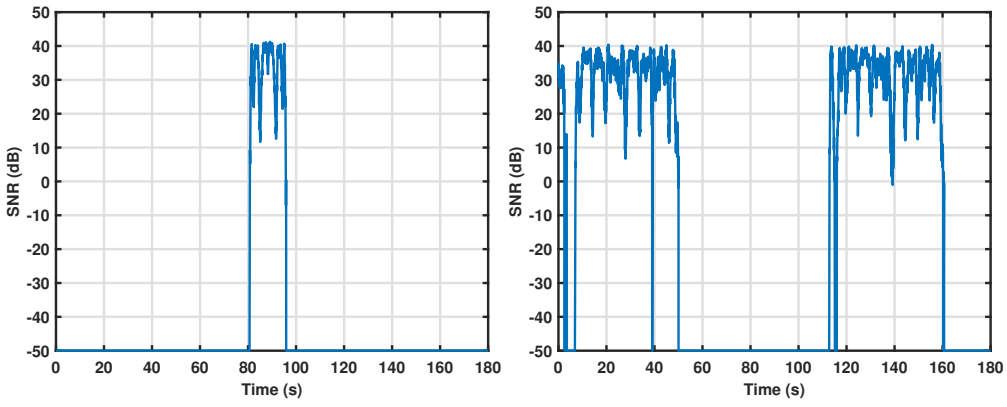

(a) *Without tracking* **(b)** *With tracking*

Figure 5.17: *Received SNR when the maximum speed is 21.4 mm/s*

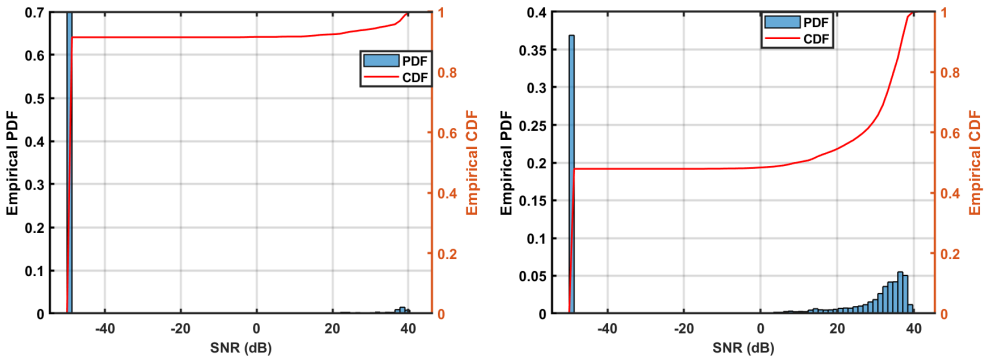

(a) *Without tracking* **(b)** *With tracking*

Figure 5.18: *Distribution of the received SNR when the maximum speed is 21.4 mm/s*

The system's performance threshold is clearly reached at the maximum tested misalignment speed of 21.4 mm/s. Figure 5.17 shows extended intervals where the tracking system is unable to maintain a stable lock on the signal, although its overall performance remains superior to the no-tracking case. During these intervals, the system appears to lose the beam's position entirely, only re-acquiring it later when relative speeds momentarily allow. This signifies a practical upper operational limit for the current system design and components. The SNR distributions in Fig. 5.18 starkly illustrate this performance degradation. The outage probability for the "with tracking" scenario increases to 0.5. Concurrently, the SNR variance is increased by more than 30-fold to the 17.4 mm/s case. These metrics indicate that the tracking system faces considerable operational stress at this speed, resulting in an unstable and unreliable communication link. In addition, the performance degradation at 21.4 mm/s represents an inherent limitation of the stepper motor system, where the mechanical response time cannot keep pace with the misalignment speed. This limitation is primarily hardware-constrained rather than algorithmic, as the NEMA 17 stepper motors and DRV8825 drivers have maximum operational speeds that are approached at this misalignment rate.

	w/o tracking				with tracking			
Misalignment max speed (mm/s)	8.8	10.8	17.4	21.4	8.8	10.8	17.4	21.4
Outage Probability ($SNR < 9\,dB$)	0.90	0.90	0.95	0.92	0.00	0.00	0.01	0.50
Variance of SNR	598.01	626.34	354.87	523.12	2.19	25.66	50.02	1647.81
Average SNR (dB)	-38.25	-41.61	-44.70	-43.10	39.35	34.80	33.55	-8.20

Table 5.3: *Summary of FSO misalignment at different speeds*

Table 5.3 summarises the systems performance (outage probability, SNR variance, average

SNR) with and without tracking, across various maximum misalignment speeds. The data shows that without tracking, the system suffers from extremely high outage probabilities (consistently exceeding 0.8), irrespective of misalignment speed. In contrast, with the tracking system active, the probability of outage is significantly lower than 1.1% for misalignment speeds of up to 17.4 mm/s, and remaining significantly lower than the no-tracking case even at 21.4 mm/s. For misalignment speeds of up to 17.4 mm/s, the tracking system provides an average SNR that is approximately 80 dB higher than the average SNR of the no-tracking system. It needs to be noted that the 80 dB SNR improvement represents the difference between complete link failure (SNR at noise floor of -50 dB) and maintained connectivity (SNR of 30-40 dB).

The tested speeds represent different misalignment conditions which is within the range of the tracking system. It is important to note that the proposed is a fine tracking system designed to operate within a fixed region. Coarse tracking mechanisms will be needed to handle large-scale misalignments beyond the operational range. Once within range, the fine tracking systems keeps the beam focused on the receiver PD.

5.3.6 Real-time Image Transmission

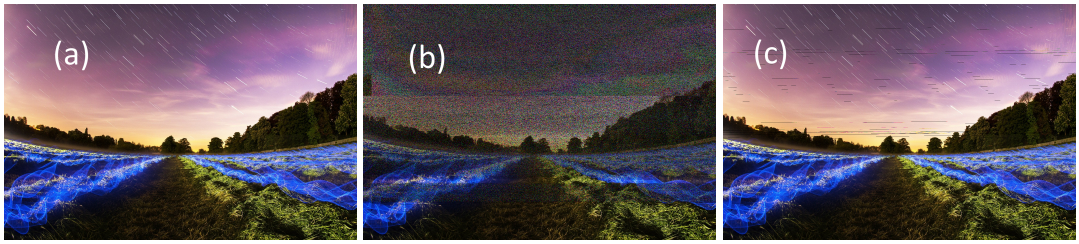

(a) *Original Image* **(b)** *Without tracking* **(c)** *With tracking*

Figure 5.19: *BMP image transmission*

To demonstrate the practical impact of the tracking system on the integrity of actual data transmission, a real-time image transmission experiment is conducted. This experiment used a maximum misalignment speed of 10.8 mm/s. The speed at the tracking system maintains a reliable and outage-free performance as shown in Section 5.3.5. Figure 5.19 presents the bitmap (BMP) image under two scenarios: with the tracking system disabled and with it enabled. The original, error-free image as in Fig. 5.19(a), depicts a clear night landscape featuring a starry sky and blue flowers in the foreground, serving as the reference for quality assessment, and the size of the picture is 7372938 bytes. When transmitted without tracking, as in Fig. 5.19(b), the received

image is severely degraded, exhibiting high noise levels and a significant loss of fine detail. This visual degradation corresponds to a measured BER of 0.305. In contrast, when the same image is transmitted with the tracking system enabled, as in Fig. 5.19(c), it retains excellent visual quality with only minimal perceptible distortion. This is characterised by a significantly lower BER of 2.29×10^{-3}. This further underscores the proposed tracking system's capability to ensure reliable communication in practical FSO applications with beam misalignment.

5.4 Summary

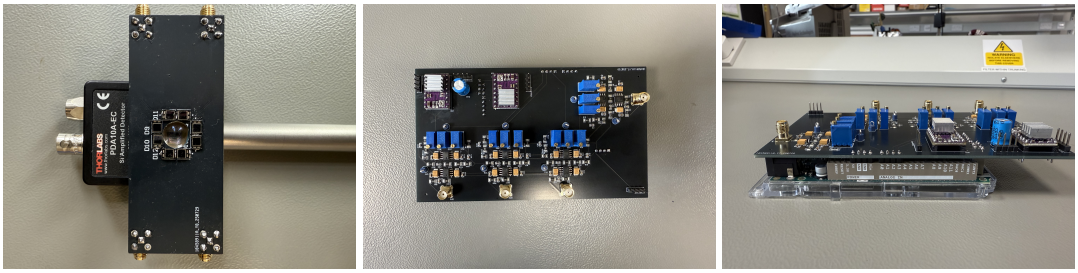

(a) *Receiver board* **(b)** *Designed shield circuit* **(c)** *Due with designed shield*

Figure 5.20: *PCB demonstration for the tracking system*

Due to the decent performance of the tracking system, the PCB board for the receiver board and shield circuit are made as shown in Fig. 5.20. The shield circuit integrates the TIA/AMP, high-pass and low-pass filter, and motor driver chips together, which allows for more practical environment testing and application. The schematic diagram and PCB design of the shield are shown in Appendix1.

This chapter presents the design, implementation, and experimental validation of an economical and robust real-time beam tracking system specifically developed for mitigating misalignment in optical wireless communication links. Static system evaluations confirmed the design's capability to accurately detect random misalignments characterised by significant standard deviations, providing the necessary input for corrective actions. Real-time experimental results demonstrated the system's effectiveness in dynamically addressing misalignment, achieving an average SNR improvement of approximately 80 dB in free-space optical scenarios. The tracking system exhibited reliable performance, maintaining minimal outage probability (1.1%) for misalignment speeds of up to 17.4 mm/s, with a degradation in performance observed at higher speeds. Furthermore, image transmission evaluations affirmed the system's practical efficacy,

with tracked transmissions achieving a BER of only 2.29×10^{-3}, a stark improvement over the 0.305 BER observed without tracking.

The tracking system was validated exclusively in free-space optical scenarios. The short-range (1.5 m) laboratory UOWC emulator used in Chapter 4 was not a suitable test environment for platform-motion tracking because the primary impairment at that scale is turbulence-induced beam wander, which is small relative to the receiver aperture and does not replicate the macroscopic platform displacements the tracking system is designed to compensate. In practical long-range UOWC deployments, such as communications between autonomous underwater vehicles, several additional factors would affect tracking performance. Scattering-induced beam broadening would reduce the spatial gradient of the received intensity profile, diminishing the sensitivity of the differential detection algorithm and potentially requiring larger photodetector array spacing. Turbulence-induced beam wander in water could introduce position errors that will cause frequent corrective actuation. Deployment would also require waterproofing of the photodetector board and actuator assembly. Extending the system to underwater operation therefore represents a direction for future work.

Chapter 6
Camera-based Adaptive Optical Wireless Communication Systems

6.1 Introduction

To make the OWC link more efficient in terms of robustness and high data rate, adaptive transmission in OWC systems requires accurate channel state information to optimise modulation parameters for varying environmental conditions. While traditional channel estimation relies on feedback channels or pilot signals, camera-based detection offers a direct visual approach to classify channel conditions. By analysing the spatial patterns of received light, cameras can identify turbulence strength in underwater channels and fog density in atmospheric links without requiring dedicated feedback mechanisms.

This chapter presents camera-based adaptive OWC systems for both underwater and free-space optical channels. For UOWC, a k-nearest neighbour (k-NN) machine learning algorithm classifies turbulence levels from captured images of backscattered light patterns. The system distinguishes between temperature-induced and bubble-induced turbulence, enabling real-time modulation adaptation. In FSO communication, Canny edge detection algorithms estimate fog intensity from camera observations to select appropriate modulation schemes. The adaptive phase-amplitude-frequency shift keying with subcarrier intensity modulation (PAFsk-SIM) modulation framework adjusts both modulation order and transmitted power based on detected channel conditions.

The key novelty of this chapter is the demonstration that a transmitter-side camera, requiring no dedicated feedback channel, can provide sufficient CSI to enable real-time adaptive modulation in both turbulent UOWC and foggy FSO links. This distinguishes the proposed approach from prior adaptive OWC systems that depend on received pilot signals or explicit return channels for channel estimation [105], making the system directly applicable to half-duplex configurations and links with no return path.

The two channel types require different estimation approaches because of their distinct physical

natures. Underwater turbulence produces spatially structured backscattering patterns in the camera images that vary systematically between still water, temperature-induced turbulence, and bubble-induced turbulence. These structured spatial differences between discrete channel states make the problem well-suited to a supervised classification algorithm such as k-NN. Fog, by contrast, does not produce discrete states but instead causes a spatially uniform, continuous reduction in image contrast and edge sharpness as density increases. This smooth, continuous relationship between fog density and edge response is better captured by a rule-based Canny edge detection algorithm than by a discrete classifier, and requires no labelled training data.

The chapter begins with the principles of camera-based channel detection in Section 6.2, covering both turbulence classification and fog intensity estimation methodologies. Section 6.3 describes the adaptive modulation schemes and their selection criteria based on camera observations. Section 6.4 presents the experimental setup and results, demonstrating performance improvements over fixed modulation schemes in varying channel conditions. Section 6.5 summarises the findings and contributions.

6.2 Principle of Camera-based Channel Detection

In this work, two example channel conditions are considered: the turbulent UOWC channel and the foggy FSO channel. This section outlines the methodology for employing camera-based channel estimation within OWC systems to estimate channel characteristics and adapt transmitted power or modulation schemes ensuring reliable communication prior to data transmission. The presented approach can be extended to other channel impairments in OWC.

6.2.1 Camera-based Underwater Turbulence Classification

In UOWC channels, the pattern backscattered light is closely associated with the type/strength of turbulence. The transmitter-side camera captures images of the optical propagation path and the backscattered photons from the channel.

The process entails using the camera to capture N images of the laser propagation path under different but known channel conditions. The channel parameters extracted from these known channel conditions are for training a machine learning classification model. This work uses each image's blue pixel value to measure the strength of backscattered photons. Due to the

presence of noise in the signal, only blue pixel value over a threshold (A_{thresh}) will be counted. For this study, seven different channel conditions are emulated in the laboratory. These are still water with no turbulence plus three levels each of turbulence created by (i) inducing temperature inhomogeneity and (ii) air bubbles along the propagation path.

The machine learning model employs the k-nearest neighbours (k-NN) algorithm, as introduced in 3.3, a robust non-parametric approach well-suited for pattern recognition and classification tasks [91]. Its performance is optimised by selecting appropriate values for the k parameter and the distance metric, tailored to the dataset's characteristics. While various machine learning techniques exist for feature extraction and classification, the k-NN algorithm (for turbulence) is chosen for this study due to its proven effectiveness, relatively low computational overhead, and suitability for real-time implementation [138].

Given the dynamic nature of the channel, rapid transitions from clear to turbulent conditions can disrupt data transmission. A channel estimation framework with a warning mechanism is implemented to address these changes, as illustrated in Figure 6.1. Initially, the differential

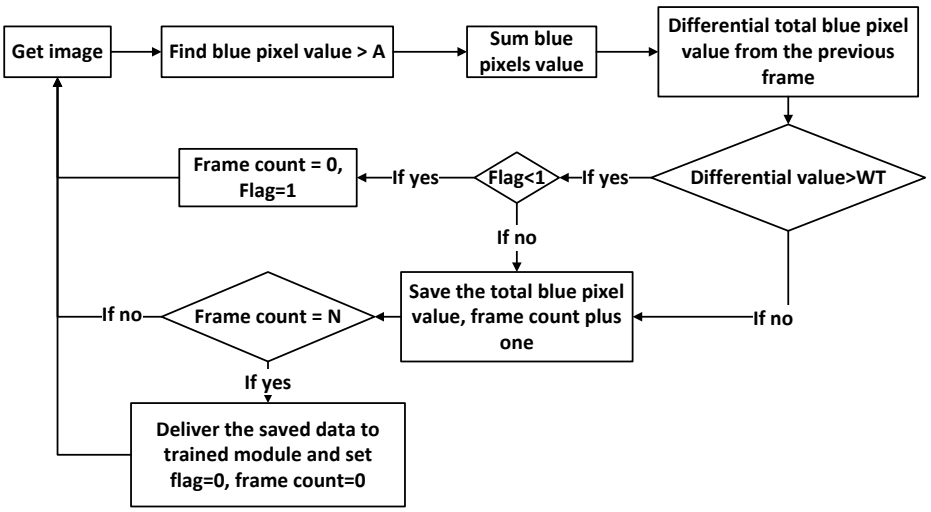

Figure 6.1: *Flowchart of the process for collecting frame data for channel prediction.*

total blue pixel value, $Flag$, and $Framecount$ are set to 0. For each captured frame, the total value of blue pixels exceeding a threshold A_{thresh} is calculated, and the absolute difference from the previous frame determines the differential value. If this value exceeds the warning threshold (WT) and $Flag$ is 0, $Flag$ is set to 1, and the $Framecount$ resets to 0. Subsequent frames are processed without resetting $Framecount$, and their data is saved. If the differen-

tial value is below WT, the total blue pixel value is saved, and $Framecount$ increments by one. Once the $Framecount$ reaches the required number (N), the collected data is fed into the trained machine learning model to predict the current channel condition. The $Flag$ and $Framecount$ are then reset. The flag mechanism ensures that data is only collected under a single channel condition, preventing mixed-condition data that could reduce prediction accuracy and increase system response time. Finally, the estimated channel condition informs the transmitter to adapt its modulation scheme for optimised performance. Information about the chosen modulation type/order is encoded using 2-FSK and appended as a preamble in the transmission data structure. At the receiver, the 2-FSK preamble is decoded to extract details of the appropriate demodulator needed to retrieve the transmitted data. It is important to note that the proposed camera-based system, with a frame capture rate of 30 frame per second (FPS) and an N-frame integration period for decision-making, is designed to adapt to changes in the general turbulence regime or average channel state, rather than compensating for the most rapid, sub-millisecond intensity fluctuations whose coherence time can be shorter than the camera's frame interval [139]. The goal is to select a modulation scheme that offers robust performance for the ongoing conditions identified in the observation window.

6.2.2 Camera-based Free-space Fog Intensity Estimation

Here, a camera-based method that adapts the transmit power dynamically in response to a varying attenuation in a foggy channel is proposed. The approach dynamically adjusts the modulation signal depth (i.e. transmit signal voltage level) in response to varying fog-induced attenuation parameters. Canny edge detection, a computer vision technique, is employed to estimate the time-varying characteristics of foggy channels through sequential mathematical operations.

To reduce noise artifacts and optimise image smoothing, Gaussian smoothing is first applied using a Gaussian filter with kernel size S_{filter} and standard deviation σ_{filter}. The Gaussian filter is defined as:

$$G_\sigma(x, y) = \frac{1}{2\pi\sigma^2} \exp\left(-\frac{x^2 + y^2}{2\sigma^2}\right). \tag{6.1}$$

The σ_{filter} determines the degree of smoothing, with larger values resulting in stronger noise reduction but increased edge blurring. The variables x and y denote spatial coordinates in the two-dimensional image plane. The filtered image, $I_{\text{smooth}}(x, y)$ is obtained through convolu-

tion:

$$I_{\text{smooth}}(x,y) = I(x,y) * G_\sigma(x,y), \tag{6.2}$$

where $I(x,y)$ is the intensity distribution of the image captured by the camera in the x,y plane and $*$ denotes the convolution operation. Gradient computation is subsequently performed using Sobel operators, S_x and S_y as follows:

$$\begin{aligned} G_x(x,y) &= I_{\text{smooth}}(x,y) * S_x, \\ G_y(x,y) &= I_{\text{smooth}}(x,y) * S_y, \end{aligned} \tag{6.3}$$

where $G_x(x,y)$ and $G_y(x,y)$ represent the horizontal and vertical gradient components respectively while Sobel kernels S_x and S_y are given by:

$$S_x = \begin{bmatrix} -1 & 0 & 1 \\ -2 & 0 & 2 \\ -1 & 0 & 1 \end{bmatrix}, \quad S_y = \begin{bmatrix} -1 & -2 & -1 \\ 0 & 0 & 0 \\ 1 & 2 & 1 \end{bmatrix}. \tag{6.4}$$

The gradient magnitude $G(x,y)$ is computed as the sum of absolute values of the directional gradients:

$$G(x,y) = |G_x| + |G_y|. \tag{6.5}$$

Non-maximum suppression is then applied to refine the edge map:

$$p(x,y) = \begin{cases} G(x,y), & \text{if } G(x,y) \text{ is a local maximum} \\ & \text{along } \theta(x,y), \\ 0, & \text{otherwise,} \end{cases} \tag{6.6}$$

where $p(x,y)$ represents the suppressed gradient magnitude, and $\theta(x,y)$ denotes the gradient direction. Finally, hysteresis thresholding is performed to classify pixels as strong edges, weak edges, or non-edges based on thresholds T_{high} and T_{low} represent the upper and lower threshold values respectively:

$$\text{Edge}(x,y) = \begin{cases} \text{strong edge}, & \text{if } p(x,y) > T_{\text{high}} \\ \text{weak edge}, & \text{if } T_{\text{low}} \le p(x,y) \le T_{\text{high}} \\ \text{no edge}, & \text{if } p(x,y) < T_{\text{low}} \end{cases}. \tag{6.7}$$

Edge pixels are assigned a value of 1, while non-edge pixels are set to 0. The estimated channel fuzziness (ECF) is calculated as the ratio of non-edge pixels to total pixels:

$$ECF = 1 - \frac{\sum Pixel_{Edge}}{Totalpixels}, \tag{6.8}$$

where $\sum Pixel_{Edge}$ represents the sum of pixels identified as edges, and $Totalpixels$ denotes the total number of pixels in the image. The resulting ECF value ranges from 0 to 1, with higher values indicating increased channel fuzziness and a higher attenuation coefficient. Based on the ECF, the transmitted power is adjusted to match the fog intensity. The simplicity and speed of this process enable real-time channel estimation and dynamic power adaptation in the system [140].

6.3 Experimental Setup and Channel Characterisation

This section describes the experimental setup, the generation of turbulence and fog conditions, and the performance evaluation of the proposed detection methods.

6.3.1 Experimental Setup

Figure 6.2 shows the block diagram of the experimental setup used in this study, which includes the OWC channel emulator. The OWC channel emulator consists of a tank with dimensions $1.5 \times 0.5 \times 0.5$ m^3. For UOWC tests, the tank is filled with 210 litres of clear tap water, while it is emptied and filled with artificial fog for free-space channel tests.

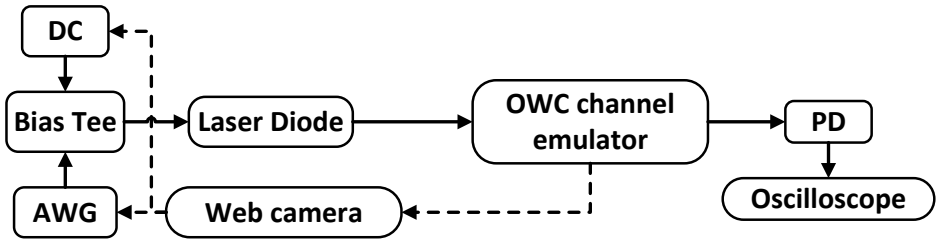

Figure 6.2: *The system block diagram of the experimental setup, including the laser diode; arbitrary waveform generator (AWG); Direct Current (DC); Photodiode (PD)*

A camera (eMeet C960 webcam), co-located with the transmitter, is used to estimate the chan-

nel conditions and dynamically adjust the transmitted power or modulation scheme. The eMeet C960 is selected for its 30 FPS frame rate, which is sufficient to track turbulence variations whose coherence timescales are on the order of hundreds of milliseconds [139], and for its compact form factor and low cost, consistent with the practical deployment goals of this chapter. The eMeet C960 webcam at 480p resolution is chosen for its low cost and sufficient spatial resolution for the working distances used in this experiment, where both the backscattering patterns from underwater turbulence and the edge features of the FSO channel are resolvable. For longer link distances where finer spatial detail would be required, a higher-resolution camera could be adopted as a straightforward upgrade within the same estimation framework. The data is generated using a MATLAB-controlled Keysight M8195A AWG. A bias-tee combines the electrical signal with a DC bias to ensure the transmitted signal remains unipolar; 40 mA was found optimal to keep the laser in its linear operating range. The combined signal drives an Osram PL450B LD. As in Chapter 4, the Osram PL450B is chosen because its 450 nm emission falls within the blue-green transmission window of seawater where absorption is minimised [5]. The optical signal propagates through the channel emulator where conditions are adjusted to simulate specific scenarios. Adjacent to the laser diode, a web camera captures a 480p (640×480) video stream at 30 FPS, providing real-time monitoring of channel conditions. At the receiver, the optical signal is detected by a PIN photodiode with an integrated transimpedance amplifier (TIA). The photodiode's 1 GHz bandwidth, which matches the selection criterion used in Chapter 4, is sufficient to resolve all symbol rates evaluated here. The output is sampled by a Keysight DSA90804A oscilloscope and processed offline in MATLAB.

6.3.2 Turbulence Generation, Detection, and Classification in Underwater Channel

This study examines two types of turbulence: temperature-induced and bubble-induced. Still water with $\sigma_I^2 \approx 0$ serves as the baseline. Temperature-induced turbulence is generated by imposing a temperature gradient within a water-filled tank using a heater, as described in 4.4.1. Three turbulence levels are analysed: Tem1 ($\sigma_I^2 \approx 0.10$), Tem2 ($\sigma_I^2 \approx 0.18$), and Tem3 ($\sigma_I^2 \approx 0.36$). Bubble-induced turbulence is achieved with an air pump distributing 15.0 L/min through four ports. A pipe divider adjusts the flow to half, three quarters and one, producing bubbles at rates of 1.875 /min (Bub1), 2.813 L/min (Bub2) and 3.75 L/min (Bub3), resulting in turbulence with $\sigma_I^2 \approx 0.10$; $\sigma_I^2 \approx 0.20$; $\sigma_I^2 \approx 0.56$, respectively. The stochastic nature of the turbulence introduces fluctuations of approximately ± 0.03 in σ_I^2 during the experiment. All

tested conditions fall under the weak turbulence regime characterised by $\sigma_I^2 < 1$.

The classifier determines the channel type among the seven conditions based on the algorithm outlined in Fig. 6.1 and a demonstration of the process for bubble classification is shown in Fig. 6.3.

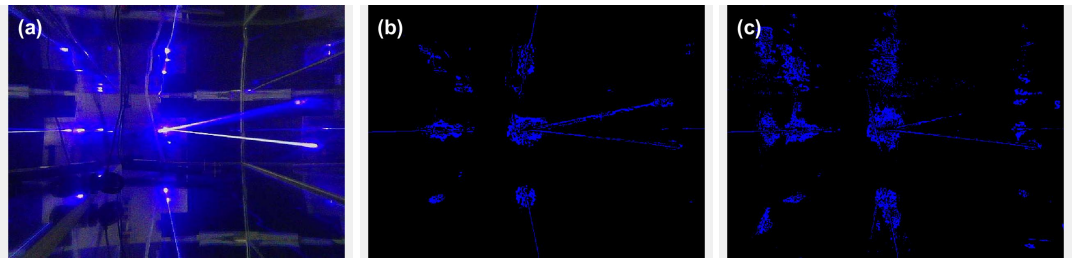

Figure 6.3: *Blue Channel extraction and processing ($A = 250$): (a) original image in still water; (b) processed image in clean water; (c) processed image in bubble-induced turbulent water*

After pretesting the system with the algorithm, the relative parameters are configured with threshold (A) = 250 and frame count (N) = 210. The learning process is based on 7,000 samples per channel condition, with 70% assigned for training and 30% randomly for testing. The performance of the classifier on 14,700 test samples is shown in Fig. 6.4. In the confusion matrix, the rows correspond to the true class and the columns correspond to the predicted class. The diagonal cells correspond to channel conditions that are correctly classified. The off-diagonal cells correspond to incorrectly classified channel conditions. The confusion matrix shows that when predicting channel as Tem3 for example, there are 50 incorrect predications as Tem2, which means there is an inaccuracy of 2.4%. Nevertheless, the figure still reveals an overall approximate accuracy 99% in classifying turbulent UOWC channels, allowing for precise channel estimation for the transmitter.

6.3.3 Fog Generation and Intensity Estimation in Free-space Channel

An optical wireless channel with fog is generated using the Rage 600I smoke machine from beamZ, which has an output capacity of 65 m^3/min. The smoke machine outlet is positioned at one end of the enclosed $1.5 \times 0.5 \times 0.5$ m^3 FSO channel enclosure, directed along the optical propagation axis. Each button press activates the machine for approximately 2 s, injecting

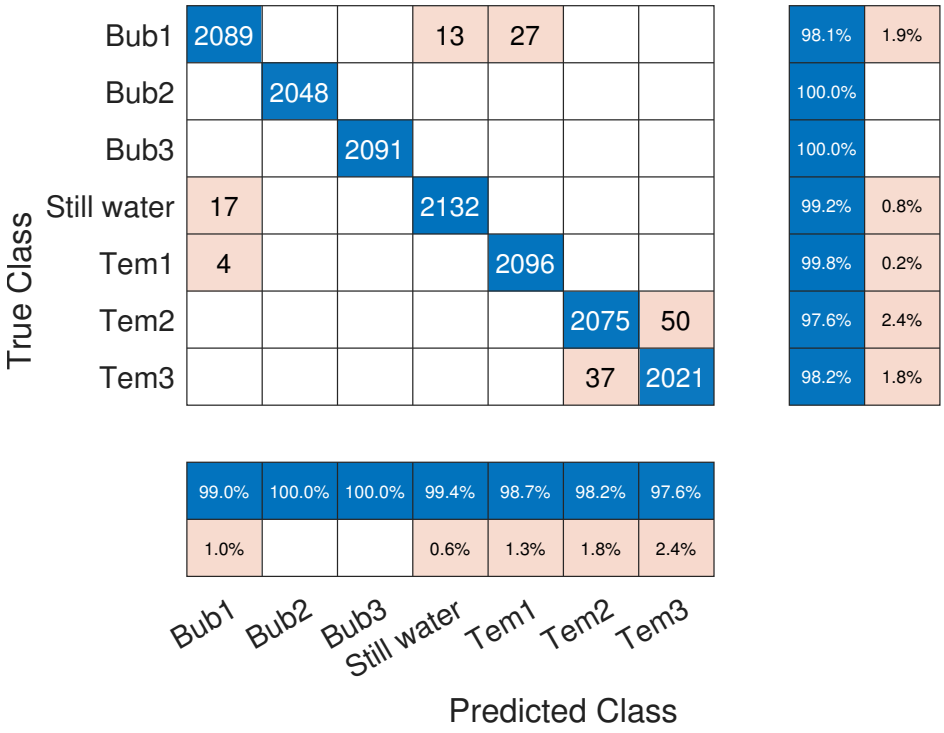

Figure 6.4: *k-NN confusion matrix*

a controlled burst of fog-like aerosol into the enclosure. An air pump mounted inside the enclosure circulates the aerosol to achieve a nominally uniform distribution across the 1.5 m propagation path. Following each injection, the fog gradually dissipates over approximately 60–90 s as the air pump continues to circulate air, allowing the channel to return to a clear state. This single-injection procedure creates a continuous progression of channel conditions within one experimental run: an initial clear state, a rapid transition to peak attenuation, followed by a gradual recovery. The received peak-to-peak voltage (V_{pp}) measured at the photodiode output is used as the continuous fog intensity metric throughout this progression, as it directly and monotonically reflects the optical attenuation introduced by the aerosol.

For the experimental setup described, the Canny edge detection parameters were empirically determined through pretesting under various conditions to be: Gaussian filter kernel size $S_{\text{filter}} = (3, 3)$, standard deviation $\sigma_{\text{filter}} = 0.8$, and hysteresis thresholds $T_{\text{high}} = 200$ and $T_{\text{low}} = 90$. It is acknowledged that these parameters may require optimization for different operational environments, camera hardware, or target distances to ensure robust performance. The transmitter continuously generates a 500 MHz sine wave with a peak-to-peak voltage of 400 mV. The experiments are carried out under natural light conditions, with an optical power of 0.13 μW

measured at the location of the webcam. The procedure involves capturing images of the distant receiver and recording the received peak-to-peak voltage. The pictures captured by the web camera and the detected edge pixels are shown in Fig. 6.5 within three different foggy conditions, which are no fog, light fog and thick fog. The received V_{pp}, edge count, and estimated

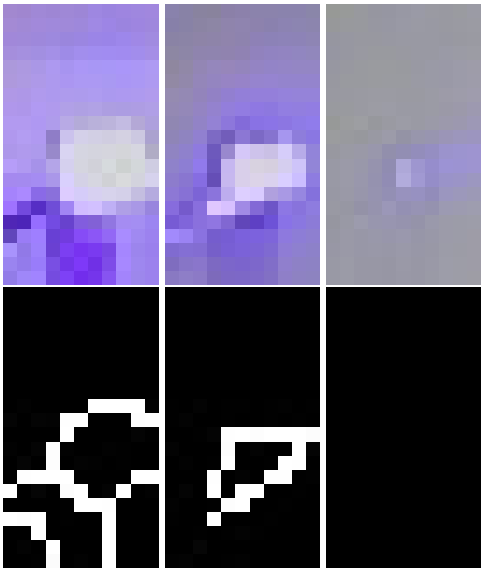

(a) *no fog* **(b)** *light fog* **(c)** *thick fog*

Figure 6.5: *Photos of receiver in different fog conditions and the corresponding edge results*

channel fuzziness are illustrated in Table 6.1. The table shows distinct variations in edge detection metrics under different foggy conditions. In the absence of fog, an edge count of 34 was observed, corresponding to a V_{pp} of approximately 190 mV. Conversely, under thick fog conditions, the edge count decreased significantly to 0, with a corresponding V_{pp} of 50 mV. Despite clear atmospheric conditions, the edge count of 34 yielded a relatively high estimated channel fuzziness of 0.83. This elevated fuzziness value can be attributed to the total pixel count in the receiver image, which is fundamentally dependent on both the camera specifications and the camera-to-receiver distance. Furthermore, the experimental results demonstrate a positive correlation between fog intensity and estimated channel fuzziness, suggesting that increased atmospheric opacity leads to higher channel uncertainty.

To determine if ambient light changes impact detection results, the system was tested under four different conditions with and without artificial ambient light. The optical power measured at the web camera position was 0.13 μW and 14 μW for environments with and without artificial light, respectively. Figure 6.6 and Table 6.2 present the ECF values in various scenarios and

Fog intensity	Received V_{pp} (mV)	Edge count	ECF
(a) No fog	190	34	0.83
(b) Light fog	112	21	0.90
(c) Thick fog	50	0	1

Table 6.1: *Measured free-space channel characterisation with and without fog*

the corresponding statistical data. In conditions of light fog (with received V_{pp} around 190 mV and 150 mV), the estimated channel fuzziness is higher in the absence of artificial illumination compared to when the light is present. This occurs because brighter ambient light provides the web camera with more image details for edge recognition. However, the disparity in estimated channel fuzziness between the two lighting conditions decreases from 0.03 to 0 as the fog density increases. Therefore, the maximum difference in estimated channel fuzziness due to artificial ambient light in this study is 0.03, indicating that the proposed system is marginally influenced by changes in ambient light.

Received V_{pp} (mV)	Artificial light	ECF	Variance
190	yes	0.80	4.13×10^{-5}
190	no	0.83	2.93×10^{-5}
150	yes	0.93	2.93×10^{-5}
150	no	0.94	2.48×10^{-5}
100	yes	0.97	8.83×10^{-6}
100	no	0.97	2.49×10^{-5}
60	yes	0.99	3.00×10^{-6}
60	no	0.99	1.63×10^{-5}

Table 6.2: *Ambient light test results showing ECF and Variance.*

6.4 Data Transmission Results

This section provides a detailed analysis of the experimental results conducted in turbulence-induced UOWC and fog-induced attenuated channels, emphasising the integration of channel estimation techniques with data transmission. In this section, the reference point for BER is set as 3×10^{-3}, and the total number of transmitted bits are over 480000 for each set of experiment.

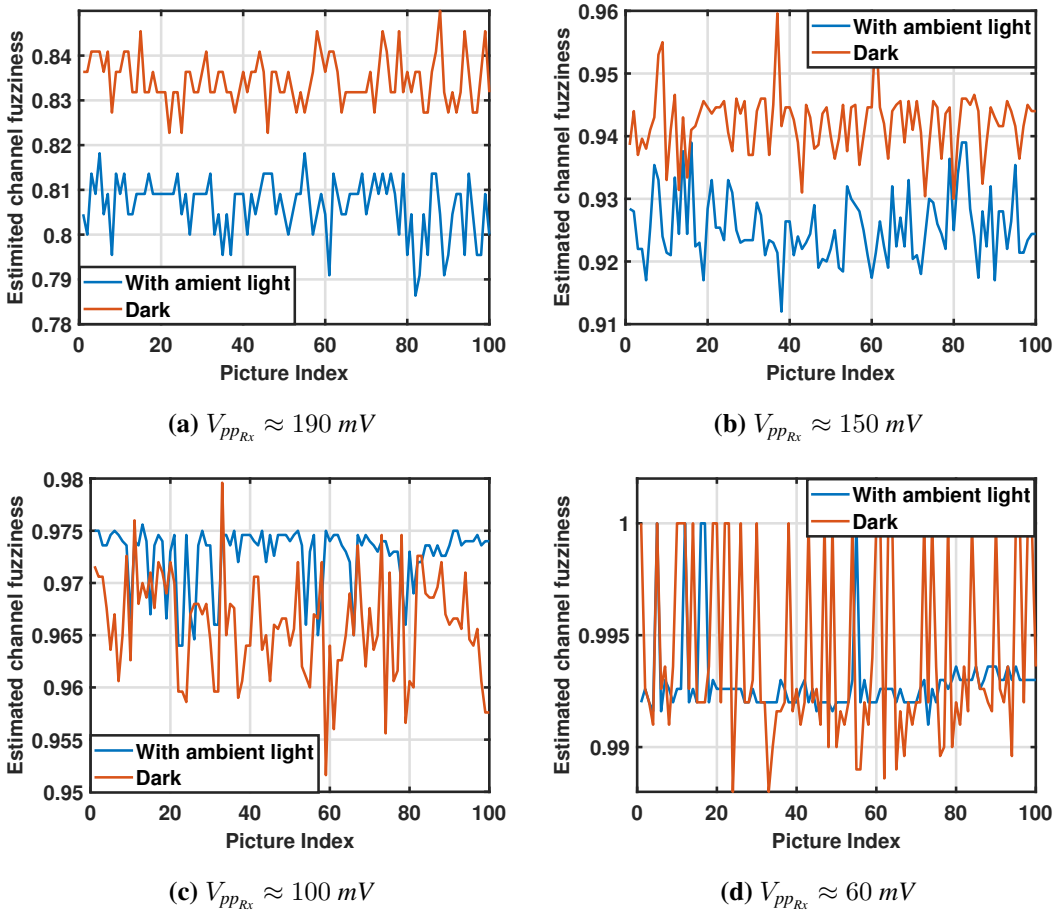

(a) $V_{pp_{Rx}} \approx 190\ mV$ **(b)** $V_{pp_{Rx}} \approx 150\ mV$

(c) $V_{pp_{Rx}} \approx 100\ mV$ **(d)** $V_{pp_{Rx}} \approx 60\ mV$

Figure 6.6: *ECF with different received V_{pp} corresponding to different fog intensity under varying ambient light conditions*

6.4.1 Performance in Underwater Optical Channel

The transmitter encodes the data according to PAFsk-SIM adaptively based on the channel estimation. The PAFsk-SIM technique offers flexibility and robustness, enhancing spectral efficiency by layering modulation dimensions [67]. This hierarchical approach achieves maximum spectral efficiency by encoding data on the three dimensions of the subcarrier signal (i.e. frequency, phase and amplitude). The resulting overall modulation order $M = M_f M_p M_a = M_f M_{pa}$, where M_f represents the FSK modulation order, M_p the phase modulation order, M_a the amplitude modulation order, and M_{pa} the combined QAM modulation order. The choice of PAFsk-SIM is predicated on its flexibility in adapting to channel conditions. While simpler schemes like On-Off Keying (OOK) or Binary Phase Shift Keying (BPSK) exist, OOK has been shown to be less robust in dynamic channels [6], and BPSK, while resilient, offers lower spectral efficiency than the higher-order phase and amplitude modulations achievable with PAFsk-SIM when channel conditions permit. The adaptive approach allows the system to leverage the robustness of frequency/phase modulation when needed, akin to the resilience of BPSK/FSK, while also capitalising on higher spectral efficiency through amplitude/phase modulation in benign conditions.

To achieve a robust UOWC link, based on the estimation from the camera, data will only be encoded onto subcarrier signal amplitude in still water to achieve the highest data rate, while frequency and phase dimensions are used in turbulent water conditions to make the UOWC link more resilient. In this experiment, $M_f = 1, M_{pa} = 16$; $M_f = 2, M_p = 4, M_a = 1$; $M_f = 2, M_p = 8, M_a = 1$ from PAFsk-SIM are chosen as potential modulation schemes to choose from depending on the channel condition.

Figure 6.7 demonstrates the adaptive response of the system to channel fluctuations by dynamically adjusting the modulation schemes based on camera-based channel estimation. Initially, the underwater channel is characterised by still water, the SNR remains stable at 21 dB, allowing the system to sustain a data rate of 4.2 Gbps with 16-QAM. This is followed by bubble-induced turbulence, between the 100 s mark (labelled point A) and the 250 s mark (labelled point B), the system employs the $M_f = 2, M_p = 8, M_a = 1$ modulation scheme, achieving a data rate of 3.58 Gbps. Following point B, the channel reverts to still water conditions until it reaches the 350 second mark (point C), during this time, 16-QAM is chosen again based on the estimated channel and the data rate is 4.2 Gbps. The heater is activated from point C (350 seconds) to point D (500 seconds), the $M_f = 2, M_p = 4, M_a = 1$ scheme is selected, providing

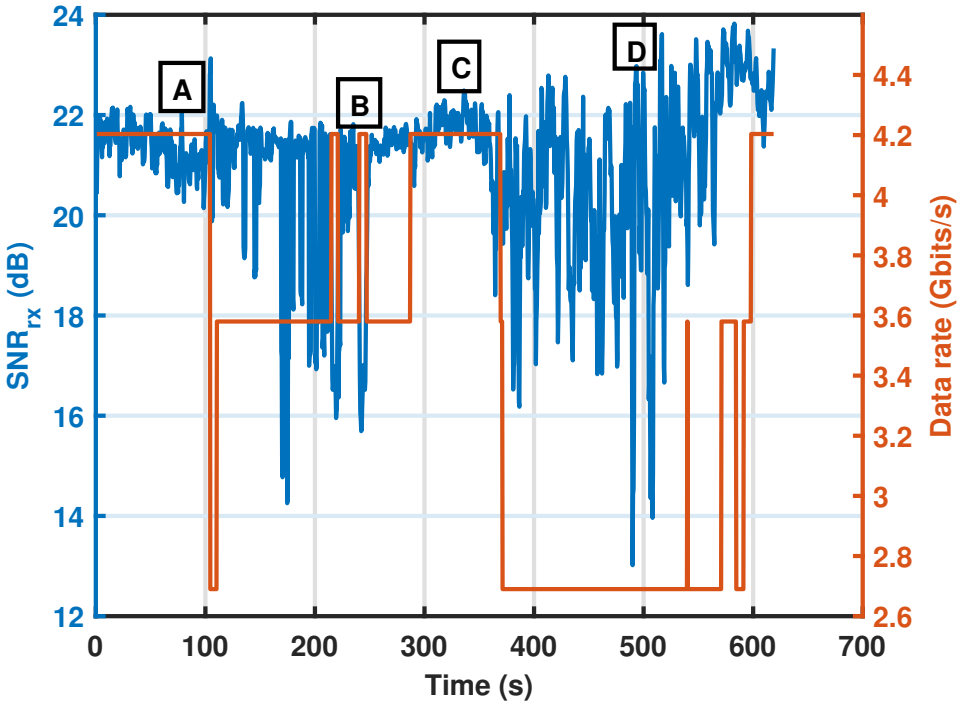

Figure 6.7: *Performance of the proposed adaptive scheme under still water, bubble-induced turbulence (A–B), and temperature-induced turbulence (C–D) UOWC channel*

Modulation schemes	Total BER	FSK BER	Data rate (Gbps)
$M_f = 1, M_{pa} = 16$	0.01	Zero	4.20
$M_f = 2, M_p = 4, M_a = 1$	0.0015	0.0013	2.69
$M_f = 2, M_p = 8, M_a = 1$	0.0036	0.0013	3.58
Adaptive PAFsk-SIM	0.0029	0.0027	3.51

Table 6.3: *Experimental results for different modulation schemes in the varying channel*

a data rate of 2.69 Gbps. Due to the inherent heating and cooling time of the heater, noticeable effects on the intensity of the received signal begin after point C and persist slightly beyond point D.

Table 6.3 demonstrates the advantages of the adaptive modulation scheme. Four sets of experiments with the same pattern of the varying channel shown in Fig. 6.7 are compared. Three sets use the single modulation scheme during the varying channel, and one set uses the proposed adaptive modulation method. The total BER indicates the error rate of all transmitted bits and the FSK BER refers to the BER of the bits encoded on frequency dimension of the subcarrier signal only. $M_f = 1, M_{pa} = 16$ and $M_f = 2, M_{pa} = 8$ have relatively higher data rate, but the BER is up to 0.01 and 3.6×10^{-3} which are higher than the BER reference, while $M_f = 2, M_{pa} = 4$ has lower data rate but a low BER. Overall, the adaptive PAFsk-SIM approach effectively balances performance and reliability, yielding an average data rate of 3.51 Gbps and a BER of 2.9×10^{-3}, demonstrating its capability to maintain robust communication under varying channel conditions. In addition, it can also be noted that in this varying channel condition, the preamble FSK symbols accurately convey the details of the modulation type/order to the receiver due to FSK's robustness.

6.4.2 Performance in Free-space optical Channel

This free-space optical channel experiment aims to adjust the transmitted electrical signal V_{pp} based on measured channel characteristics to maintain stable communication using $M_f = 1, M_{pa} = 16$ at a data rate of 4.20 Gbps. For this setup, achieving a reliable link at the BER reference point requires a minimum V_{pp} of 260 mV, resulting in a minimum electrical SNR of 14 dB. Below this value, the link breaks down. Taking into account the system response time between varying conditions, a BER lower than the reference BER is maintained in the initial

channel with a transmitted V_{pp} of 400 mV.

To evaluate the adaptive system, fog is introduced in the free-space channel. Figure 6.8 illustrates the temporal evolution of the free-space fog channel through SNR measurements and corresponding estimated channel fuzziness values. Fog was introduced at four distinct times:

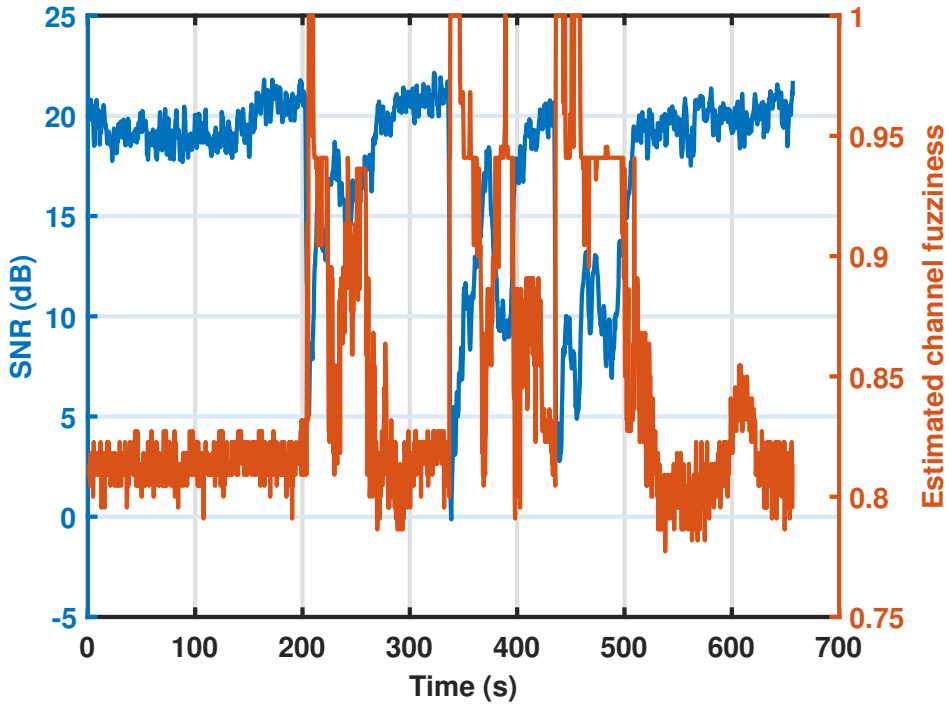

Figure 6.8: *Received SNR and estimated channel fuzziness*

200 s, 330 s, 380 s, and 460 s. In clear conditions, the channel is clear and the system can maintain an SNR of approximately 20 dB. As fog density increased, a significant inverse correlation emerged between SNR and channel fuzziness, with SNR declining rapidly during fog introduction and recovering gradually during fog dissipation, inversely tracking the channel fuzziness values. Figure 6.9 plots the received SNR against estimated channel fuzziness, fitted with a quadratic curve. In the figure, region A is the received SNR area which the system wants to maintain to get a low BER; region B is the area where the received SNR can meet the SNR requirement by adjusting the transmit signal V_{pp}; region C is the limitation in this work, the received SNR will not be able to get up to 14 dB due to the available maximum power of the transmitter.

The relationship demonstrates a declining SNR trend as fuzziness increases, described by (6.9),

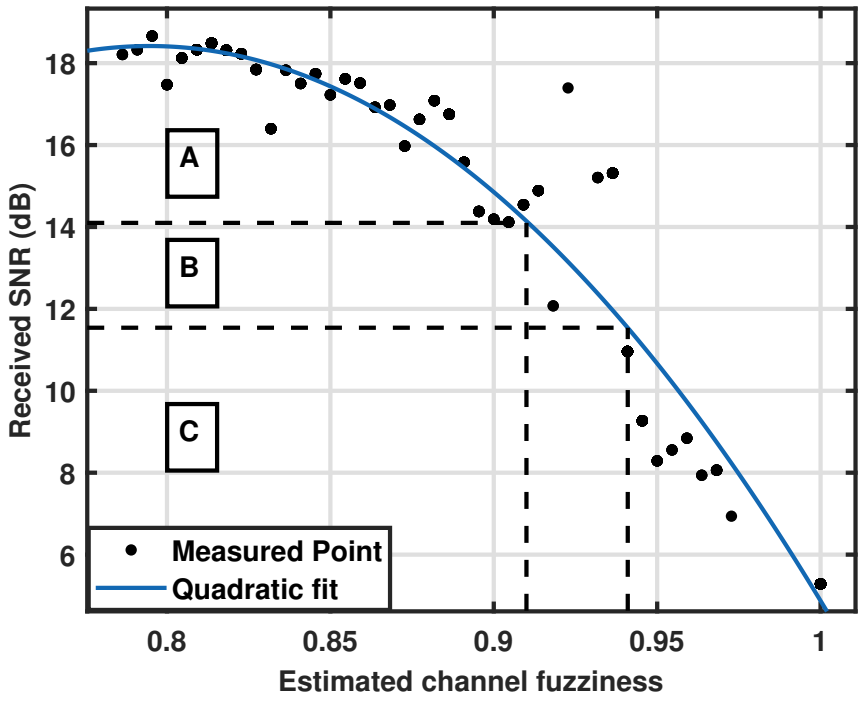

Figure 6.9: *Received SNR against the estimated channel fuzziness with quadratic fitting curve*

where f is the estimated channel fuzziness and $\mathrm{SNR}_{\mathrm{rx}}$ is the received SNR in dB.

$$\mathrm{SNR}_{\mathrm{rx}}(f) = -353.5f^2 + 571.8f - 213.5. \tag{6.9}$$

The transmitter estimates the received SNR using the fitting curve from Fig. 6.9, which is based on channel predictions from the web camera. To maintain the SNR requirements (14 dB), the transmitter adjusts the V_{pp} of the transmitted signal. The required gain to amplify the signal is so that the system can maintain below the reference error rate is determined by:

$$\mathrm{Gain}(f) = \begin{cases} 18.1 - \mathrm{SNR}_{\mathrm{rx}} & \text{for } f \leq 0.94 \\ 2.3 & \text{for } f > 0.94. \end{cases} \tag{6.10}$$

Data transmission was conducted to evaluate the proposed system under dynamic fog conditions. The performance with constant transmitting power without fog is used as a benchmark. The performance of adaptive transmitting power was compared with constant transmitting power under varying fog conditions. As shown in Fig. 6.10, the fog machine was activated

Channel conditions	SNR (A)	SNR (B)	SNR (C)
No fog	19.7	20.5	20.8
Varying fog without adaptive power	15.3	10.8	9.9
Varying fog with adaptive power	18.9	13.6	13.8

Table 6.4: *SNR comparison among different channel conditions*

at 200 s, 340 s, and 430 s. In the clear conditions (no fog), the received SNR was around 20 dB,

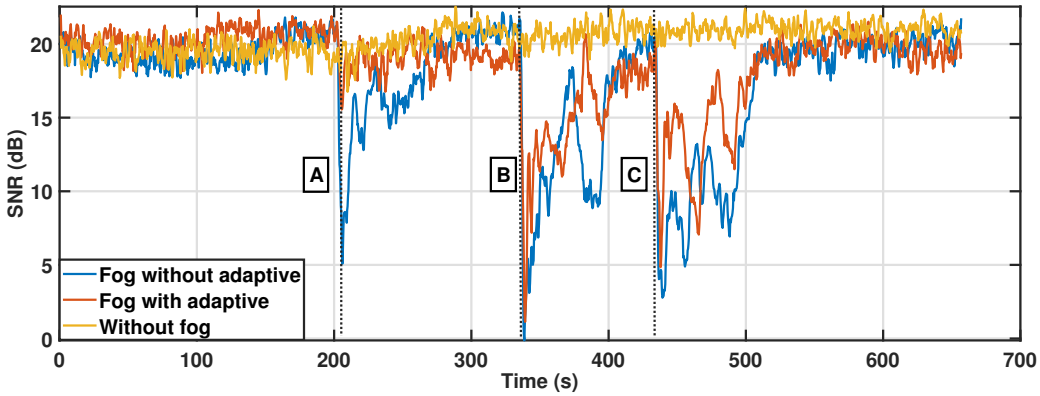

Figure 6.10: *SNR curve in frame transmission*

but it decreased with the introduction of fog for both constant and adaptive V_{pp} transmissions. However, the adaptive V_{pp} transmission maintained relatively stable SNR, particularly when fog was added at 200 seconds. Additionally, the adaptive method led to faster SNR recovery compared to constant V_{pp} transmission, even in dense fog conditions at 340 s and 430 s. Table 6.4 shows the average SNR after fog releasing (points A, B, and C) until the SNR is stable before the next point. The table indicates that the proposed adaptive system achieves an increase in SNR of around 3 dB over constant transmission power.

However, the SNR of fog with adaptive and without adaptive are similar after giving fog at point B and C. This can be attributed to the received optical signal power being below the noise level because of the dense fog. In addition, the corresponding BER values were 3.97×10^{-4} for constant transmitting power with no fog, 0.01 for constant transmitting power with varying fog, and 3.0×10^{-3} for adaptive transmitting power with varying fog. These results demonstrate that the proposed system ensures a more stable OWC link in varying fog conditions.

When considering the application to practical and long-distance environments, such as 1 km

outdoor links, the fundamental process described in this paper would be maintained. However, it is crucial to note that the proposed system is not designed for static operation post-deployment without recalibration. Instead, it incorporates a strategy for periodic channel re-evaluation. This process involves retraining the underlying estimation models (e.g., k-NN for UOWC) by leveraging data from co-located sensors at the receiver (e.g., photodiodes monitoring SNR, or other environmental detectors). Such retraining would occur when a significant alteration in channel characteristics is detected, or at predetermined intervals (e.g., hourly). This adaptive mechanism enables the system to update its operational dataset and dynamically adjust its parameters, thereby ensuring robust performance as real-world conditions evolve. This operational approach is also key to the broader generalisation capabilities discussed for future research.

6.5 Summary

The proposed camera-based channel estimation system for the OWC uses k-NN and image processing techniques to estimate the OWC channel and adapt the modulation schemes or transmitted power accordingly. The adaptive PAFsk-SIM framework successfully demonstrated real-time modulation adaptation based on camera-detected channel conditions, achieving optimal balance between data rate and reliability without requiring feedback channels in varying hostile channel conditions. The lab experiments in turbulence resulted in an average data rate of 3.51 Gbps at no higher that 2.9×10^{-3} BER throughout the transmission. In foggy channel conditions, the experiment resulted in a data rate of 4.2 Gbps at 3.0×10^{-3} for the entire transmission period. Thus, it can be concluded that the proposed system enhances the OWC link robustness with a low-cost webcam-based channel estimation. Additionally, camera with higher FPS will potentially reduce sensing time to increase the system's sensitivity against channel varying, which can be discovered in the future work. The selection of turbulence as the primary UOWC impairment and fog as the primary FSO impairment was motivated by both practical relevance and laboratory controllability. Temperature and bubble-induced turbulence are the dominant channel impairments in UOWC that cannot be fully mitigated by increasing transmitted power, making adaptive modulation the appropriate response. Fog is the severe and dynamically variable attenuation impairment in short-range FSO deployments, with gradual temporal evolution well-suited to camera-based monitoring. Both impairments are controllably reproducible in the laboratory channel emulator, enabling systematic experimental characterisation.

Future research will also focus on validating the system's generalisation capabilities in diverse real-world underwater and atmospheric environments, including scenarios with varying salinity gradients, complex multipath scattering, and dynamic ambient lighting conditions. This will involve field trials and the development of robust online learning or model adaptation mechanisms to ensure sustained performance when encountering conditions not present in the initial training dataset. Such investigations will also address the system's applicability to longer communication links.

Chapter 7
Retroreflector-based CSI Estimation for Adaptive Optical Wireless Communication

7.1 Introduction

Accurate CSI is essential for adaptive optical wireless communication systems to optimise transmission parameters. In Chapter 6, we demonstrated a camera-based approach for CSI estimation that uses machine learning algorithms to classify channel conditions from captured images of backscattered light patterns. While effective, the camera-based method requires image processing hardware and computational resources for k-nearest neighbour (k-NN) classification, with estimation times limited by camera frame rates (typically 30 FPS).

This chapter presents a complementary CSI estimation architecture using retroreflector-based polarisation transformations to achieve transmitter-side channel monitoring. Similar to the camera-based approach in Chapter 6, this method eliminates the need for dedicated feedback channels. However, instead of visual pattern recognition, it exploits the deterministic polarisation changes induced by corner cube retroreflectors to extract CSI directly from the optical signal.

The proposed system uses the same adaptive PAFsk-SIM modulation framework as Chapter 6, but obtains CSI through a different physical mechanism. A beam splitter (BS) separates the retroreflected signal for channel monitoring while maintaining the primary communication link. The retroreflector's alignment-preserving property ensures that the monitored signal accurately represents the channel conditions affecting data transmission. This approach offers faster response times compared to the camera-based method, as it is not limited by frame capture rates. The system adapts three-dimensional hierarchical PAFsk-SIM modulation schemes based on SI measurements from the transmitter-side APD.

This chapter details the retroreflector-based CSI estimation system design and experimental validation in both turbulent underwater and foggy atmospheric channels. Section 7.2 presents

the polarisation transformation theory and retroreflector properties. Section 7.3 describes the experimental setup including the optical architecture and signal processing subsystems. Section 7.4 provides channel characterisation methodology, comparing sliding window and block-based SI estimation approaches. Section 7.5 demonstrates adaptive modulation performance, achieving 9% throughput improvement in turbulent underwater channels and 15% in foggy FSO links compared to fixed modulation schemes. Section 7.6 summarises the key findings.

7.2 Polarisation State along FSO Channel and Retroreflector

The polarisation state evolution of optical signals propagating through underwater channels has been introduced in Chapter 4, where experimental results demonstrated that polarisation states are broadly maintained over short-distance UOWC links, enabling successful PDM implementation with negligible cross-polarisation interference. However, the transition from underwater to FSO channels introduces additional polarisation considerations.

In FSO channels, atmospheric effects on polarisation are more pronounced than in UOWC. Although underwater channels preserve polarisation states due to predominantly small-angle scattering [122], FSO channels experience three distinct mechanisms that affect polarisation. First, atmospheric turbulence induces random polarisation fluctuations through differential phase shifts between orthogonal components, creating time-varying polarisation states [141]. Second, aerosol and molecular scattering can cause partial depolarisation, particularly during adverse weather conditions. Third, when these altered polarisation states encounter polarisation-sensitive components such as polarising BSs, the resulting polarisation-dependent losses (PDL) can cause significant power variations [142]. Studies have shown that while forward scattering at small angles (less than ten°) generally preserves polarisation [143], the cumulative effect of atmospheric turbulence over longer FSO paths can degrade polarisation purity more severely than in the relatively stable underwater environment. However, when the beam size increases, the effect of FSO to the polarisation state of the optical beam will be limited, probe and signal optical beam with different polarisation states are coordinated to recover the signal beam mode under FSO turbulence effect [144, 145].

While Chapter 6's camera-based approach captures spatial patterns of turbulence through backscattered light imaging, the retroreflector-based method measures the integrated effect of channel impairments on the retroreflected signal. Both approaches aim to classify similar channel

conditions—still water, temperature-induced turbulence, and bubble-induced turbulence—but through different detection mechanisms. The camera method provides visual classification with 99% accuracy after processing 210 frames, whereas the retroreflector approach offers continuous scintillation index measurements with convergence after approximately 10 samples.

In addition, beyond natural channel effects, optical components can introduce controlled polarisation transformations. The polarisation transformation induced by optical elements, such as retroreflectors, is mathematically described through the Jones matrix formalism [119]:

$$\begin{pmatrix} E'_x \\ E'_y \end{pmatrix} = \begin{pmatrix} J_{11} & J_{12} \\ J_{21} & J_{22} \end{pmatrix} \begin{pmatrix} E_x \\ E_y \end{pmatrix} \tag{7.1}$$

where the Jones matrix elements J_{ij} are determined by the optical properties of the element and the incident beam geometry. Additionally, retroreflectors introduce deterministic polarisation transformations, converting linearly polarised incident light to elliptically polarised states through differential phase shifts between orthogonal polarisation components upon retroreflection [119]. This predictable polarisation modification forms the theoretical foundation for the proposed transmitter-side sensing mechanism.

And in this chapter, the combination of retroreflector-induced polarisation transformations and channel propagation effects will be discussed due to the potential opportunities for channel state estimation in optical communication systems. In UOWC, where polarisation states are well-maintained as demonstrated in Chapter 4, the retroreflector's deterministic polarisation transformation remains largely unaffected by the channel, enabling reliable extraction of retroreflected signals for sensing applications. This polarisation stability means that intensity variations in the retroreflected signal directly correspond to channel conditions such as turbulence-induced scintillation or turbidity-induced attenuation, rather than being affected by polarisation degradation. In FSO channels, despite greater polarisation variability, the bidirectional propagation through the same atmospheric path ensures that both forward and retroreflected signals experience highly similar channel impairments, including attenuation, scattering, and turbulence effects. This bidirectional path effectively doubles the channel's impact on the retroreflected signal, potentially enhancing the sensitivity of channel state detection. Furthermore, since retroreflectors preserve beam alignment regardless of incident angle, the reflected sensing beam tracks the communication path, ensuring that the measured channel conditions accurately represent those affecting data transmission. These characteristics suggest that retroreflector-based

architectures could enable real-time channel state estimation for adaptive optical communication systems in both underwater and atmospheric environments, providing an alternative to the camera-based approach presented in Chapter 6.

7.3 Experimental Setup and System Architecture

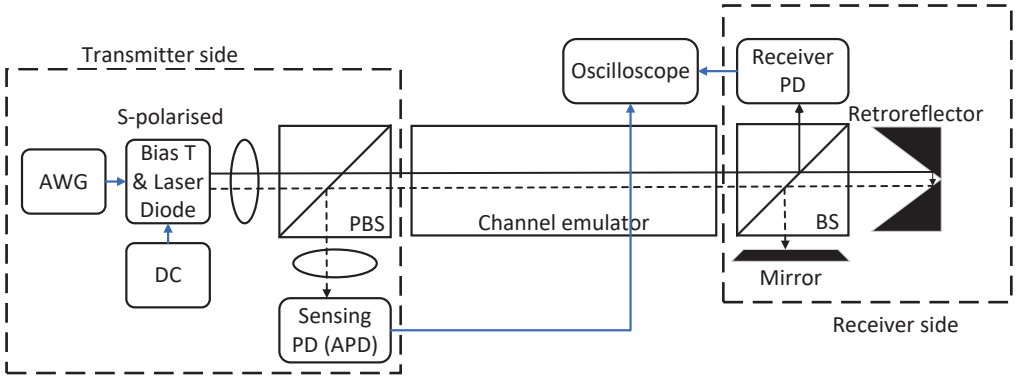

Figure 7.1: *Block diagram of the retroreflector-based CSI estimation system.*

Figure 7.1 illustrates the comprehensive architecture of the proposed retroreflector-based CSI estimation system. Similar to the experimental setup in Chapter 6, the system employs adaptive PAFsk-SIM modulation based on estimation of CSI. However, instead of using a camera to observe backscattered patterns, this system extracts CSI from retroreflected signals that have traversed the channel bidirectionally. The optical transmitter consists of an laser diode operating at 450 nm wavelength and a wideband bias-tee. The laser diode (Osram PL450B) is tuned to transmit s-polarised beam with a DoP of 80%. The bias-tee combines the modulated electrical signal from AWG with a precisely regulated 30 mA DC bias current from power supply, maintaining laser operation within its linear modulation region whilst avoiding thermal instabilities. A polarising beam splitter (PBS) with extinction ratio exceeding 1000:1 directs the s-polarised component through the channel emulator towards a precision 50:50 BS (THORLABS CCM1-BS013/M) positioned at the receiver side. The optical power division from the BS enables simultaneous communication and channel monitoring: 50% of the incident power reaches the high-speed communication PD (Femto HSPR-X-I-1G4-SI), whilst the remaining power arrives at the corner-cube retroreflector (THORLABS PS975M-B) which reflects the coming beam back toward its original direction by 3 total internal reflections. The retroreflection process induces a deterministic polarisation transformation from linear to elliptical states

through differential phase retardation. When the beam is reflected to the transmitter, the elliptical polarisation state enables the PBS to extract a fraction of the retroreflected signal for channel monitoring via an APD (THORLABS APD430A/M). The retroreflector's inherent property of preserving beam alignment regardless of incident angle eliminates the need for active tracking, thereby establishing an accurate and robust CSI estimation architecture. In addition, as the BS will reflect the beam (elliptical polarisation state) from the retroreflector, a mirror is put next to the BS for reflecting the beam back to the system and reduce the optical power loss.

The signal generation process utilises a Keysight M8195A AWG, controlled through MATLAB for precise waveform synthesis. To enable hierarchical data transmission with varying reliability levels, the data is modulated using three-dimensional hierarchical SIM method proposed in [67]. In the front of the high-frequency data-carrying subcarriers, the transmitted signal includes two distinct pilot signal: FSK modulated signal to indicate the current modulation scheme and a low-frequency square wave that facilitates channel state sensing and time synchronisation. Using FSK modulated pilot signal is shown to be robust even in hostile channel conditions and successfully used to identify the modulation scheme of the current transmission signal in our previous work [146]. Signal acquisition employs an Agilent DSA90804A oscilloscope, enabling simultaneous capture of both communication and sensing channels for comprehensive offline signal processing and performance analysis. For the channel emulator, the generation of temperature-induced turbulence, bubble-induced turbulence and foggy conditions are as same as described in Section 6.3.

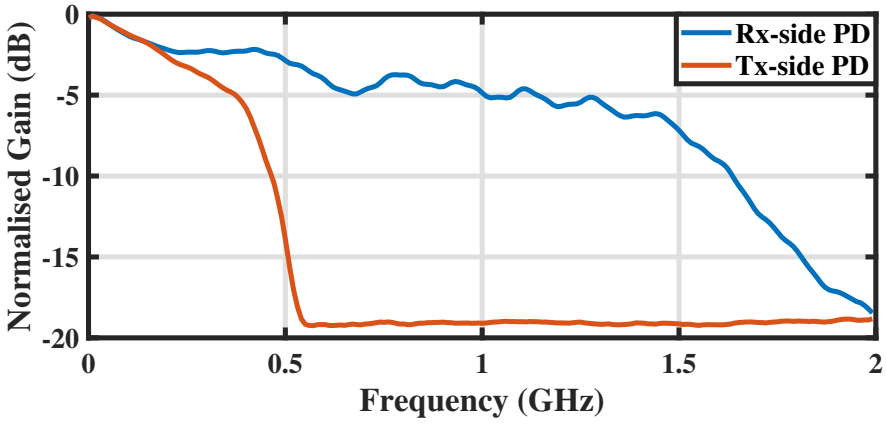

Figure 7.2: *Frequency response of the transmitter-side sensing APD and receiver-side PIN photodiode.*

Figure 7.2 presents the experimentally characterised frequency responses of the receiver sub-

systems. The communication PD exhibits a -3 dB bandwidth of 900 MHz, enabling multi-gigabit data transmission whilst maintaining acceptable signal integrity. The -3 dB bandwidth of the sensing APD is measured to be 400 MHz, which supports channel state estimation via pilot square wave detection. Importantly, the APD's internal avalanche gain mechanism yields a sensitivity enhancement of approximately 20 dB compared to the PIN photodiode, compensating for the reduced optical power in the sensing path. This deliberate bandwidth asymmetry represents an optimal design trade-off: the sensing subsystem prioritises sensitivity over bandwidth, as channel variations occur at timescales significantly slower than the data modulation rate.

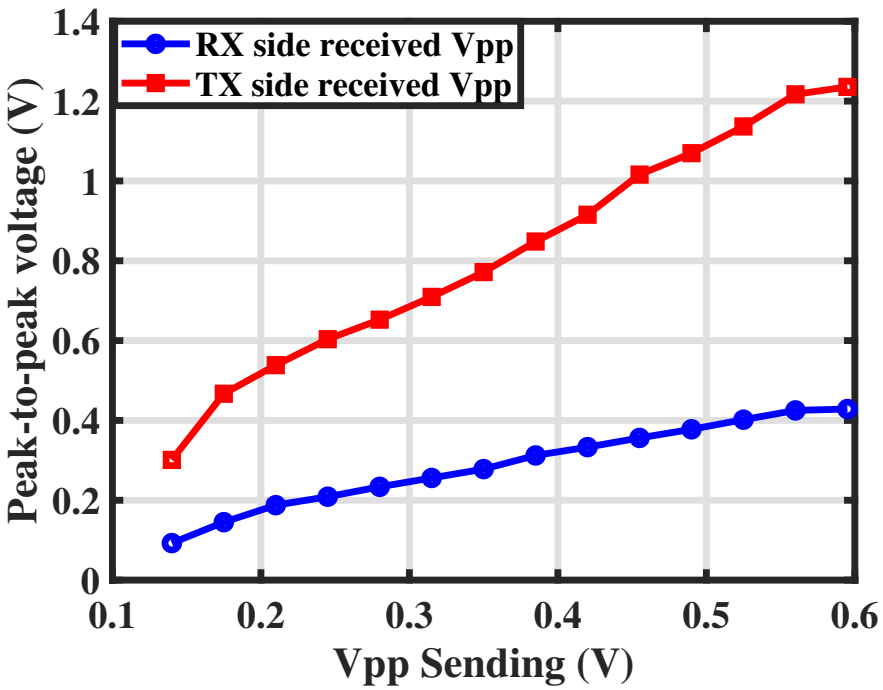

Figure 7.3: *Received peak-to-peak voltage at the transmitter (Tx) and receiver (Rx) sides versus the transmitted signal amplitude.*

Figure 7.3 presents a characterisation of the system's electro-optical transfer function, revealing critical operational constraints. The linear modulation regime spans transmitted peak-to-peak voltages (V_{pp}) from 0.14 V to 0.57 V, within which both photodetectors maintain proportional responses. For $V_{pp} > 0.56$ V, the laser diode exhibits gain compression, thus, the operational signal amplitude is restricted to $V_{pp} \leq 0.56$ V to preserve modulation linearity and minimise intermodulation products. Notably, the sensing APD demonstrates a sensitivity advantage of approximately 3 times relative to the PIN photodiode, thereby enhancing the SNR for robust

channel estimation.

7.4 Channel Characterisation and Sensing Methodology

7.4.1 Characterisation and Sensing of Turbulent Underwater Channels

The turbulence generation and measurement methodology used here follows the same approach as described in Chapter 4, where temperature-induced and bubble-induced turbulence were systematically characterised using the scintillation index as the channel quality metric.

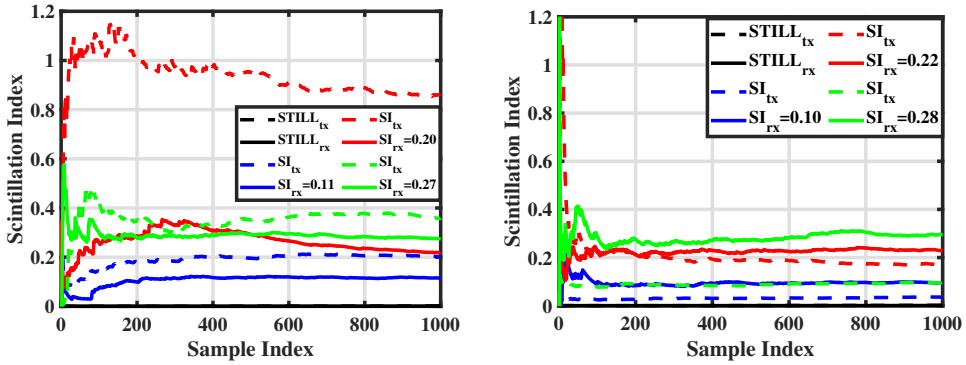

(a) *Temperature-induced turbulence* **(b)** *Bubble-induced turbulence*

Figure 7.4: *Scintillation index convergence with accumulated samples in turbulent UOWC channels.*

Accurate statistical characterisation of turbulence-induced scintillation index requires sufficient temporal sampling to ensure convergence of the scintillation index estimator. Figure 7.4 presents the empirical convergence behaviour of SI estimation for still water, temperature-induced turbulence, and bubble-induced turbulence. The turbulence strength is represented by the SI measured at the receiver side, whilst the SI measured at the transmitter-side is represented by the same colour but with dotted lines in the figure. The SI of the still water condition remains at zero, as shown in both subfigures.

Figure 7.4a demonstrates SI measurements with temperature-induced turbulence across three representative turbulence strengths. The experimental data reveals that statistical convergence to within 5% of the asymptotic SI value requires approximately 600 independent samples. The experimental data shows that transmitter-side sensing measurements consistently yield higher

scintillation index estimates compared to receiver-side observations. This phenomenon can be attributed to the bidirectional propagation path of the retroreflected signal, which traverses the turbulent medium twice before detection at the transmitter-side.

Figure 7.4b presents a similar convergence analysis for bubble-induced turbulence, revealing distinctly different statistical behaviour. Bubble-induced scintillation achieves statistical convergence with approximately 400 samples. This accelerated convergence stems from fundamental differences in the underlying physical mechanisms: bubble-induced turbulence manifests itself as discrete, temporally localised scattering events with characteristic timescales determined by bubble transit times across the beam, whereas temperature-induced turbulence produces random, continuous, spatially correlated refractive index fluctuations. However, the SI at the transmitter-side is lower than at the receiver side, which can be attributed to differences in the scattering characteristics between bubble-induced and temperature-induced turbulence. These differences between transmitter-side and receiver-side measurements provide opportunities to distinguish between different turbulent water conditions.

Channel Condition	SI (approximate)	R^2	Fitting parameters
Tem1 (blue)	0.11	0.97	GGD: $a = 0.60, b = 1.20, c = 4.96$
Tem2 (red)	0.20	0.94	GGD: $a = 0.45, b = 1.45, c = 3.95$
Tem3 (green)	0.27	0.96	GGD: $a = 1.43, b = 0.87, c = 1.55$
Bub1 (blue)	0.10	0.97	EL: $w = 0.19, \lambda_{\text{EL}} = 0.34, \mu = 0.13, \sigma^2 = 9 \times 10^{-3}$
Bub2 (red)	0.22	0.96	EL: $w = 0.52, \lambda_{\text{EL}} = 0.92, \mu = 0.30, \sigma^2 = 5.3 \times 10^{-3}$
Bub3 (green)	0.28	0.95	EL: $w = 0.42, \lambda_{\text{EL}} = 0.11, \mu = 0.34, \sigma^2 = 2.8 \times 10^{-3}$

Table 7.1: *Fitting parameters for received intensity distributions in turbulent UOWC channels.*

To sense the channel, more details about received V_{pp} at transmitter and received side are needed. Figure 7.5 and Table 7.1 demonstrate and provide comprehensive fitting curves and parameters for received V_{pp} at the receiver side with different turbulence types. Figure 7.5 also illustrates the distribution of the received V_{pp} at the transmitter-side.

Figure 7.5(a) presents the empirical probability density functions (PDFs) of the normalised received power under temperature-induced turbulence. The blue, red and green represents the tested turbulence of $SI \approx 0.11$, $SI \approx 0.20$, and $SI \approx 0.27$. The receiver-side intensity distributions exhibit a strong fit to the generalised gamma distribution (GGD) model, yielding coefficients of determination $R^2 > 0.94$, thereby validating the theoretical framework for

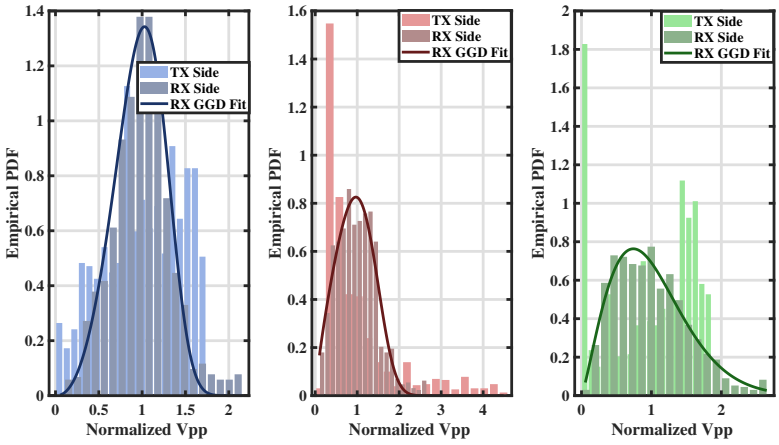

(a) *Temperature-induced turbulence*

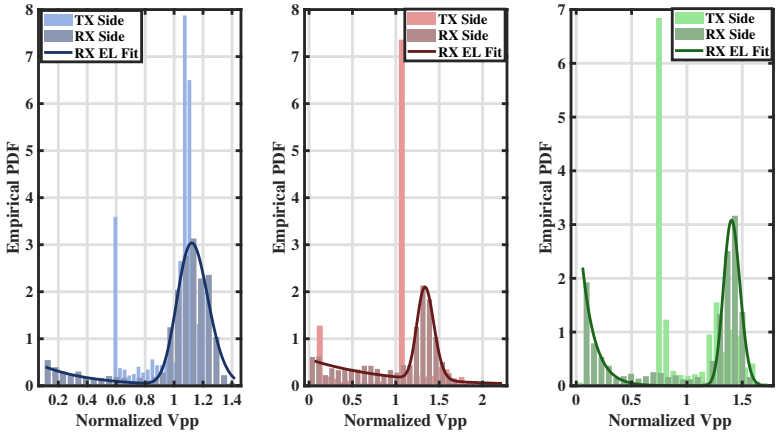

(b) *Bubble-induced turbulence*

Figure 7.5: *Normalised intensity distributions at transmitter and receiver sides under turbulent UOWC conditions.*

weak-to-moderate turbulence regimes. In contrast, transmitter-side distributions exhibit significant positive skewness characterised by extended high-intensity tails that deviate substantially from receiver-side statistical models. This asymmetry arises from the bidirectional propagation through turbulence realisations, polarisation-dependent scattering cross-sections, and different responsivity characteristics between the sensing APD and data PIN photodiode.

Figure 7.5(b) presents the corresponding statistical analysis for bubble-induced turbulence. The blue, red and green represents the tested turbulence of $SI \approx 0.10$, $SI \approx 0.22$, and $SI \approx 0.28$. The receiver-side intensity statistics conform to an exponential lognormal (EL) distribution with $R^2 > 0.95$, consistent with predictions for discrete scattering events superimposed on continuous background turbulence. The concentration of V_{pp} values received at the transmitter-side within a narrower range indicates the observation of lower SI values compared to the receiver side, which aligns the results in Fig. 7.4b.

Importantly, Fig. 7.5 shows that the received V_{pp} distributions at the transmitter-side differ among the six different turbulent water conditions, which provides the possibility to sense the channel at the transmitter-side with sufficient received V_{pp} samples.

Channel state estimation requires optimising the fundamental trade-off between statistical accuracy and temporal resolution. From the perspective of simplified system design, sliding window and block-based estimation approaches are considered in this work. With each new received transmitter-side V_{pp} sample, the sliding window approach incorporates the new data whilst discarding the oldest data, then performs the estimation; in contrast, the block-based estimation accumulates new data up to a predetermined amount before estimating the channel state.

Figure 7.6 presents a comprehensive comparative analysis of sliding window and block-based estimation algorithms. The figures show the mean value and variance of the difference between estimated SI in various turbulent water conditions and still water based on the received V_{pp} at transmitter-side.

The sliding window estimator (Figs. 7.6a and 7.6c) demonstrates an estimation capability with reduced variance for SI samples window sizes between 0-20 samples. When the SI samples window size goes up above 10, the mean value and variance of SI difference almost keep a constant value. Thus, it can be noted that at a SI samples window size of 10, the estimator achieves optimal performance, balancing response speed with sufficient statistical reliability. Looking at $SI \approx 0.20$ and $SI \approx 0.22$ in temperature-induced turbulent and bubble-induced

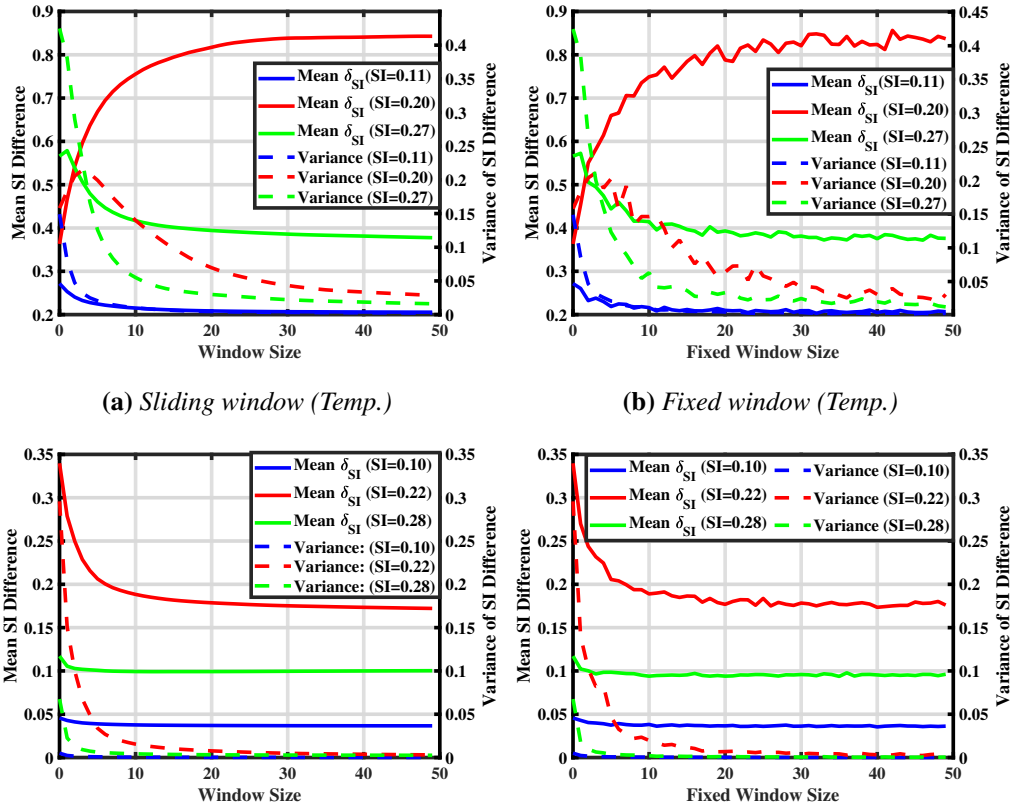

(a) *Sliding window (Temp.)* **(b)** *Fixed window (Temp.)*

(c) *Sliding window (Bubble)* **(d)** *Fixed window (Bubble)*

Figure 7.6: *Performance comparison of sliding window and fixed-size SI samples window approaches for SI estimation under (a)-(b) temperature-induced and (c)-(d) bubble-induced turbulence.*

turbulent water conditions, it can be observed that a mean SI difference converges to 0.40 and 0.18 with variance of 0.13 and 0.02, respectively.

The block-based approach (Figs. 7.6b and 7.6d) exhibits comparable steady-state performance to the sliding window method but suffers from inherent processing latency equal to the block duration and reduced sensitivity to transient channel variations. While the variance characteristics are similar for larger SI samples window sizes, the block-based method cannot adapt to rapid channel fluctuations as effectively. Therefore, the sliding window approach with a 10 SI samples window size is selected for subsequent channel estimation, providing an optimal trade-off between estimation accuracy and temporal responsiveness.

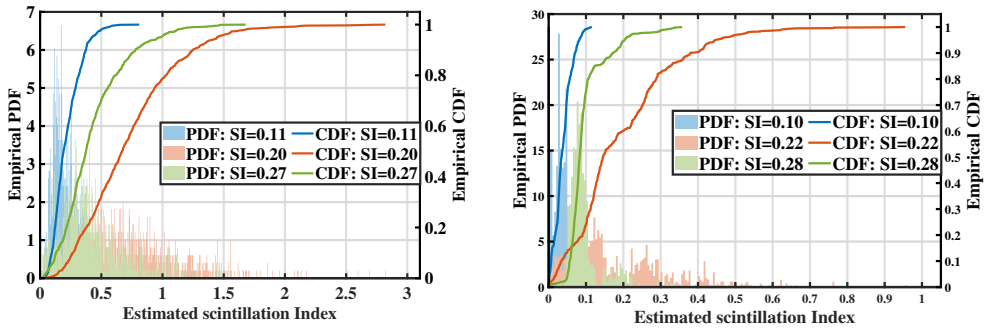

(a) *Temperature-induced* **(b)** *Bubble-induced*

Figure 7.7: *Empirical cumulative distribution functions of estimated SI using a 10-sample sliding window.*

After selecting a sliding SI samples window size of 10, Fig. 7.7 presents the empirical cumulative distribution functions (CDFs) of SI estimates obtained using the optimised 10-sample sliding window estimator to evaluate the distinguishability of different turbulent water conditions at transmitter-side. For temperature-induced turbulence (Fig. 7.7a), the CDFs exhibit well-separated distributions across different turbulence intensities, with inter-class overlap below 5%, ensuring robust turbulence level classification with minimal false alarm probability. The bubble-induced turbulence CDFs (Fig. 7.7b) display similar separation characteristics for distinguishing turbulence strength within the same type. However, overlap exists between temperature-induced and bubble-induced turbulence at similar SI levels, which could complicate channel identification in practical applications. Notably, when the estimated SI is below 0.1, the probability of bubble-induced turbulence (approximately 0.9) significantly exceeds that of temperature-induced turbulence (approximately 0.18), as indicated by the CDF results. Given the more severe impact of temperature-induced turbulence on signal quality, a conser-

vative approach employing more robust transmission schemes is selected when the estimated SI exceeds 0.1. Therefore, whilst this approach may not be suitable for precise turbulence type classification, it can effectively detect the channel impact on transmitted signals before transmission, enabling proactive adaptation strategies to enhance communication robustness.

7.4.2 Characterisation and Sensing Under FSO Fog Conditions

Figure 7.8a establishes the fundamental correlation between transmitter-side sensing measurements and receiver-side signal strength across a range of fog-induced attenuation levels. Operating with a fixed transmitted signal amplitude of 560 mV_{pp}, the experimental data exhibits strong linear correlation ($R^2 = 0.992$) spanning received V_{pp} at receiver side from 0.12 V to 0.42 V. The range representing standard deviation bounds demonstrates an error range where the variation in the estimated received Rx V_{pp} is below 3%. The empirical transfer function relating transmitter-side sensing to receiver-side signal strength is given by:

$$V_{pp}^{\text{Rx,est}} = 0.2576 \cdot V_{pp}^{\text{Tx,meas}} + 0.1267 \tag{7.2}$$

Figure 7.8b illustrates the differential sensitivity of the retroreflector-based sensing mechanism. The blue curve shows fog attenuation effects when transmitting at a constant 600 mV_{pp}, whilst the red curve represents the response when varying transmitted power from 0.14 V to 0.6 V in clear conditions (no fog). The experimental data reveals that the retroreflected signal experiences greater attenuation relative to the single-pass communication link under fog conditions, a consequence of the bidirectional propagation through the FSO channel. This enhanced sensitivity provides an advantage for proactive channel adaptation: the sensing subsystem detects signal degradation before the next transmission, enabling pre-emptive modulation adaptation before link quality deteriorates below acceptable thresholds.

7.5 Experimental Results and Performance Evaluation

This section introduces the adaptive modulation strategy for varying UOWC turbulence and FSO foggy channel, and evaluate the performance of the proposed systems in varying channels with experiments. For each set of experiment, the total number of transmitted bits are over 480000.

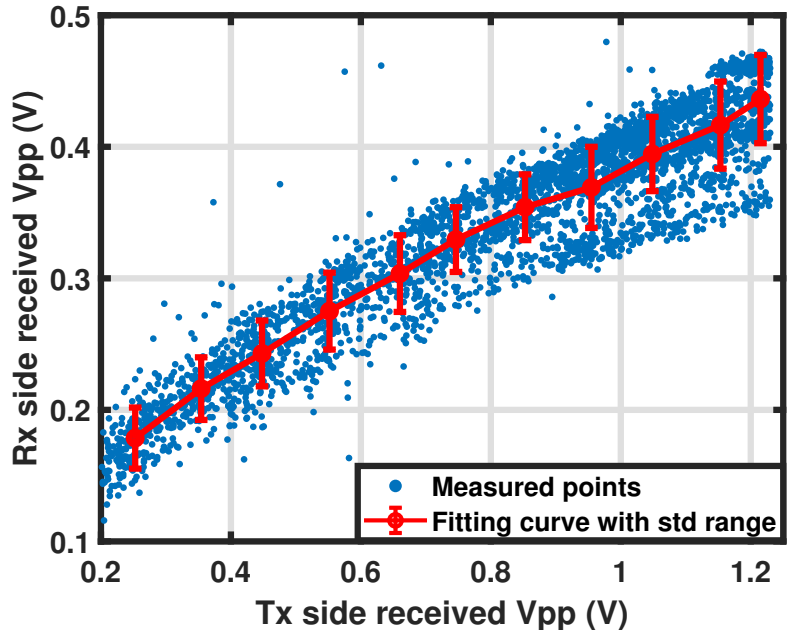

(a) *Mapping of received voltages in a foggy channel with fixed 600 mV_{pp} transmission*

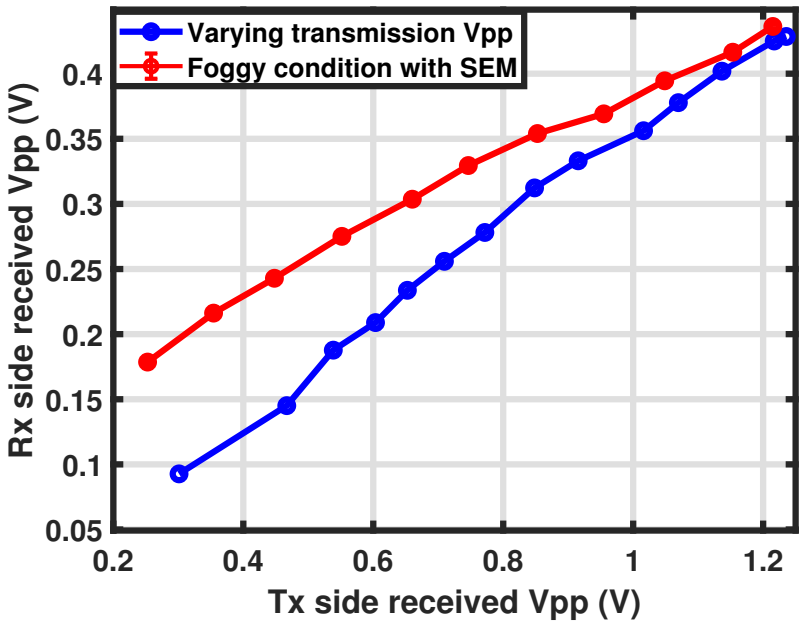

(b) *Comparison of fog attenuation effects (with 600 mV_{pp} transmission) versus transmitted power variation effects (without fog, varying transmission from 0.14 V to 0.56 V).*

Figure 7.8: *Correlation between transmitter-side and receiver-side measurements.*

7.5.1 Adaptive Modulation Strategy Design

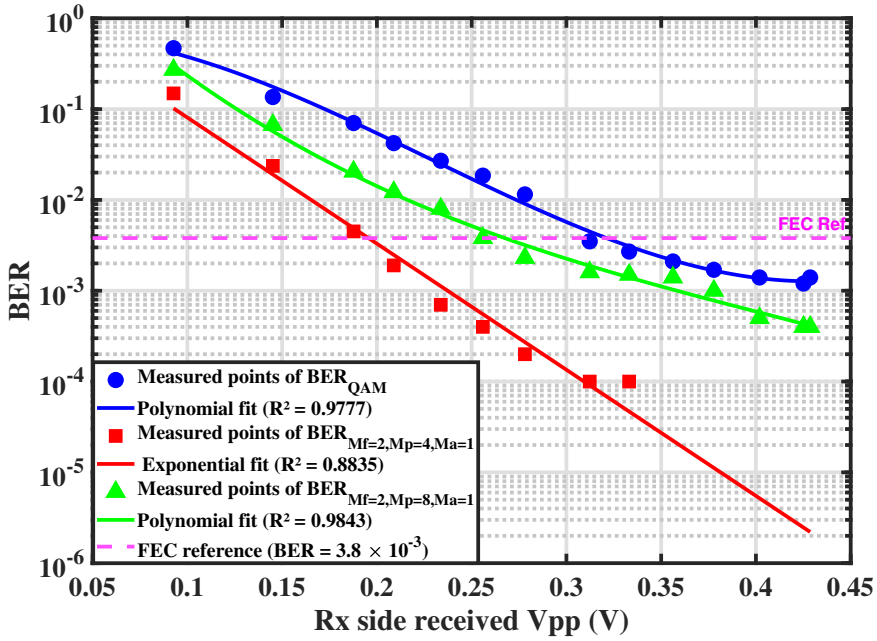

Figure 7.9: *BER performance versus received signal strength for different PAFsk-SIM modulation schemes.*

The proposed adaptive modulation framework employs three PAFsk-SIM configurations, each scheme optimised for specific channel impairment levels based on the three-dimensional hierarchical signalling paradigm established in [67]. The forward error correction (FEC) threshold in this work is selected as 3.8×10^{-3}. Figure 7.9 presents comprehensive BER characterisation curves as a function of received signal amplitude for the candidate modulation schemes. The high-throughput 16-QAM configuration ($M_f = 1, M_{pa} = 16$) achieves the highest transmission speed of 4.2 Gbps under clear channel conditions but exhibits BER over FEC when rx side received V_{pp} is less than 0.32 V. The scheme ($M_f = 2, M_p = 8, M_a = 1$) delivers 3.3 Gbps whilst maintaining BER below FEC threshold for rx side received V_{pp} over 0.25 V, with increased resilience to hostile channel conditions compared to the 16-QAM configuration. The most resilient scheme ($M_f = 2, M_p = 4, M_a = 1$) sustains reliable communication at 2.5 Gbps with rx side received V_{pp} over 0.18 V, demonstrating the robustness of frequency-domain encoding against amplitude fluctuations. These empirical BER curves serve as the foundation for threshold-based modulation selection.

For underwater channels dominated by turbulence-induced fading, the adaptation algorithm employs a threshold-based decision framework utilising the sliding window SI estimates. The

modulation switching thresholds were empirically optimised through extensive BER measurements across the full range of turbulence conditions, yielding the following decision boundaries:

- **Still water** ($SI \approx 0$ with estimated SI < 0.06): Deploy 16-QAM ($M_f = 1, M_{pa} = 16$) achieving 4.2 Gbps throughput
- **Bubble-induced turbulence** ($SI \approx 0.1$ with $0.06 \leq$ estimated SI < 0.1): Transition to $M_f = 2, M_p = 8, M_a = 1$ maintaining 3.3 Gbps
- **Temperature-induced turbulence** ($SI \approx 0.12$ with estimated SI ≥ 0.1): Switch to $M_f = 2, M_p = 4, M_a = 1$ ensuring 2.5 Gbps

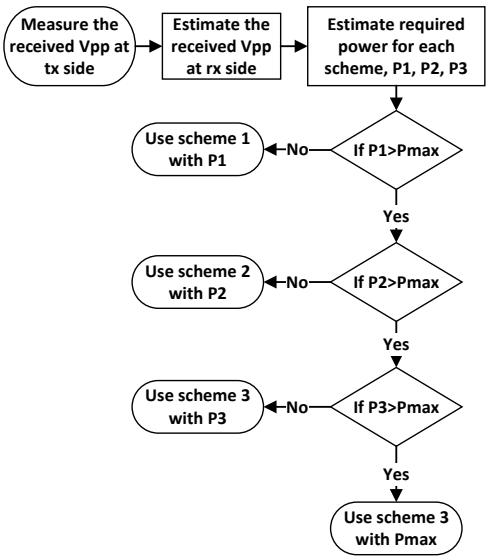

Figure 7.10: *Adaptive strategy flowchart for foggy FSO channels.*

For atmospheric FSO channels impaired by fog-induced attenuation, the adaptation strategy implements a joint power-modulation optimisation algorithm, illustrated in Fig. 7.10. The control algorithm operates through a two-stage decision process: first, it computes the minimum transmitted power required to achieve the target BER for each candidate modulation scheme based on optical power attenuation estimates from the CSI estimation subsystem; second, it selects the highest-throughput modulation scheme whose power requirement remains within the laser's linear operating region ($V_{pp} \leq 0.56$ V). This adaptive modulation framework aims

for performance degradation with BER below FEC as fog density increases, prioritising link availability over throughput when channel conditions deteriorate.

7.5.2 Performance Evaluation in Turbulent Underwater Channels

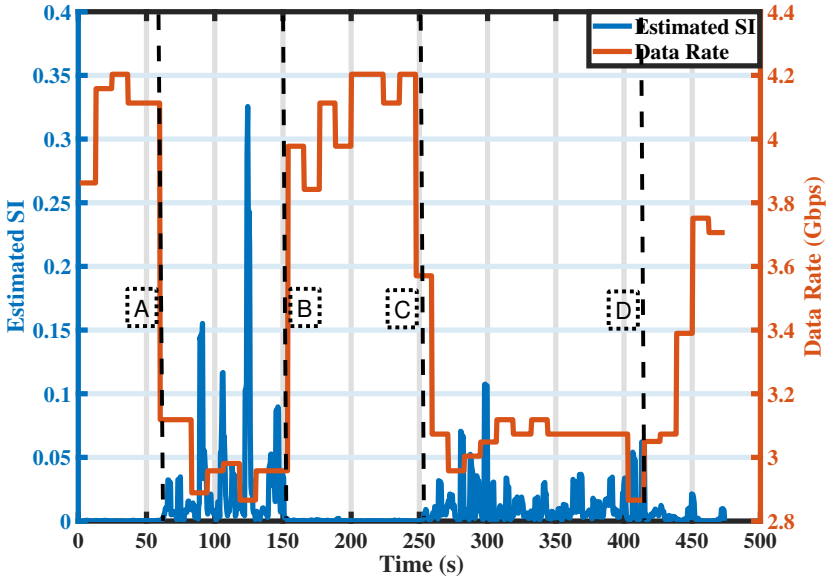

Figure 7.11: *Sliding window SI estimation and adaptive data rate selection in a time-varying UOWC channel.*

To evaluate the performance of the proposed adaptive system with retroreflector-based CSI estimation under practical operating conditions, time-varying turbulent underwater channels were systematically generated in the channel emulator. The temporal evolution of system performance is illustrated in Fig. 7.11, demonstrating the adaptive response to varying turbulence conditions over a 500-second experimental duration. As the proposed algorithm needs a sliding window with a size of 10 SI samples, before the recorded number of windows goes up to 10, the system will use scheme of $M_f = 2, M_p = 4, M_a = 1$. Region before A (0-50 s) represents the still water condition, the estimated SI is nearly 0 and the data rate is over 4 Gbps. Region from A to B (50-150 s) introduces bubble-induced turbulence, creating discrete scattering events that cause rapid intensity fluctuations which is caught by the estimated SI. During this phase, the adaptive system executes transitions between $M_f = 2, M_p = 4, M_a = 1$ and $M_f = 2, M_p = 8, M_a = 1$ as the estimated SI varies. The bubble machine is shut down after time stamp B, the estimated SI gradually goes down and stays at 0, the data rate increases as there is no turbulence-induced fading during this period. In the region from C to D (250-400

s) temperature-induced turbulence is introduced to the channel, exhibiting high variance in the estimated SI but overall lower estimated SI values, as expected. This prompts the system to choose $M_f = 2, M_p = 4, M_a = 1$ or $M_f = 2, M_p = 8, M_a = 1$ based on estimated SI for stable communication. In the region after D (400-500 s), as temperature-induced turbulence dissipates, the system exhibits progressive performance recovery, incrementally transitioning through higher-order modulation schemes as channel conditions improve towards baseline clear water conditions. Additionally, when the channel is transitioning from still to turbulence, the data rate drops much faster compared to when the channel is transitioning from turbulent to still, this ensures the robustness of the system and can be attributed to the sensitivity of the proposed sliding sensing window.

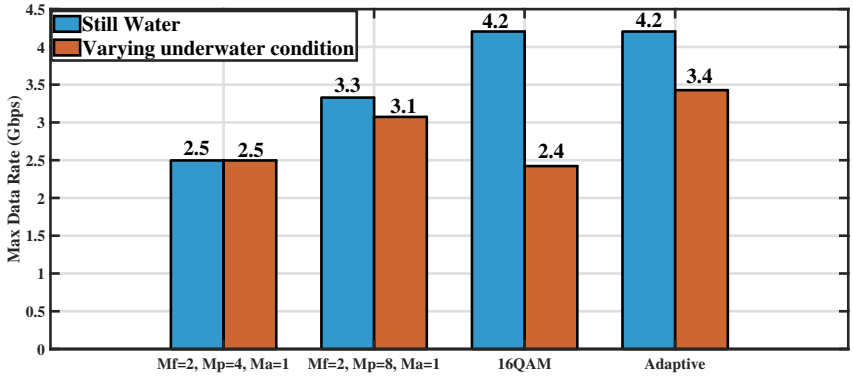

Figure 7.12: *Performance comparison of adaptive versus fixed modulation schemes in the UOWC channel.*

The results presented in Fig. 7.12 demonstrate the impact of channel variations on modulation performance. The experimental results demonstrate that fixed modulation schemes experience substantial performance degradation when transitioning from still water to turbulent conditions. The 16-QAM configuration achieves 4.2 Gbps in still water but drops to an average of 2.4 Gbps across turbulent conditions (43% reduction) with BER of 0.003. The relatively robust scheme ($Mf = 2, Mp = 8, Ma = 1$) experiences a 21% throughput decrease from 4.2 to 3.3 Gbps with BER of 0.0032. The most robust scheme ($Mf = 2, Mp = 4, Ma = 1$) maintains a stable 2.5 Gbps with BER of 0.0021 but still with lower data rate. These results align with the robustness difference shown in Fig. 7.9.

In contrast, the adaptive system with retroreflector-based CSI estimation demonstrates solid resilience, achieving a time-averaged data rate of 3.4 Gbps with an average BER of 0.0037 across varying turbulent conditions. This performance is comparable to Chapter 6's camera-based ap-

proach, which achieved 3.51 Gbps average throughput, validating that both CSI estimation techniques can effectively enable adaptive transmission. Additionally, the adaptive system achieves a 9% improvement over the best-performing fixed configuration ($Mf = 2, Mp = 8, Ma = 1$) in varying UOWC channels, highlighting the effectiveness of the proposed modulation adaptation.

7.5.3 Performance Evaluation in Foggy FSO Channels

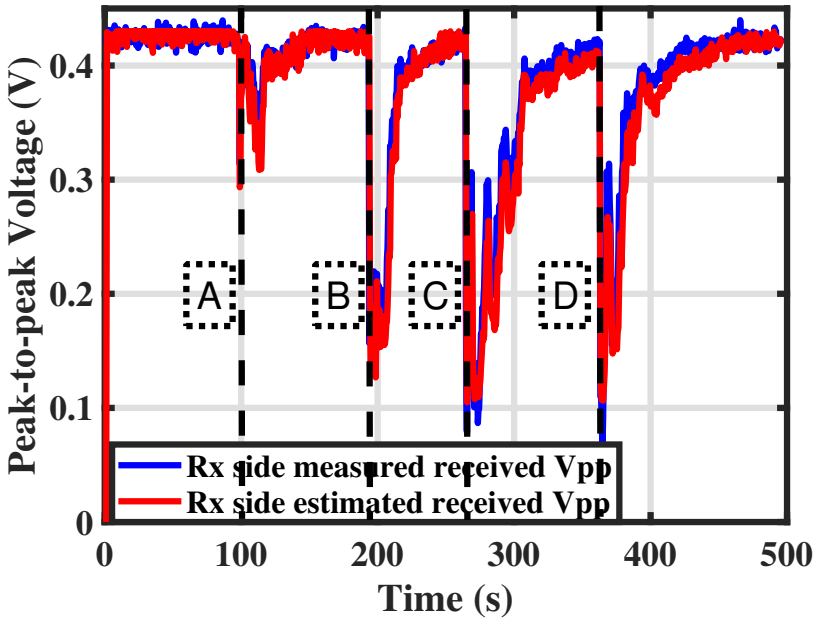

Figure 7.13: *Validation of receiver-side signal estimation accuracy using transmitter-side sensing during dynamic fog events.*

To evaluate the adaptive system with retroreflector-based CSI estimation performance under atmospheric FSO conditions, controlled time-varying fog densities were systematically generated in the channel emulator. Figure 7.13 presents the empirical validation of channel estimation accuracy under varying fog conditions. Region before A (0-100 s) represents clear atmospheric conditions where the measured receiver-side V_{pp} remains at approximately 0.4 V with closely matching estimated values. Region from A to B (100-200 s) introduces light fog to the channel, reducing the measured V_{pp} to approximately 0.35 V while the estimation tracks this decrease. In the region from B to C (200-300 s), moderate levels of fog are added to the channel and measured V_{pp} drops to around 0.25 V and the estimation maintaining accurate tracking. Re-

gion from C to D (300-400 s) creates dense fog conditions, where the measured V_{pp} reaches minimum values of approximately 0.15 V, with the estimation still following the trend despite severe attenuation. Region after D (400-500 s) demonstrates the fog fading away, with V_{pp} gradually increasing from 0.15 V back towards 0.4 V as fog clears, and the estimation accurately tracking this improvement. The strong correlation between estimated and measured V_{pp} values throughout all fog conditions validates the transmitter-side sensing accuracy and allows for robust modulation selection.

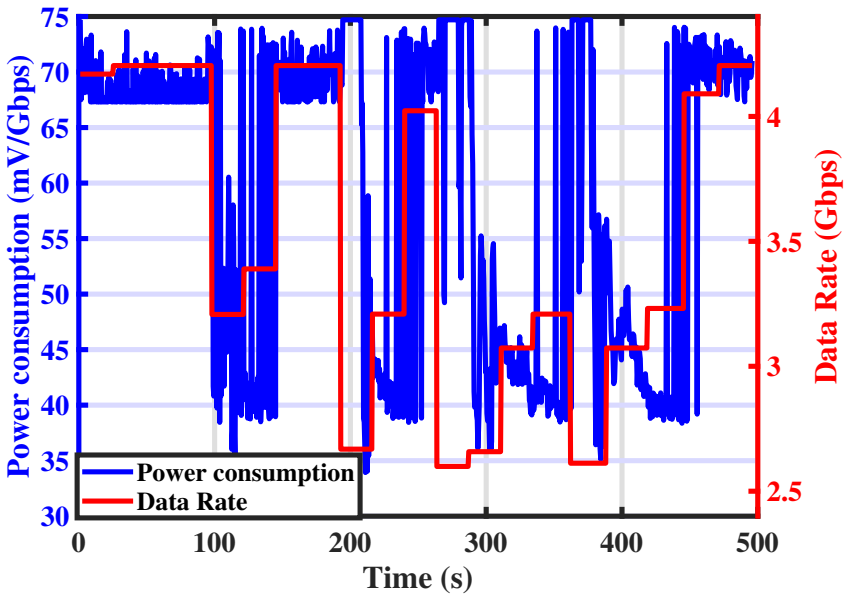

Figure 7.14: *Power consumption and adaptive data rate evolution in a time-varying foggy FSO channel.*

The joint power-modulation adaptation under time-varying atmospheric conditions is demonstrated in Fig. 7.14. As the proposed algorithm needs at least one reading from the last transmitted signal before next transmission, the system will use scheme of $M_f = 2, M_p = 4, M_a = 1$ as the first transmission. During light fog event A to B (t = 100-200 s), the system executes power pre-compensation, increasing transmitted power whilst maintaining high-order modulation to preserve throughput. The moderate fog B to C (t = 200-300 s) triggers further power increase with potential modulation adjustment. The dense fog event C to D (t = 300-400 s) requires comprehensive adaptation: transmitted power increases to the maximum permissible level (600 mV_{pp}) whilst transitioning to the most robust modulation scheme (2.5 Gbps PAFsk-SIM) to maintain link connectivity. The recovery phase after D (400-500 s) demonstrates re-optimisation capabilities, with the system executing stepped transitions through intermediate

modulation schemes and progressively reducing transmitted power as visibility improves.

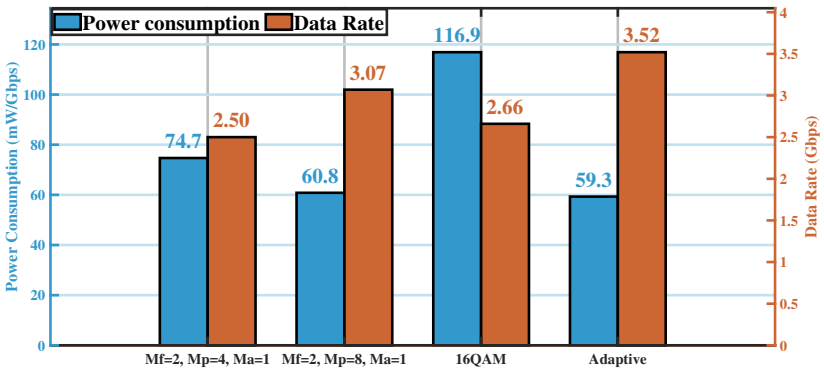

Figure 7.15: *Aggregate performance comparison in the foggy FSO channel.*

The performance metrics presented in Fig. 7.15 demonstrate the impact of fog conditions on different modulation strategies. Fixed modulation schemes exhibit severe limitations when transitioning from clear to foggy conditions. The 16-QAM configuration achieves 2.66 Gbps at 116.9 mW/Gbps with a BER of 0.0027 in varying fog condition. The scheme ($Mf = 2, Mp = 8, Ma = 1$) delivers 3.07 Gbps at 60.8 mW/Gbps under varying fog with BER = 0.002. The robust scheme ($Mf = 2, Mp = 4, Ma = 1$) maintains stable 2.66 Gbps with BER $= 9.8090 \times 10^{-4}$ across the varying fog conditions, with a power consumption of 74.7 mW/Gbps.

Under identical varying fog conditions, the adaptive system with retroreflector-based CSI estimation demonstrates improved resilience through joint channel monitoring and power-modulation adaptation, achieving time-averaged data rate of 3.52 Gbps with power efficiency of 59.3 mW/Gbps and average BER = 0.0031. Compared to the best-performing fixed scheme ($Mf = 2, Mp = 8, Ma = 1$) which achieves 3.07 Gbps at 60.8 mW/Gbps, the adaptive system delivers 15% higher data rate while maintaining comparable power efficiency, establishing the effectiveness of retroreflector-based CSI estimation in FSO OWC systems.

7.6 Summary

This chapter has presented a retroreflector-based channel state estimation technique for adaptive optical wireless communication systems. Building upon the CSI-driven adaptation framework established in Chapter 6, this approach offers an alternative to camera-based channel monitoring by exploiting polarisation transformations in retroreflected signals.

The key distinction from Chapter 6's visual pattern recognition approach is the direct optical measurement of channel effects without requiring image processing or machine learning algorithms. The retroreflector-based method provides aligned communication optical channel and feedback channel while maintaining comparable adaptation performance. Compared to the camera-based system in Chapter 6, the two approaches have complementary strengths. For turbulent UOWC, the camera-based k-NN classifier achieves 99% discrete state accuracy, which is higher than the continuous SI estimation from the retroreflected signal, making it the more reliable turbulence classifier. For foggy FSO, the retroreflector-based method directly measures optical attenuation at the transmitter side, providing a more accurate and stable fog estimate than the camera's Canny edge detection, which is subject to frame-to-frame ECF variability. This accuracy advantage enables the retroreflector system to jointly adapt both modulation order and transmitted power, achieving 3.52 Gbps at BER $= 0.0031$, whereas the camera-based system adapts modulation order only, achieving 3.51 Gbps at BER $\leq 2.9 \times 10^{-3}$.

Chapter 8
Conclusion and Future Work

8.1 Summary of the Work

This thesis has addressed the challenge of establishing robust OWC links in hostile channel environments through different approaches. The research has systematically investigated and developed novel techniques including advanced modulation, intelligent tracking, adaptive data transmission, integrated CSI estimation and OWC system. The work has demonstrated the performance improvements over existing approaches while maintaining practical implementation feasibility.

The thesis successfully achieved its primary research objectives. First, the development of resilient frequency-based modulation schemes was accomplished, as shown in Chapter 4. An investigation of frequency-based techniques (FSK-SIM and FSCM) combined with PDM demonstrated robustness over conventional amplitude-based methods under different hostile channel conditions. In addition, the results also shows the doubled spectral efficiency, proving that frequency-domain encoding with PDM effectively keeps the resilience against hostile varying channel conditions while achieving high data rates.

Second, the proposed real-time beam tracking system for OWC from Chapter 5, which uses photodetector arrays and step motors, successfully compensates for the effect from random varying misalignment. This system achieved fast response time and maintained link availability above 99.5% in scenarios where untracked systems would fail, validating its viability for robust OWC.

Third, the implementation of adaptive transmission strategies was achieved using the camera-based channel estimation techniques from Chapter 6. This machine learning enhanced approach allows for real-time adaptation of transmission parameters by extracting CSI through images. Using k-NN for turbulence classification and Canny edge detection for fog estimation, the system achieves high accuracy for CSI estimation and higher data rate through the corporation with adaptive transmission.

Fourth, the work developed alternative channel state estimation techniques. Chapters 6 and 7 presented two complementary CSI estimation approaches, a camera-based method using image processing and a retroreflector-based method exploiting polarisation transformations for direct optical monitoring, both of which operate without a dedicated feedback channel. Crucially, both systems are designed as standalone adaptive sensing modules that can be retrofitted to existing OWC deployments currently operating with fixed modulation schemes. Both approaches demonstrated comparable throughput gains of 9–15% over the best-performing fixed scheme under varying channel conditions.

Finally, all research objectives were supported by comprehensive experimental validation. Each technical chapter provided rigorous validation under realistic, controlled channel conditions, systematically comparing new techniques against already developed techniques. Collectively, these contributions address key limitations in OWC by providing practical solutions that balance robustness, data rate, and adaptability, while enhancing the OWC link robustness in challenging environments.

8.2 Limitations and Future Work

Despite the significant contributions of this thesis, some limitations have been identified that present opportunities for future research.

8.2.1 Current Limitations

While this research has made significant contributions to the design of resilient OWC systems, several limitations of the current work must be acknowledged. The experimental OWC channel used in the work, such as controlled laboratory experiments like temperature-induced turbulence, require extended field validation to fully capture the statistical complexities of real-world oceanic and atmospheric conditions, including seasonal variations and extreme weather. Scalability also presents challenges. The proposed tracking systems require precise calibration when considered into practical application; and the computational demands of real-time image processing for adaptive application might be prohibitive for resource-constrained platforms such as AUVs. Furthermore, experiments were conducted over short ranges (under 50 metres), and performance at kilometre-scale distances needs to be re-optimised, considering potentially prohibitive power requirements, especially for mobile systems. The retroreflector-based CSI

approach, while innovative, introduces optical losses impacting the power budget. Environmental sensitivity is another concern, as machine learning models require extensive training data and may struggle with varying initial conditions, while optical components remain susceptible to factors like temperature, humidity, and contamination over the long distance. Finally, integrating the individual effective subsystems (modulation, tracking, adaptation) into a comprehensive solution poses a significant challenge, with potential for unforeseen interactions leading to system instabilities not observed during isolated testing.

8.2.2 Future Research Directions

Building upon the contributions of this thesis, several promising research directions emerge. Advanced machine learning integration, including CNNs for camera-based estimation and reinforcement learning for autonomous optimisation, could enhance performance, while transfer learning might alleviate the burden of extensive training data collection. Combining AOA sensing and adjustment upon current tracking system is promising, the four identical PD channels and differential algorithm can extract the AOA information and generate the correction movement. Hybrid communication architectures combining optical and RF capabilities, potentially using intelligent switching algorithms, could significantly improve system robustness and ensure seamless connectivity during optical link outages. Exploring quantum-enhanced OWC systems, such as integrating quantum key distribution (QKD) over FSO links supported by the robust techniques developed here, offers possibilities for ultra-secure communications, with quantum sensing potentially providing novel channel characterisation methods. Investigating energy harvesting techniques (e.g., solar) and ultra-low-power signal processing is essential for enabling self-powered, autonomous OWC systems suitable for remote, long-term deployments. Lastly, application-specific optimisation is needed to tailor system designs to the unique constraints of different domains, such as underwater environments (considering marine biology, corrosion), automotive applications (focusing on latency, reliability), and indoor VLC systems (balancing communication with illumination and comfort).

The focus of the work in this thesis was improving the robustness of the OWC link and system in challenging channel conditions. The proposed system and findings are demonstrated with validating laboratory results, which can be used for building or designing a practical application in OWC field.

Appendix A
Appendix1

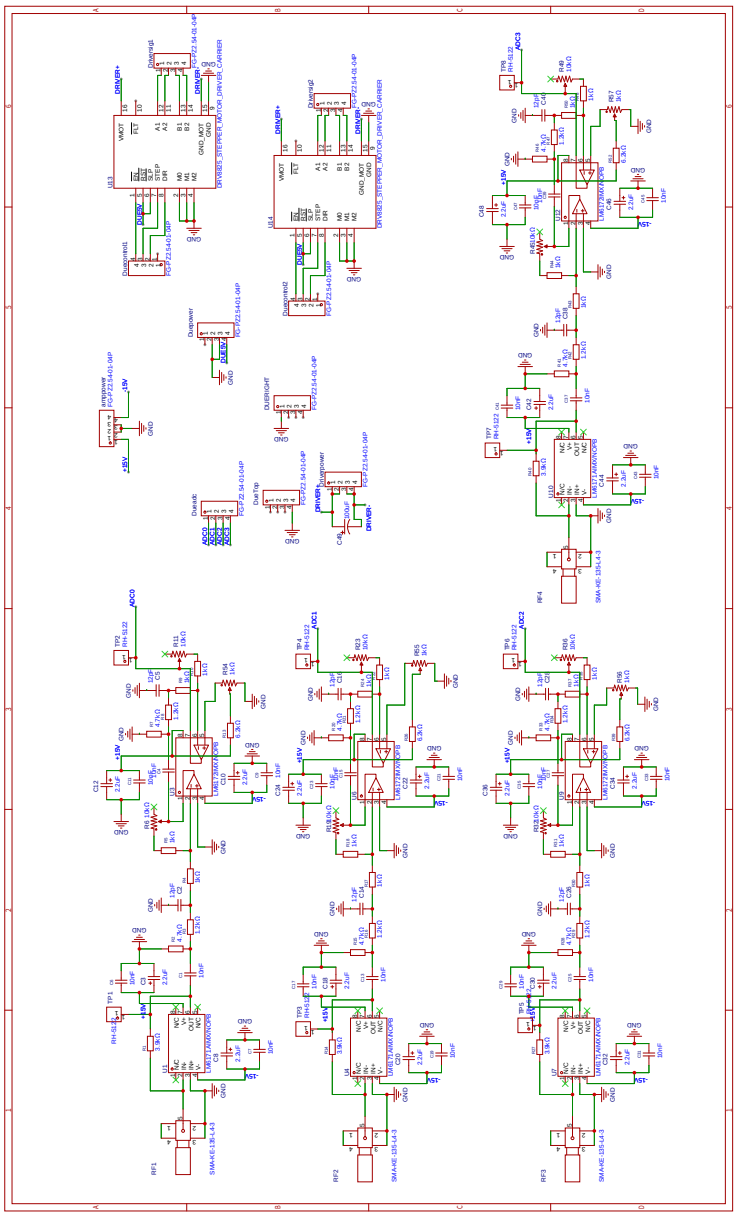

Figure A.1: *Schematic diagram of the Arduino shield.*

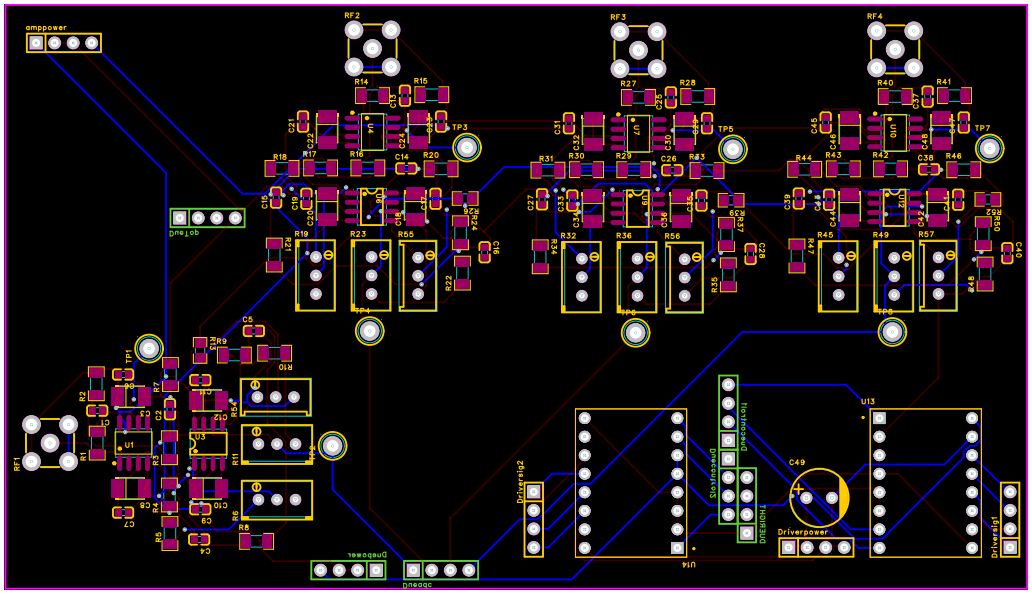

Figure A.2: *Top view of the PCB design for the Arduino shield.*

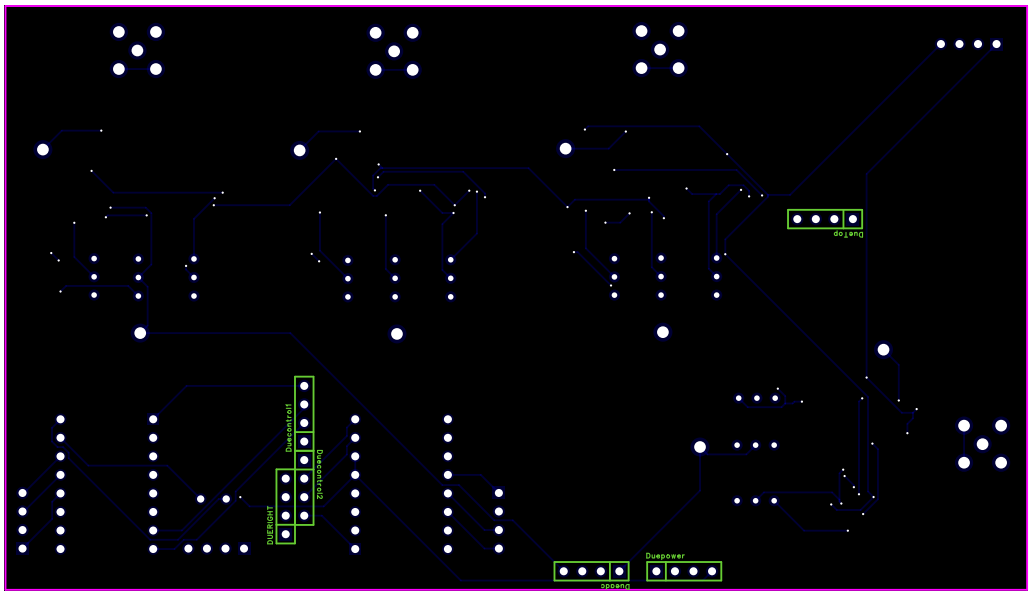

Figure A.3: *Bottom view of the PCB design for the Arduino shield.*

References

[1] H. Haas, L. Yin, Y. Wang, and C. Chen, "What is LiFi?," *Journal of Lightwave Technology*, vol. 34, no. 6, pp. 1533–1544, 2016.

[2] M. A. Khalighi and M. Uysal, "Survey on free space optical communication: A communication theory perspective," *IEEE communications surveys & tutorials*, vol. 16, no. 4, pp. 2231–2258, 2014.

[3] Z. Ghassemlooy, W. Popoola, and S. Rajbhandari, *Optical wireless communications: system and channel modelling with MATLAB*. Boca Raton, FL: CRC Press/Taylor & Francis Group, 2 ed., 2019.

[4] H.-W. Wu and et al., "A 448-gb/s pam4 FSO communication with polarization-multiplexing injection-locked vcsels through 600 m free-space link," *IEEE Access*, vol. 8, pp. 28859–28866, 2020.

[5] H. Kaushal and G. Kaddoum, "Underwater optical wireless communication," *IEEE access*, vol. 4, pp. 1518–1547, 2016.

[6] C. T. Geldard, E. Guler, A. Hamilton, and W. O. Popoola, "An Empirical Comparison of Modulation Schemes in Turbulent Underwater Optical Wireless Communications," *Journal of Lightwave Technology*, vol. 40, pp. 2000–2007, Apr. 2022.

[7] Z. Vali and et al., "Experimental study of the turbulence effect on underwater optical wireless communications," *Applied optics*, vol. 57, no. 28, pp. 8314–8319, 2018.

[8] H. Elgala, R. Mesleh, and H. Haas, "Indoor optical wireless communication: potential and state-of-the-art," *IEEE Communications Magazine*, vol. 49, no. 9, pp. 56–62, 2011.

[9] T. Komine and M. Nakagawa, "Fundamental analysis for visible-light communication system using LED lights," *IEEE Transactions on Consumer Electronics*, vol. 50, no. 1, pp. 100–107, 2004.

[10] M. Sait and et al., "The impact of vertical salinity gradient on non-line-of-sight underwater optical wireless communication," *IEEE Photonics Journal*, vol. 13, no. 6, pp. 1–9, 2021.

[11] L. Zeng and et al., "High data rate multiple input multiple output (MIMO) optical wireless communications using white LED lighting," *IEEE Journal on Selected Areas in Communications*, vol. 27, no. 9, pp. 1654–1662, 2009.

[12] Z. Xu and B. M. Sadler, "Ultraviolet Communications: Potential and State-of-the-Art," *IEEE Communications Magazine*, vol. 46, no. 5, pp. 67–73, 2008.

[13] M. S. Islim and H. Haas, "Modulation techniques for LiFi," *ZTE communications*, vol. 14, no. 2, pp. 29–40, 2019.

[14] H. Henniger and O. Wilfert, "An Introduction to Free-Space Optical Communications," *Radioengineering*, vol. 19, no. 2, pp. 203–212, 2010.

[15] E. F. Schubert, *Light-Emitting Diodes*. Cambridge, UK: Cambridge University Press, 2nd ed., 2006.

[16] F. Yam and Z. Hassan, "Innovative advances in LED technology," *Microelectronics Journal*, vol. 36, no. 2, pp. 129–137, 2005.

[17] S. Nakamura, S. Pearton, and G. Fasol, "The blue laser diode. the complete story," *Measurement Science and Technology*, vol. 12, no. 6, pp. 755–756, 2001.

[18] J. Piprek, *Semiconductor Optoelectronic Devices: Introduction to Physics and Simulation*. San Diego, CA: Academic Press, 2003.

[19] J. J. D. McKendry and et al., "Visible-Light Communications Using a CMOS-Controlled Micro-Light-Emitting-Diode Array," *Journal of Lightwave Technology*, vol. 30, no. 1, pp. 61–67, 2012.

[20] L. A. Coldren, S. W. Corzine, and M. L. Mashanovitch, *Diode Lasers and Photonic Integrated Circuits*. Hoboken, NJ: John Wiley & Sons, 2nd ed., 2012.

[21] J. A. Tatum and et al., "VCSEL-Based Interconnects for Current and Future Data Centers," *Journal of Lightwave Technology*, vol. 33, no. 4, pp. 727–732, 2015.

[22] A. Valle, M. Sciamanna, and K. Panajotov, "Polarization Switching and Polarization Mode Hopping in Quantum Dot Vertical-Cavity Surface-Emitting Lasers," *Physical Review E*, vol. 78, no. 3, p. 036209, 2008.

[23] R. M. Gagliardi and S. Karp, "Optical communications," *New York*, 1976.

[24] J. M. Senior and M. Y. Jamro, *Optical Fiber Communications: Principles and Practice*. Harlow, UK: Pearson Education, 3rd ed., 2008.

[25] O. Popoola, S. Sinanović, W. Popoola, and R. Ramirez-Iniguez, "Optical Boundaries for LED-Based Indoor Positioning System," *Computation*, vol. 7, p. 7, Jan. 2019.

[26] J. C. Campbell and et al., "Recent advances in avalanche photodiodes," *IEEE Journal of selected topics in quantum electronics*, vol. 10, no. 4, pp. 777–787, 2004.

[27] M. A. Khalighi, H. Akhouayri, and S. Hranilovic, "Silicon-photomultiplier-based underwater wireless optical communication using pulse-amplitude modulation," *IEEE Journal of Oceanic Engineering*, vol. 45, no. 4, pp. 1611–1621, 2019.

[28] M. P. Sheehan, J. Tachella, and M. E. Davies, "A sketching framework for reduced data transfer in photon counting lidar," *IEEE Transactions on Computational Imaging*, vol. 7, pp. 989–1004, 2021.

[29] M. A. Esmail, H. Fathallah, and M.-S. Alouini, "Outdoor FSO communications under fog: attenuation modeling and performance evaluation," *IEEE photonics journal*, vol. 8, no. 4, pp. 1–22, 2016.

[30] M. A. Esmail, "Experimental performance evaluation of weak turbulence channel models for FSO links," *Optics Communications*, vol. 486, p. 126776, 2021.

[31] M. A. Esmail, H. Fathallah, and M.-S. Alouini, "Channel modeling and performance evaluation of FSO communication systems in fog," in *2016 23rd International Conference on Telecommunications (ICT)*, pp. 1–5, IEEE, 2016.

[32] W. Liu, Z. Xu, and L. Yang, "SIMO detection schemes for underwater optical wireless communication under turbulence," *Photonics Research*, vol. 3, no. 3, pp. 48–53, 2015.

[33] A. Chaaban, J.-M. Morvan, and M.-S. Alouini, "Free-space optical communications: Capacity bounds, approximations, and a new sphere-packing perspective," *IEEE Transactions on communications*, vol. 64, no. 3, pp. 1176–1191, 2016.

[34] M. A. Esmail, H. Fathallah, and M.-S. Alouini, "Outdoor FSO Communications Under Fog: Attenuation Modeling and Performance Evaluation," *IEEE Photonics Journal*, vol. 8, pp. 1–22, Aug. 2016.

[35] L. D. McGlauchlin and R. B. McQuistan, *Elements of infrared technology: generation, transmission, and detection*. Wiley, 1962.

[36] I. I. Kim, B. McArthur, and E. J. Korevaar, "Comparison of laser beam propagation at 785 nm and 1550 nm in fog and haze for optical wireless communications," in *Optical wireless communications III*, vol. 4214, pp. 26–37, Spie, 2001.

[37] M. Al Naboulsi, H. Sizun, and F. d. r. de Fornel, "Fog attenuation prediction for optical and infrared waves," *Optical Engineering*, vol. 43, no. 2, pp. 319–329, 2004.

[38] M. Schlessinger, *Infrared technology fundamentals*. Routledge, 2019.

[39] C. Loo, "A statistical model for a land mobile satellite link," *IEEE transactions on vehicular technology*, vol. 34, no. 3, pp. 122–127, 1985.

[40] C. Fang, S. Li, Y. Wang, and K. Wang, "High-speed underwater optical wireless communication with advanced signal processing methods survey," in *Photonics*, vol. 10, p. 811, MDPI, 2023.

[41] L. Aguiar-Castillo and et al., "Survey on optical wireless communications-based services applied to the tourism industry: Potentials and challenges," *Sensors*, vol. 21, no. 18, p. 6282, 2021.

[42] C. T. Geldard, *Underwater optical wireless communications in turbulent conditions: from simulation to experimentation*. PhD thesis, University of Edinburgh, 2022.

[43] W. Liu, D. Zou, Z. Xu, and J. Yu, "Non-line-of-sight scattering channel modeling for underwater optical wireless communication," in *2015 IEEE International Conference on Cyber Technology in Automation, Control, and Intelligent Systems (CYBER)*, (Shenyang, China), pp. 1265–1268, IEEE, June 2015.

[44] J. T. Kirk, *Light and photosynthesis in aquatic ecosystems*. Cambridge university press, 1994.

[45] H. Buiteveld, J. Hakvoort, and M. Donze, "Optical properties of pure water," in *Ocean optics XII*, vol. 2258, pp. 174–183, SPIE, 1994.

[46] Z. Zeng and et al., "A survey of underwater optical wireless communications," *IEEE communications surveys & tutorials*, vol. 19, no. 1, pp. 204–238, 2016.

[47] S. A. Thorpe, *The turbulent ocean*. Cambridge university press, 2005.

[48] C. T. Geldard, J. Thompson, and W. O. Popoola, "Effects of turbulence induced scattering on underwater optical wireless communications," *arXiv preprint arXiv:2008.01152*, 2020.

[49] D. J. Bogucki, J. A. Domaradzki, R. E. Ecke, and C. R. Truman, "Light scattering on oceanic turbulence," *Applied Optics*, vol. 43, p. 5662, Oct. 2004.

[50] J. Lian, M. Noshad, and M. Brandt-Pearce, "Comparison of optical OFDM and M-PAM for LED-based communication systems," *IEEE Communications Letters*, vol. 23, no. 3, pp. 430–433, 2019.

[51] J. G. Proakis and M. Salehi, *Digital communications*, vol. 4. McGraw-hill New York, 2001.

[52] J. Ma and et al., "Nonlinear compensation based on k-means clustering algorithm for Nyquist PAM-4 VLC system," *IEEE Photonics Technology Letters*, vol. 31, no. 12, pp. 935–938, 2019.

[53] G. Tilahun, *Enhanced Energy and Spectrum Efficiency in Visible Light Communications*. PhD thesis, University of Edinburgh, 2023.

[54] A. Pradana and et al., "VLC physical layer design based on pulse position modulation (PPM) for stable illumination," in *2015 international symposium on intelligent signal processing and communication systems (ISPACS)*, pp. 368–373, IEEE, 2015.

[55] D.-S. Shiu and J. M. Kahn, "Differential pulse-position modulation for power-efficient optical communication," *IEEE transactions on communications*, vol. 47, no. 8, pp. 1201–1210, 1999.

[56] W. O. Popoola, E. Poves, and H. Haas, "Spatial pulse position modulation for optical communications," *Journal of Lightwave Technology*, vol. 30, no. 18, pp. 2948–2954, 2012.

[57] S. Arnon, "The effect of clock jitter in visible light communication applications," *journal of Lightwave Technology*, vol. 30, no. 21, pp. 3434–3439, 2012.

[58] Y. Roth, J.-B. Doré, L. Ros, and V. Berg, "Turbo-FSK, a physical layer for low-power wide-area networks: Analysis and optimization," *Comptes Rendus Physique*, vol. 18, no. 2, pp. 178–188, 2017.

[59] A. W. Azim and et al., "Energy Efficient M-ary Frequency-Shift Keying-Based Modulation Techniques for Visible Light Communication," *IEEE Transactions on Cognitive Communications and Networking*, vol. 5, no. 4, pp. 1244–1256, 2019.

[60] L. Vangelista, "Frequency shift chirp modulation: The lora modulation," *IEEE signal processing letters*, vol. 24, no. 12, pp. 1818–1821, 2017.

[61] A. Springer and et al., "Spread spectrum communications using chirp signals," in *IEEE/AFCEA EUROCOMM 2000. Information Systems for Enhanced Public Safety and Security (Cat. No.00EX405)*, (Munich, Germany), pp. 166–170, IEEE, 2000.

[62] T. Elshabrawy and J. Robert, "Closed-form approximation of LoRa modulation BER performance," *IEEE Communications Letters*, vol. 22, no. 9, pp. 1778–1781, 2018.

[63] T. T. Nguyen, H. H. Nguyen, R. Barton, and P. Grossetete, "Efficient design of chirp spread spectrum modulation for low-power wide-area networks," *IEEE Internet of Things Journal*, vol. 6, no. 6, pp. 9503–9515, 2019.

[64] W. O. Popoola and Z. Ghassemlooy, "BPSK Subcarrier Intensity Modulated Free-Space Optical Communications in Atmospheric Turbulence," *Journal of Lightwave Technology*, vol. 27, pp. 967–973, Apr. 2009.

[65] C. T. Geldard, E. Guler, A. Hamilton, and W. O. Popoola, "An empirical comparison of modulation schemes in turbulent underwater optical wireless communications," *Journal of Lightwave Technology*, vol. 40, no. 7, pp. 2000–2007, 2022.

[66] E. Guler, C. Geldard, A. Baldwin, and W. Popoola, "A demonstration of frequency-shift keying in underwater optical wireless communications," in *CLEO: QELS_Fundamental Science*, pp. JW3B–104, Optica Publishing Group, 2022.

[67] E. Guler and et al., "3D-Hierarchical Signalling for Resilient Optical Wireless Communication Systems," *IEEE Open Journal of the Communications Society*, 2023.

[68] E. Güler, "Hierarchical subcarrier intensity modulation for resilient optical wireless communication," 2025.

[69] J. Chen and et al., "An experimental demonstration of FSK-SIM-PDM underwater optical wireless communications," in *2022 Sixth Underwater Communications and Networking Conference (UComms)*, pp. 1–4, IEEE, 2022.

[70] C. T. Geldard, I. M. Butler, and W. O. Popoola, "Beyond 10 GBPS in hostile underwater optical wireless communication channel conditions using polarisation division multiplexing," *Journal of Lightwave Technology*, vol. 42, no. 13, pp. 4444–4453, 2024.

[71] Z. Wang and et al., "Beyond 25 Gbps OFDM UOWC System Based on Green and Blue Laser Diodes with Wavelength and Polarization Multiplexing," in *2021 9th International Conference on Communications and Broadband Networking*, (Shanghai China), pp. 329–332, ACM, Feb. 2021.

[72] P. Mandal and et al., "10 Gbps wired and 10 Gbps/20 GHz wireless transmission system employing S and P polarization states of light and OFDM technique," *Optical and Quantum Electronics*, vol. 54, p. 6, Jan. 2022.

[73] C. Gao and et al., "Physical layer encryption for polarization division multiplexing coherent optical communication system based on the rotation of the state of polarization," in *2021 19th International Conference on Optical Communications and Networks (ICOCN)*, (Qufu, China), pp. 1–3, IEEE, Aug. 2021.

[74] J. Armstrong, "OFDM for optical communications," *Journal of lightwave technology*, vol. 27, no. 3, pp. 189–204, 2009.

[75] S. D. Dissanayake and J. Armstrong, "Comparison of ACO-OFDM, DCO-OFDM and ADO-OFDM in IM/DD systems," *Journal of Lightwave Technology*, vol. 31, no. 7, pp. 1063–1072, 2013.

[76] T. Z. Gutema, H. Haas, and W. O. Popoola, "WDM based 10.8 Gbps visible light communication with probabilistic shaping," *Journal of Lightwave Technology*, 2022.

[77] J. Che, S. H. M. Safari, and M. Safari, "Spatial mode multiplexing for fiber-coupled IM/DD optical wireless links with misalignment," *IEEE Transactions on Communications*, 2025.

[78] J. Che, S. Huang, and M. Safari, "Few-mode fiber-coupled indoor optical wireless communication in the presence of misalignment," in *2024 IEEE 99th Vehicular Technology Conference (VTC2024-Spring)*, pp. 1–6, IEEE, 2024.

[79] N. Chi and et al., "Gaussian kernel-aided deep neural network equalizer utilized in underwater PAM8 visible light communication system," *Optics express*, vol. 26, no. 20, pp. 26700–26712, 2018.

[80] N. Chi and et al., "Challenges and prospects of machine learning in visible light communication," *Journal of Communications and Information Networks*, vol. 5, pp. 302–309, Sept. 2020.

[81] M. Abdelsattar, E. S. Amer, H. A. Ziedan, and W. M. Salama, "CNN-LSTM-am approach for outdoor wireless optical communication systems," *Scientific Reports*, vol. 15, no. 1, p. 32178, 2025.

[82] X. Lu and et al., "Memory-controlled deep LSTM neural network post-equalizer used in high-speed PAM VLC system," *Optics express*, vol. 27, no. 5, pp. 7822–7833, 2019.

[83] X. Wang and et al., "Robust weighted k-means clustering algorithm for a probabilistic-shaped 64qam coherent optical communication system," *Optics Express*, vol. 27, no. 26, pp. 37601–37613, 2019.

[84] X. Lu and et al., "Nonlinear compensation of multi-CAP VLC system employing clustering algorithm based perception decision," *IEEE Photonics Journal*, vol. 9, no. 5, pp. 1–9, 2017.

[85] X. Zhang, W. Liu, N. Huang, and Z. Xu, "Orthogonal waveform-based backscattering interference suppression technique for underwater optical wireless communication," *Journal of the Optical Society of America A*, vol. 41, p. 1372, July 2024.

[86] J. Wang and et al., "Enabling reliable water–air direct optical wireless communication for uncrewed vehicular networks: A deep reinforcement learning approach," *IEEE Transactions on Vehicular Technology*, vol. 73, no. 8, pp. 11470–11486, 2024.

[87] L. Yang, W. Guo, D. B. da Costa, and M.-S. Alouini, "Free-Space Optical Communication With Reconfigurable Intelligent Surfaces," Nov. 2020. arXiv:2012.00547 [cs, math].

[88] V. Matus and et al., "Experimentally derived feasibility of optical camera communications under turbulence and fog conditions," *Sensors*, vol. 20, no. 3, p. 757, 2020.

[89] N. Hautiere, J.-P. Tarel, J. Lavenant, and D. Aubert, "Automatic fog detection and estimation of visibility distance through use of an onboard camera," *Machine vision and applications*, vol. 17, no. 1, pp. 8–20, 2006.

[90] S. Yue, P. Li, and P. Hao, "SVM classification: Its contents and challenges," *Applied Mathematics-A Journal of Chinese Universities*, vol. 18, pp. 332–342, 2003.

[91] G. Guo and et al., "KNN model-based approach in classification," in *On The Move to Meaningful Internet Systems 2003: CoopIS, DOA, and ODBASE: OTM Confederated International Conferences, CoopIS, DOA, and ODBASE 2003, Catania, Sicily, Italy, November 3-7, 2003. Proceedings*, pp. 986–996, Springer, 2003.

[92] J. Che, Z. Liu, and S. Wu, "Gaia: A contention-free optical data center network based on arrayed waveguide grating router," in *2021 Opto-Electronics and Communications Conference (OECC)*, pp. 1–3, IEEE, 2021.

[93] J. Che and et al., "Rgaia: a reconfigurable awgr based optical data center network," *Optics Express*, vol. 30, no. 13, pp. 23640–23655, 2022.

[94] M. Mansoor and et al., "SIMCSO: Improvement of OWC link under snow attenuation," in *2019 2nd International Conference on Communication, Computing and Digital systems (C-CODE)*, pp. 34–39, IEEE, 2019.

[95] S.-K. Liao and et al., "Satellite-to-ground quantum key distribution," *Nature*, vol. 549, no. 7670, pp. 43–47, 2017.

[96] T. Nagatsuma, G. Ducournau, and C. C. Renaud, "Advances in terahertz communications accelerated by photonics," *Nature Photonics*, vol. 10, no. 6, pp. 371–379, 2016.

[97] A. Gomez and et al., "A 50 Gb/s transparent indoor optical wireless communications link with an integrated localization and tracking system," *Journal of Lightwave Technology*, vol. 34, no. 10, pp. 2510–2517, 2016.

[98] J. Tang, R. Jiang, Z. Chen, and Z. Zhu, "Monocular vision aided optical tracking for underwater optical wireless communications," *Optics Express*, vol. 30, p. 14737, Apr. 2022.

[99] R. Feng, Y. Chang, and X. Mao, "Beam tracking algorithm for marine applications using visible light communication," *Applied Optics*, vol. 59, p. 6751, Aug. 2020.

[100] F. Ahmad, R. Sathisha, K. M. Jyothsna, and V. Raghunathan, "Hybrid laser-LED transmitter with closed-loop beam-steering control for indoor optical wireless communication," *Journal of Lightwave Technology*, vol. 40, no. 12, pp. 3557–3566, 2022.

[101] Y. Yang, A. Forbes, and L. Cao, "A review of liquid crystal spatial light modulators: devices and applications," *Opto-Electronic Science*, vol. 2, no. 8, pp. 230026–1, 2023.

[102] Y. Di, Y. Shao, and L.-K. Chen, "Real-time wave mitigation for water-air OWC systems via beam tracking," *IEEE Photonics Technology Letters*, vol. 34, no. 1, pp. 47–50, 2021.

[103] A. Xu, Y. Di, X. Yue, and L.-K. Chen, "Beam tracking aided by complexity-reduced mobilenetv2 for water-air OWC with waves," *IEEE Photonics Technology Letters*, 2024.

[104] A. Xu, Y. Di, X. Yue, and L.-K. Chen, "Seeing through wave—real-time beam tracking via a resnet-based model in water-air OWC systems," in *2024 Optical Fiber Communications Conference and Exhibition (OFC)*, pp. 1–3, IEEE, 2024.

[105] S. Al-Zhrani and et al., "Underwater optical communications: A brief overview and recent developments," *Engineered Science*, vol. 16, pp. 146–186, 2021.

[106] E. B. Muller, V. N. Silva, P. P. Monteiro, and M. C. Medeiros, "Joint optical wireless communication and localization using OFDM," *IEEE Photonics Technology Letters*, vol. 34, no. 14, pp. 757–760, 2022.

[107] I. Takai and et al., "LED and CMOS image sensor based optical wireless communication system for automotive applications," *IEEE photonics journal*, vol. 5, no. 5, pp. 6801418–6801418, 2013.

[108] D. Tse and P. Viswanath, "Fundamentals of Wireless Communication," 2005.

[109] J. Cho and P. J. Winzer, "Probabilistic constellation shaping for optical fiber communications," *Journal of Lightwave Technology*, vol. 37, no. 6, pp. 1590–1607, 2019.

[110] F. Buchali and et al., "Experimental demonstration of capacity increase and rate-adaptation by probabilistically shaped 64-QAM," in *2015 European Conference on Optical Communication (ECOC)*, (Valencia, Spain), pp. 1–3, IEEE, Sept. 2015.

[111] F. Buchali and et al., "Rate adaptation and reach increase by probabilistically shaped 64-QAM: An experimental demonstration," *Journal of Lightwave Technology*, vol. 34, no. 7, pp. 1599–1609, 2016.

[112] M. Kong and et al., "Survey of energy-autonomous solar cell receivers for satellite–air–ground–ocean optical wireless communication," *Progress in quantum electronics*, vol. 74, p. 100300, 2020.

[113] K. O. Odeyemi and P. A. Owolawi, "Performance analysis of reconfigurable intelligent surface in visible light communication systems," *IEEE Access*, vol. 8, pp. 160132–160144, 2020.

[114] Q. Wu and et al., "Intelligent reflecting surface-aided wireless communications: A tutorial," *IEEE Transactions on Communications*, vol. 69, no. 5, pp. 3313–3351, 2021.

[115] M. Najafi, B. Schmauss, and R. Schober, "Intelligent Reflecting Surfaces for Free Space Optical Communication Systems," *IEEE Transactions on Communications*, vol. 69, pp. 6134–6151, Sept. 2021.

[116] L. C. Andrews and R. L. Phillips, *Laser Beam Propagation through Random Media*. Bellingham, WA: SPIE Press, 2nd ed., 2005.

[117] T. Z. Gutema, J. Chen, T. Adiono, and W. O. Popoola, "Comparative study of frequency-based modulations for visible light communication," in *2024 IEEE Wireless Communications and Networking Conference (WCNC)*, pp. 1–6, IEEE, 2024.

[118] N. Lourenco and et al., "Visible light positioning: A roadmap for international standardization," *IEEE Communications Magazine*, vol. 56, no. 3, pp. 68–73, 2018.

[119] M. Zhu, Y. Li, and J. D. Ellis, "Polarization model for total internal reflection-based retroreflectors," *Optical Engineering*, vol. 53, p. 064101, June 2014.

[120] O. Korotkova and N. Farwell, "Effect of oceanic turbulence on polarization of stochastic beams," *Optics communications*, vol. 284, no. 7, pp. 1740–1746, 2011.

[121] F. Chen, Q. Zhao, Y. Chen, and J. Chen, "Polarization properties of quasi-homogeneous beams propagating in oceanic turbulence," *Journal of the Optical Society of Korea*, vol. 17, no. 2, pp. 130–135, 2013.

[122] B. Cochenour, L. Mullen, and J. Muth, "Effect of scattering albedo on attenuation and polarization of light underwater," *Optics letters*, vol. 35, no. 12, pp. 2088–2090, 2010.

[123] J. E. Hansen, "Multiple scattering of polarized light in planetary atmospheres part ii. sunlight reflected by terrestrial water clouds," *Journal of Atmospheric Sciences*, vol. 28, no. 8, pp. 1400–1426, 1971.

[124] C.-Y. Li and et al., "50 Gb/s PAM4 underwater wireless optical communication systems across the water–air–water interface," *Chinese Optics Letters*, vol. 17, no. 10, p. 100004, 2019.

[125] W.-S. Tsai and et al., "A 30 Gb/s PAM4 underwater wireless laser transmission system with optical beam reducer/expander," *Scientific reports*, vol. 9, no. 1, p. 8605, 2019.

[126] W. Liu and et al., "Multilevel polarization shift keying modulation for turbulence-robust underwater optical wireless communication," *Optics Express*, vol. 31, no. 5, pp. 8400–8413, 2023.

[127] C. T. Geldard, J. Thompson, and W. O. Popoola, "Empirical study of the underwater turbulence effect on non-coherent light," *IEEE Photonics Technology Letters*, vol. 32, no. 20, pp. 1307–1310, 2020.

[128] C. A. Williamson and R. C. Hollins, "Measured IOPs of Jerlov water types," *Applied Optics*, vol. 61, no. 33, pp. 9951–9961, 2022.

[129] N. G. Jerlov and F. F. Koczy, *Photographic measurements of daylight in deep water*. Elanders boktr., 1951.

[130] H. M. Oubei, "Underwater wireless optical communications systems: From system-level demonstrations to channel modeling," 2018.

[131] M. V. Jamali and et al., "Statistical distribution of intensity fluctuations for underwater wireless optical channels in the presence of air bubbles," in *2016 Iran Workshop on Communication and Information Theory (IWCIT)*, (Tehran, Iran), pp. 1–6, IEEE, May 2016.

[132] Y. Di, A. Xu, and L.-K. Chen, "Performance enhancement via real-time image-based beam tracking for wa-OWC with dynamic waves and mobile receivers," *Journal of Lightwave Technology*, vol. 42, no. 19, pp. 6671–6678, 2024.

[133] S. A. Self, "Focusing of spherical Gaussian beams," *Applied optics*, vol. 22, no. 5, pp. 658–661, 1983.

[134] A. A. Farid and S. Hranilovic, "Outage capacity optimization for free-space optical links with pointing errors," *Journal of Lightwave technology*, vol. 25, no. 7, pp. 1702–1710, 2007.

[135] R. Smith, "Deflection limits in tall buildings—are they useful?," in *Structures Congress 2011*, pp. 515–527, 2011.

[136] S. A. Al-Gailani and et al., "A survey of free space optics (FSO) communication systems, links, and networks," *IEEE Access*, vol. 9, pp. 7353–7373, 2020.

[137] S. Han, P. Yue, and X. Yi, "Study of an underwater accurate channel model considering comprehensive misalignment errors," *Journal of the Optical Society of America A*, vol. 39, p. 1014, June 2022.

[138] C. Hoyos-Barceló and et al., "Efficient k-NN implementation for real-time detection of cough events in smartphones," *IEEE journal of biomedical and health informatics*, vol. 22, no. 5, pp. 1662–1671, 2017.

[139] S. Tang, X. Zhang, and Y. Dong, "Temporal statistics of irradiance in moving turbulent ocean," in *2013 MTS/IEEE OCEANS-Bergen*, pp. 1–4, IEEE, 2013.

[140] J. Canny, "A computational approach to edge detection," *IEEE Transactions on pattern analysis and machine intelligence*, no. 6, pp. 679–698, 1986.

[141] A. Tou, S. Driz, B. Fassi, and I. S. K. Mahadjoubi, "Harnessing polarization diversity for enhanced reliability in free space optical communications," *Progress In Electromagnetics Research C*, vol. 142, pp. 27–35, 2024.

[142] C.-H. Yeh, Y.-J. Chang, C.-W. Chow, and W.-P. Lin, "Utilizing polarization-multiplexing for free space optical communication transmission with security operation," *Optical Fiber Technology*, vol. 52, p. 101992, 2019.

[143] Z. Li and et al., "Research on light polarization FSO-OFDM system," in *2010 International Conference on Electrical and Control Engineering*, pp. 4552–4555, IEEE, 2010.

[144] H. Chang and et al., "Adaptive optics compensation for orbital angular momentum optical wireless communications," *IEEE Transactions on Wireless Communications*, vol. 21, no. 12, pp. 11151–11163, 2022.

[145] H. Chang and et al., "Low-complexity adaptive optics aided orbital angular momentum based wireless communications," *IEEE Transactions on Vehicular Technology*, vol. 70, no. 8, pp. 7812–7824, 2021.

[146] J. Chen, T. Z. Gutema, and W. O. Popoola, "Adaptive optical wireless communication systems with camera-based underwater turbulence and fog channel estimation," *Applied Optics*, vol. 64, p. 4878, June 2025.